National Technical University of Athens
School of Mechanical Engineering
Fluids Section
Parallel CFD & Optimization Unit

Applications of Topology Optimization in the Design of Microchannel Heat Sinks

Diploma Thesis

Dimitrios Nikolaidis

Supervisor: Kyriakos C. Giannakoglou, Professor NTUA

Athens, 2025

Acknowledgments

First and foremost, I would like to express my deepest gratitude to my supervisor Dr. K.C. Giannakoglou for his guidance and support throughout this endeavor. His expertise and insightful feedback significantly contributed to the quality of this thesis.

I would also like to sincerely thank Dr. E.M. Papoutsis-Kiachagias for his continuous assistance with all the technical difficulties and challenges I encountered. His knowledge, consistent availability and willingness to help played an important role in the successful completion of this work.

Last but not least, I would like to give my heartfelt thanks to my family for their unconditional love and support throughout the entirety of my academic journey. Their encouragement and belief in me, provided the strength and resilience to persevere and complete my studies.

National Technical University of Athens
School of Mechanical engineering
Fluids Section
Parallel CFD & Optimization Unit

Applications of Topology Optimization in the Design of Microchannel Heat Sinks

Diploma Thesis

Dimitrios Nikolaidis

Supervisor: Kyriakos C. Giannakoglou, Professor NTUA

Abstract

This thesis explores the implementation of porosity-based topology optimization in the design of forced convection microchannel heat sinks for electronics cooling applications. A 2.5D conjugate heat transfer model is employed which simplifies the solution of the state/primal problem, by reducing the full 3D governing equations to 2.5D ones. In addition to the momentum conservation equations containing porosity-dependent velocity penalization terms, the thermal conductivity is also formulated as a function of the real-valued porosity field, to model the difference in thermal properties between fluid and solid material. Efficient thermal dissipation from densely packed circuits, heavily contributes to the reliability and longevity of modern electronic systems and hence it is desired to keep temperature levels under control during their operation. Considering this, the maximum temperature appearing in the substrate of the heat sink, which is in direct contact with the electronic components, is chosen as the objective function to be minimized by the topology optimization algorithm. The sensitivity derivatives of the objective function required by the employed gradient-based method used to update the design variables, are computed through the continuous adjoint method.

A heat sink with different fin layouts was considered and the state problem was solved for different pressure drops, using the 2.5D model. The results were compared against full 3D simulations, showing that the low computational cost 2.5D model resolves the heat transfer process quite satisfactorily for low pressure drops across the heat sink. Furthermore, the 2.5D model agrees with the 3D results as to which fin layout is more thermally efficient at a certain operating point (prescribed pressure drop) of the heat sink. Finally, topology optimization was performed using the 2.5D model, for heat sinks

with different inlet-outlet configurations where the substrate was considered uniformly or locally heated. The resulting heat sink geometries, reveal that the algorithm tends to place as many fins as possible in strategic locations in the design space to maximize convective surface area, while keeping the hydraulic resistance at low levels to allow relatively considerable mass flow rates through the heat sink. Hence, a higher number of fins is observed for the heat sinks designed to work at greater pressure drops. The thermal performance of the optimized heat sinks was evaluated and discussed.

Εθνικό Μετσόβιο Πολυτεχνείο
Σχολή Μηχανολόγων Μηχανικών
Τομέας Ρευστών
Μονάδα Παράλληλης Υπολογιστικής Ρευστοδυναμικής & Βελτιστοποίησης

Εφαρμογές Βελτιστοποίησης Τοπολογίας στο Σχεδιασμό Ψυκτρών με Μικροκανάλια

Διπλωματική Εργασία

Δημήτριος Νικολαΐδης

Επιβλέπων: Κυριάκος Χ. Γιαννάκογλου, Καθηγητής ΕΜΠ

Περίληψη

Αντικείμενο αυτής της διπλωματικής εργασίας είναι η χρήση βελτιστοποίησης τοπολογίας, στο σχεδιασμό ψυκτρών (εξαναγκασμένης συναγωγής) με μικροκανάλια, για εφαρμογές ψύξης ηλεκτρονικών κυκλωμάτων. Κάνοντας χρήση ενός 2.5Δ μοντέλου συζυγούς μεταφοράς θερμότητας, οι 3Δ εξισώσεις εκφυλίζονται σε 2.5Δ απλοποιώντας σημαντικά το πρωτεύον πρόβλημα. Οι εξισώσεις διατήρησης ορμής περιέχουν όρους πηγής (όρους ποινής ταχύτητας) που εξαρτώνται από το πεδίο του πορώδους, μηδενίζοντας την ταχύτητα στις στερεοποιημένες περιοχές του υπολογιστικού χωρίου. Επιπλέον η θερμική αγωγιμότητα μοντελοποιείται και αυτή ως συνάρτηση του πορώδους, ώστε να ληφθεί υπόψη η διαφορά στις θερμικές ιδιότητες μεταξύ ρευστού και στερεού. Η αποτελεσματική απαγωγή θερμότητας από ηλεκτρονικά στοιχεία συμβάλλει σημαντικά στην αξιοπιστία και την μακροζωία των μοντέρνων ηλεκτρονικών συστημάτων. Συνεπώς είναι αναγκαίο να διατηρείται η θερμοκρασία σε ελεγχόμενα επίπεδα κατά τη λειτουργία τους. Λαμβάνοντας αυτό υπόψη, η μέγιστη θερμοκρασία που εμφανίζεται στο υπόστρωμα της ψύκτρας, που έρχεται σε άμεση επαφή με τα ηλεκτρικά κυκλώματα, αποτελεί τη συνάρτηση στόχο που αποσκοπεί να ελαχιστοποιήσει ο αλγόριθμος βελτιστοποίησης. Οι παράγωγοι ευαισθησίας που απαιτούνται από την αιτιοκρατική μέθοδο ανανέωσης των μεταβλητών σχεδιασμού, υπολογίζονται μέσω της συνεχούς συζυγούς μεθόδου.

Μελετήθηκε μια ψύκτρα, με διαφορετικές διαμορφώσεις πτερυγίων και το πρωτεύον πρόβλημα επιλύθηκε για διαφορετικές πτώσεις πίεσης, χρησιμοποιώντας το 2.5Δ μοντέλο. Συγκρίνοντας τα αποτελέσματα με αυτά που προέκυψαν από 3Δ προσομοιώσεις, φαίνεται ότι το 2.5Δ μοντέλο επιλύει ικανοποιητικά και, κυρίως, οικονομικά τα φαινόμενα μεταφοράς θερμότητας για μικρές πτώσεις πίεσης κατά μήκος της ψύκτρας. Επιπλέον, το 2.5Δ μοντέλο συμφωνεί με τα 3Δ απο-

τελέσματα ως προς τα ποια διάταξη πτερυγίων είναι η πιο αποδοτική θερμικά, σε συγκεκριμένο σημείο λειτουργίας (δεδομένη κλίση πίεσης) της ψύκτρας. Τέλος, πραγματοποιήθηκε βελτιστοποίηση τοπολογίας χρησιμοποιώντας το 2.5Δ μοντέλο για ψύκτρες με διαφορετικές διατάξεις εισόδου-εξόδου όπου το υπόστρωμα θεωρήθηκε ομοιόμορφα ή τοπικά θερμαινόμενο. Οι γεωμετρίες των ψυκτρών που προέκυψαν, δείχνουν ότι ο αλγόριθμος έχει την τάση να τοποθετεί όσο το δυνατόν περισσότερα πτερύγια σε στρατηγικές θέσεις στο χώρο σχεδιασμού, ώστε να μεγιστοποιήσει την επιφάνεια συναγωγής, χωρίς όμως να αυξήσει την υδραυλική αντίσταση τόσο ώστε να δυσκολέψει τη διέλευση της ροής. Συνεπώς, μεγαλύτερος αριθμός πτερυγίων παρατηρείται στις ψύκτρες που σχεδιάζονται να λειτουργούν σε υψηλότερες πτώσεις πίεσης. Η θερμική απόδοση των βελτιστοποιημένων ψυκτρών αξιολογήθηκε και συζητήθηκε.

Acronyms

NTUA	National Technical University of Athens
PCopt	Parallel CFD & Optimization unit
CFD	Computational Fluid Dynamics
TopO	Topology Optimization
ShpO	Shape Optimization
CHT	Conjugate Heat Transfer
FVM	Finite Volume Method
PDE/s	Partial Differential Equation/s
FD	Finite Differences
DD	Direct Differentiation
1I1O	One Inlet-One Outlet
1I2O	One Inlet-Two Outlet

Contents

Contents **i**

1 Introduction **1**

1.1 Optimization Methods 1

1.2 Topology Optimization: an Overview 2

1.3 Subject of the Thesis 3

1.4 OpenFOAM: an Open Source Software 4

2 Topology Optimization (TopO) **5**

2.1 The State/Primal Problem 5

2.1.1 Primal Field Equations 6

2.1.2 Primal Boundary Conditions 10

2.2 Porosity Field 11

2.2.1 Porosity-Dependent Terms 11

2.2.2 Regularization and Projection of the Porosity Field . . 13

2.3 The Adjoint Problem 14

2.3.1 Augmented Objective Function 15

2.3.2 TopO Objective Function 16

2.3.3 Adjoint Field Equations 17

2.3.4 Adjoint Boundary Conditions 24

2.3.5 Sensitivity Derivatives 25

2.4 The SQP Update Method 27

3 Case Studies **29**

3.1 2.5D vs 3D: Adequacy of the 2.5D Model 29
3.2 Application to TopO Problems 36
3.2.1 The 1I1O and 1I2O CHT TopO Problems 37
3.2.2 The Varying Heat Flux (VHF) Application 43
3.2.3 Porosity Field Initialization: Sensitivity Analysis 46

4 Closure-Conclusions **51**

A 2.5D Problem Formulation **53**
A.1 Velocity and Temperature Profiles 54
A.2 2.5D Equations 60

Bibliography **65**

Chapter 1

Introduction

In early engineering practice, long before modern computers, designers and engineers relied on analytical methods, hand calculations, and trial-and-error experiments to solve optimization problems, often using graphical techniques and simplified models to balance competing design criteria. This manual and painstaking process was primarily based on the intuition and experience of engineers and was limited by the available mathematical tools. The landscape changed dramatically with the advent of digital computers in the mid-20th century, which enabled the development of robust numerical methods and eventually more sophisticated approaches to optimization problems like evolutionary and deterministic algorithms. The increase in computational power, allowed the simulation of complex flows enabling engineers to explore vast design spaces and tackle complex, high-dimensional optimization problems.

1.1 Optimization Methods

The goal of modern optimization techniques is to minimize or maximize objective functions, while satisfying a set of constraints. In computational fluid dynamics (CFD) applications, the objective functions that interest engineers usually indicate the performance of a system or a specific geometry configuration. Such objective functions include total pressure losses, heat dissipation, or lift to drag ratio for aerodynamic design. Optimization methods are divided into two main categories:

Deterministic or Gradient-Based Optimization Methods rely on the calculation of the derivatives of the objective function to search over the

design space, where numerical methods like steepest descent, conjugate gradient, and quasi-Newton algorithms iteratively converge to the optimal solution. Gradient-based approaches offer high precision and strong, efficient convergence for smooth and differentiable objective functions, while they may struggle with noisy or discontinuous functions. Furthermore, their performance can be sensitive to initial guesses or step size parameters, which can cause such methods to become trapped in local minima/maxima especially when dealing with non-convex design spaces [1], [2], [3].

Stochastic Optimization Methods which are based on natural evolution or swarm behavior, incorporate randomness into the search process allowing them to explore the design space more broadly and avoid getting stuck in local optima. Techniques like simulated annealing or genetic algorithms do not require gradient information, making them versatile and applicable to a wide range of complex, high-dimensional problems with noisy objective functions or rugged landscapes, where gradient-based methods may be unreliable. On the downside, stochastic techniques typically require many more function evaluations, leading to slower convergence rates and higher computational costs. The inherent randomness leads to more erratic convergence and sensitivity to parameters like mutation rates, making their performance less predictable compared to deterministic methods [1], [4], [5].

1.2 Topology Optimization: an Overview

The concept of topology optimization (TopO) was first introduced in structural mechanics in [6] in the late 1980s, where a continuous, real-valued density design variable field was used to find the optimal layout of material in structures. The idea was to identify the optimal shape of a geometric structure, that would have the best structural performance under specific loads, by determining the optimal topology of the design space. Areas of the design space with unitary density values corresponded to solid regions, while zero density values indicated the no-material zones. The goal of the algorithm was to find the optimal density distribution, determining which areas should be filled with material and which should remain hollow. Since then, the concept was widely adopted in the field of structural menchanics [7], [8], [9] as well as multidisciplinary optimization problems involving both structural and heat transfer analysis [10], [11].

Over time, this powerful framework has been extended into the realm of CFD, initially proposed for Stokes flows in [12], where the momentum conservation equations were augmented with the Brinkman velocity penalization terms, that were functions of a continuous real-valued porosity field. Areas of the design space with zero (or almost zero) porosity values indicated fluid re-

gions, while areas with very high local porosity values corresponded to solid regions. The target was to identify the optimal porosity distribution that would produce the optimal shape the geometry should have for the required flow patterns to emerge, in order to minimize/maximize certain objective functions.

TopO is a method employed in the early design stages, where no information about the geometry configuration is known a priori. Since the method does not rely on a parameterization scheme to describe the surface of the geometry and modify its boundary every optimization cycle, like in shape optimization (ShpO), it has the freedom to explore almost the entirety of the design space, giving rise to unconventional and non-intuitive solutions. On the other hand, the selection of the parameterization scheme in ShpO restricts the possible solutions that the algorithm can produce, and thus it is used to enhance/fine-tune the shape of the geometry after an initial design has been determined.

Finally, in TopO methods that are based on the porosity (or density) approach, gray areas not belonging to neither region, appear in the design space. These intermediate zones emerge because the optimization relaxes a binary decision (fluid-solid or material-hollow) into a continuous design variable field, which inevitably results in intermediate porosity/density values that do not fully represent a certain region. Hence, the extraction of the interface between two regions is subjective and depends on a certain set tolerance.

1.3 Subject of the Thesis

The main matter of this thesis involves the study and assessment of implementing porosity-based TopO in the design of forced convection microchannel heat sinks, for the cooling of electrical components. Efficient heat dissipation from densely packed circuits is essential for the reliability and longevity of modern electronic systems, preventing thermal overload and minimizing performance degradation.

In addition to the momentum conservation equations containing porosity-dependent velocity penalization terms, the thermal conductivity is also formulated as a function of the real-valued porosity field [13], [14], to accommodate the difference in thermal properties between fluid and solid material. The state problem constitutes a conjugate heat transfer (CHT) problem between solid and fluid regions, with the latter being the design space of the optimization. The goal is to find the optimal material distribution in the fluid region (and hence the optimal flow path) in order to maximize heat dissipation through conduction and convection.

Because of the nature of the geometries that are present when studying microchannel flows, the 2.5D model proposed in [13], for heat sinks with a plate-like geometric structure, is implemented. Following the 2.5D analysis, the 3D governing equations of each region can be reduced to 2.5D ones. In the context of an optimization process, in which the state problem is being solved iteratively, the ability to avoid solving the full 3D problem significantly reduces the computational cost of each run and, subsequently, of each optimization cycle.

The sensitivity derivatives of the objective function required by the Sequential Quadratic Programming (SQP) method [3], which is the employed gradient-based update method for the design variables, are computed with the continuous adjoint method [23], [24], [15], [16]. The main characteristic of the adjoint method, to be able to compute these sensitivities at a cost independent of the number of design variables, plays a key role in reducing the overall computational cost of the optimization method.

1.4 OpenFOAM: an Open Source Software

OpenFOAM is a free, open-source CFD toolbox written in C++ that provides a highly flexible framework for simulating a wide array of physical phenomena: from incompressible and compressible flows to multiphase processes, combustion and heat transfer. It stands out for its extensive collection of solver models, numerous turbulence formulations and a versatile set of boundary conditions that can be easily customized to suit complex applications. At its core, OpenFOAM employs the finite volume method (FVM) to discretize partial differential equations (PDEs), ensuring conservation of fluxes across arbitrary, often unstructured control volumes. These features make it both robust and adaptable for academic research and industrial applications alike. The Parallel CFD and Optimization Unit (PCOpt/NTUA) has developed "adjointOptimisationFoam", an OpenFOAM-based optimization tool that computes the sensitivity derivatives of the objective function, using the continuous adjoint method. The tool can handle a wide range of objective functions and includes both TopO and ShpO problems. The algorithm that solves the 2.5D primal and adjoint problems has also been developed by the PCOpt/NTUA inside the OpenFOAM software; however, this is not publicly available yet. All numerical simulations presented in this thesis were carried out using OpenFOAM.

Chapter 2

Topology Optimization (TopO)

2.1 The State/Primal Problem

In many CFD applications, thin-walled structures are studied, where the thickness or height of the geometry under consideration is extremely small compared to its other dimensions. In such cases, considering that the fluid momentum in the height direction is almost negligible, a reasonable approach would be to completely ignore the minuscule height direction and solve a classic 2D flow problem. However, a viable alternative one can follow to simplify the 3D problem, is to assume that the behavior of the flow is predictable across the height direction. In other words, supposing the flow is fully developed, the velocity and temperature variations across the height direction can be derived under certain simplifications.

Implementing the derived velocity and temperature profiles into the full 3D governing equations and integrating across the height direction gives rise to averaged or 2.5D governing equations [12], [13]. Through this averaging process extra source terms and certain constants in front of already existing terms appear in the resulting equations, that encapsulate part of the information as to how the neglected dimension influences the flow and heat transfer process. The term 2.5D originates from the fact that, although these equations do not provide a fully resolved 3D solution, they give a more accurate representation of the underlying physics than a purely 2D model, where all information about the effect of the third dimension is disregarded.

This type of modeling provides a balanced compromise - it captures certain aspects of the 3D effects, without incurring the high computational cost associated with full 3D simulations. For the study of microchannel flows,

where geometries with small hydraulic diameters and high surface-area-to-volume ratios are present, the use of a 2.5D model is extremely suitable.

2.1.1 Primal Field Equations

The problems analyzed in this thesis involve incompressible and laminar flows, where both the flow and heat transfer process are considered to be steady. Additionally, the fluid and solid properties are assumed to remain constant. The 2.5D CHT model proposed in [13] concerns microchannel heat sinks that have the geometric structure depicted in fig. 2.1, where the height of both the fluid and solid substrate regions is considered relatively small compared to the heat sink's length and width, and thus 2.5D governing equations can be formulated for each region. The heat flux applied to the bottom surface of the substrate is considered uniform.

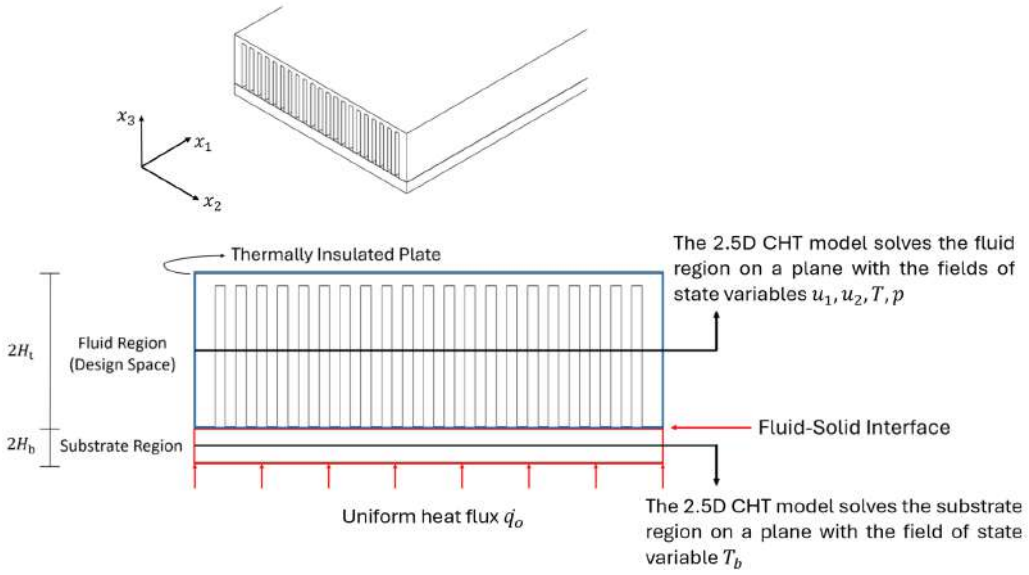

Figure 2.1: *Geometric structure of microchannel heat sinks considered in this thesis, consisting of a bottom substrate solid region and a top adiabatic plate. As the optimization algorithm progresses, parts of the fluid region begin to solidify, i.e. fins appear in the fluid region which is the design space of the optimization. Heat generated by electrical components at the bottom surface of the substrate is conducted through the substrate's material to the fins and fluid. The cooling flow then removes heat from both the substrate and fins via convection, ensuring efficient thermal management.*

The 3D governing continuity, momentum and energy conservation equations for the fluid region are expressed as follows:

$$R^{p} = \frac{\partial u_{j}^{'}}{\partial x_{j}} = 0 \tag{2.1}$$

$$R_{i}^{u^{'}} = \rho u_{j}^{'} \frac{\partial u_{i}^{'}}{\partial x_{j}} + \frac{\partial p}{\partial x_{i}} - \mu \frac{\partial}{\partial x_{j}} \left(\frac{\partial u_{i}^{'}}{\partial x_{j}} + \frac{\partial u_{j}^{'}}{\partial x_{i}} \right) = 0 \quad i = 1, 2, 3 \tag{2.2}$$

$$R^{T^{'}} = \rho C_{p} u_{j}^{'} \frac{\partial T^{'}}{\partial x_{j}} - \frac{\partial}{\partial x_{j}} \left(k_{f} \frac{\partial T^{'}}{\partial x_{j}} \right) = 0 \tag{2.3}$$

where ρ, μ, C_p and k_f are the fluid's density, dynamic viscosity, thermal capacity under constant pressure and thermal conductivity respectively. The 3D pressure field is denoted with $p\left(x_1, x_2, x_3\right)$, while $u_i^{'}\left(x_1, x_2, x_3\right)$ with $i = 1, 2, 3$ are the components of the full 3D velocity field and $T^{'}\left(x_1, x_2, x_3\right)$ the full 3D temperature field of the fluid region. The above equations follow the Einstein convention, where repeated indices imply summation, which will be used from this point forward in the thesis.

The 3D governing heat transfer equation for the solid substrate region can be written as:

$$R^{T_b^{'}} = \frac{\partial}{\partial x_{j}} \left(k_{b} \frac{\partial T_{b}^{'}}{\partial x_{j}} \right) = 0 \tag{2.4}$$

where k_b is the substrate's thermal conductivity and $T_b^{'}\left(x_1, x_2, x_3\right)$ the full 3D temperature field of the substrate region. In this chapter, the 2.5D equations of each region will be directly presented and appropriately modified to fit into a TopO process. Details about the formulation of the 2.5D problem and the derivation of the 2.5D equations from the full 3D ones can be found in Appendix A.

Assuming fully developed flow, the full 3D velocity field can be expressed with the help of the non-dimensional velocity profile $f_u\left(x_3\right)$ which is parabolic and invariant in flow directions x_1, x_2 as shown below:

$$f_{u}\left(x_{3}\right) = 1 - \frac{x_{3}^{2}}{H_{t}^{2}} \tag{2.5}$$

$$\boldsymbol{u}^{'}\left(x_1, x_2, x_3\right) = \begin{bmatrix} u_1^{'}\left(x_1, x_2, x_3\right) \\ u_2^{'}\left(x_1, x_2, x_3\right) \\ u_3^{'}\left(x_1, x_2, x_3\right) \end{bmatrix} = \begin{bmatrix} f_u\left(x_3\right) u_1\left(x_1, x_2\right) \\ f_u\left(x_3\right) u_2\left(x_1, x_2\right) \\ 0 \end{bmatrix} \tag{2.6}$$

where $\boldsymbol{u} = [u_1\ u_2]^T$ is the velocity seen by the 2.5D model and corresponds to the velocity on the mid-plane of the fluid region while H_t is the half height of the design space.

Using the non-dimensional velocity profile $f_u(x_3)$ as a basis the resulting 2.5D continuity and momentum equations can be written as:

$$R^p = \frac{\partial u_j}{\partial x_j} = 0 \tag{2.7}$$

$$R_i^u = \frac{6}{7}\rho u_j \frac{\partial u_i}{\partial x_j} + \frac{5}{4}\frac{\partial p}{\partial x_i} - \mu \frac{\partial}{\partial x_j}\left(\frac{\partial u_i}{\partial x_j} + \frac{\partial u_j}{\partial x_i}\right) - \frac{5}{2}\frac{\mu}{H_t^2}u_i = 0 \quad i = 1, 2 \tag{2.8}$$

where the pressure field p solved by the 2.5D model is now only a function of x_1, x_2.

As previously mentioned, during a TopO process, solid areas begin to form or to be suppressed inside the computational domain. In order for the equations to be able to resolve both the fluid and solid parts of the design space they are augmented with the Brinkman penalization source terms [12], [17], [18] of the form $G(a)\,u_i$, where $a \in [0, 1]$ is the real-valued porosity field. By default, the 2.5D momentum equation 2.8 already includes a similar source term, namely $(-5\mu/2H_t^2)\,u_i$, which represents the averaged stresses $\mu\left(\partial^2 u_i^{'}/\partial x_3^2\right)$ across the height of the fluid region and has emerged as a result of the 2.5D analysis. The 2.5D momentum equation is thus modified as follows:

$$R_i^u = \frac{6}{7}\rho u_j \frac{\partial u_i}{\partial x_j} + \frac{5}{4}\frac{\partial p}{\partial x_i} - \mu \frac{\partial}{\partial x_j}\left(\frac{\partial u_i}{\partial x_j} + \frac{\partial u_j}{\partial x_i}\right) - G(a)\,u_i = 0 \quad i = 1, 2 \tag{2.9}$$

Zero (or almost zero) a values of the porosity field correspond to the fluid part of the design space and thus G must be equal to the value $(5\mu/2H_t^2)$, in order for equation 2.9 to return to its original form, given by equation 2.8, expressing the 2.5D momentum conservation. On the other hand, unitary (or almost unitary) a values indicate the presence of solid material and G should be high enough to drive the solution of the flow equation towards zero in the solidified parts of the design space. The goal of the TopO algorithm is to compute the optimal a distribution, i.e. the optimal fin layout, in order to minimize a given objective function.

Since the flow is also thermally fully developed, the non-dimensional temperature profile $f_T(x_3)$ [13] defined below for the fluid region can also be

considered invariant in directions x_1, x_2:

$$f_T(x_3) = \frac{T_i - T'}{T_i - T} = \frac{35}{416}\left[\left(\frac{x_3}{H_t}\right)^4 - 6\left(\frac{x_3}{H_t}\right)^2 + 8\left(\frac{x_3}{H_t}\right) + 13\right] \tag{2.10}$$

where $T_i(x_1, x_2)$ is the temperature at the interface between fluid and substrate regions and $T(x_1, x_2) = \int_{-H_t}^{+H_t} |\boldsymbol{u}'| T' \, dx_3 / \int_{-H_t}^{+H_t} |\boldsymbol{u}'| \, dx_3$ is the bulk mean temperature of the fluid across x_3.

Based on the non-dimensional temperature profile $f_T(x_3)$, the 2.5D energy equation for the fluid region can be derived [13]:

$$R^T = \frac{4H_t}{3}\rho C_p u_j \frac{\partial T}{\partial x_j} - \frac{49H_t}{26}\frac{\partial}{\partial x_j}\left[k_{eff}\frac{\partial T}{\partial x_j}\right] - \frac{35k_{eff}}{26H_t}(T_i - T) = 0 \tag{2.11}$$

where $k_{eff}(a)$ is the effective thermal conductivity which is used instead of just the fluid's thermal conductivity k_f to account for the presence of fins inside the fluid region. Similar to the velocity penalization terms in the momentum equation 2.9, in order to perform a TopO process, the effective thermal conductivity is also formulated as a function of the real-valued porosity field and should be equal to $k_{eff} = k_f$ in the fluid part of the design space or $k_{eff} = k_b$ in the solid fin areas. Here, the fins are chosen to be made of the same highly conductive solid material as the substrate. This is a design choice rather than a strict requirement.

In a similar manner, the non-dimensional temperature profile $f_{T_b}(x_3)$ [13] defined below for the substrate is invariant in x_1, x_2 directions:

$$f_{T_b}(x_3) = \frac{T_i - T_b'}{T_i - T_b} = 1 - \frac{x_3}{H_b} \tag{2.12}$$

where $T_b(x_1, x_2) = \int_{-H_b}^{+H_b} T_b' \, dx_3 / 2H_b$ stands for the mean temperature of the substrate across x_3 and H_b the half height of the substrate region.

Based on the temperature profile $f_{T_b}(x_3)$, the 2.5D energy equation for the substrate region is obtained [13]:

$$R^{T_b} = 2H_b\frac{\partial}{\partial x_j}\left(k_b\frac{\partial T_b}{\partial x_j}\right) - \frac{k_b}{H_b}(T_b - T_i) + \dot{q_o} = 0 \tag{2.13}$$

where $\dot{q}_o$ is the heat flux applied to the bottom surface of the substrate.

The 2.5D energy equations of the fluid and substrate regions are coupled through the common temperature T_i which can be computed according to the heat flux continuity at the interface boundary:

$$\frac{35k_{eff}\left(a\right)}{26H_t}\left(T_i - T\right) = \frac{k_b}{H_b}\left(T_b - T_i\right) \tag{2.14}$$

The system of the 2.5D energy equations for the entire heat sink can then be written as:

$$R^T = \frac{4H_t}{3}\rho C_p u_j \frac{\partial T}{\partial x_j} - \frac{49H_t}{26}\frac{\partial}{\partial x_j}\left[k_{eff}\left(a\right)\frac{\partial T}{\partial x_j}\right] - h\left(a\right)\left(T_b - T\right) = 0 \tag{2.15}$$

$$R^{T_b} = 2H_b \frac{\partial}{\partial x_j}\left(k_b \frac{\partial T_b}{\partial x_j}\right) - h\left(a\right)\left(T_b - T\right) + \dot{q}_o = 0 \tag{2.16}$$

with $h\left(a\right) = 35k_b k_{eff}\left(a\right) / \left[26H_t k_b + 35H_b k_{eff}\left(a\right)\right]$. Equations 2.7, 2.9, 2.15 and 2.16 comprise the state or primal field equations of the 2.5D problem.

2.1.2 Primal Boundary Conditions

Boundary conditions for the primal variables u_i, p, T and T_b are required for the numerical solution of the primal equations. All cases explored in this thesis are pressure-driven flows, i.e. the static pressure difference between the inlet and outlet boundaries is prescribed and the solver calculates the inlet velocity and inlet mass flow rate. By setting the pressure at the outlet zero, the inlet pressure value p_I is actually the prescribed pressure difference between the two boundaries.

Inlet Boundaries S_I

For the velocity and temperature T_b, a zero Neumann condition is imposed at the inlet boundaries. Dirichlet boundary conditions are set for the pressure and temperature T:

$$\frac{\partial u_i}{\partial x_j} n_j = 0, \quad p = p_I = const, \quad T = T_I = const, \quad \frac{\partial T_b}{\partial x_j} n_j = 0 \tag{2.17}$$

Outlet Boundaries S_O

A zero Dirichlet condition is imposed on pressure while zero Neumann conditions are set for the velocity components and temperatures T, T_b:

$$\frac{\partial u_i}{\partial x_j} n_j = 0, \quad p = 0 = const, \quad \frac{\partial T}{\partial x_j} n_j = 0, \quad \frac{\partial T_b}{\partial x_j} n_j = 0 \tag{2.18}$$

Wall Boundaries $\mathbf{S_W}$

A zero value Dirichlet condition is imposed on the velocity, which expresses the no-slip condition for viscous fluids, and zero Neumann conditions are set for pressure and temperatures T, T_b:

$$u_i = 0, \quad \frac{\partial p}{\partial x_j} n_j = 0, \quad \frac{\partial T}{\partial x_j} n_j = 0, \quad \frac{\partial T_b}{\partial x_j} n_j = 0 \tag{2.19}$$

The 2.5D model solves both the fluid and substrate regions on a single uniform Cartesian 2D mesh, and perceives the fins as areas where cells have a unitary porosity value. In other words, in the context of the 2.5D model, the fin outlines are not strictly considered as solid wall boundaries (see section 3.1). Here, the wall boundaries S_W refer to all other boundaries besides the inlet and outlet that enclose the 2D computational domain Ω upon which the 2.5D model solves the primal equations.

2.2 Porosity Field

The modeling of the porosity-dependent terms appearing in the primal equations influences the solution of not only said equations but also their adjoint counterparts and the computation of the sensitivity derivatives as described in section 2.3. In the following, the filtering and projection of the porosity field, that are employed to prevent noisy geometries and eliminate the gray areas that arise during TopO problems as much as possible, are presented.

2.2.1 Porosity-Dependent Terms

The Brinkman penalization terms $G(a)\, u_i$ and effective thermal conductivity $k_{eff}(a)$ appearing in primal equations 2.9, 2.15 respectively are given by the following expressions [19]:

$$G(a)\, u_i = \left[\frac{5\mu}{2H_t^2} + I(a) \left(\frac{5\mu M^2}{2H_t^2} - \frac{5\mu}{2H_t^2} \right) \right] u_i \tag{2.20}$$

$$k_{eff}(a) = k_f + I(a)(k_b - k_f) \tag{2.21}$$

$I(a)$ is an interpolation function implemented to compute the aforementioned terms for intermediate a values of the porosity field and M is a constant non-dimensional scalar quantity that is used to ensure the Brinkman penalization terms dominate over the other terms appearing in the primal momentum equation, in areas where $a = 1$ (or practically $a \to 1$). Because all other terms become negligible, the only remaining term $G(a)\,u_i$ produces a locally zero velocity field to satisfy equation 2.9 in the solidified parts of the fluid region/design space. Consequently M should be considerably large. As far as the interpolation function $I(a)$ is concerned there is a wide range of choices that can be found in the literature, however the Borrvall-Petersson function [12] shown in equation:

$$I(a) = \frac{a}{1 + b(1 - a)} \tag{2.22}$$

is used in this thesis. The control parameter b adjusts the steepness of the function, with increasing b values more strictly suppressing intermediate values of the porosity field as shown in fig. 2.2. In other words, bigger values of the control parameter b means a clearer distinction between the fluid and solid parts of the design space. It should also be mentioned that the source terms $G(a)\,u_i$ in the primal momentum equation 2.9 are smaller for intermediate a values as the control parameter b increases. This aids the creation of fluid areas in more parts of the design space.

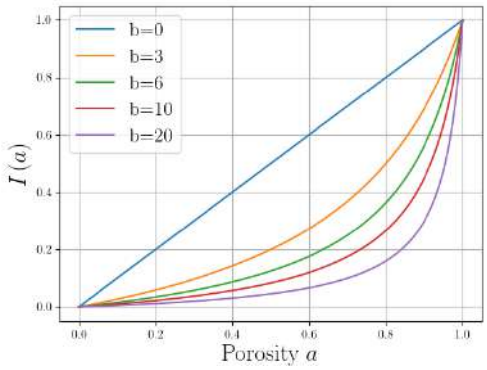

Figure 2.2: *Graphical representation of the Borrvall-Petersson interpolation function $I(a)$ for increasing values of the control parameter b in equation 2.22. Gray areas with intermediate properties between fluid and solid material appear increasingly with lower b values.*

2.2.2 Regularization and Projection of the Porosity Field

In TopO problems, using the porosity field a to directly compute the porosity-dependent terms can lead to rough or checkerboard geometries with the resulting optimal solution depending on the mesh resolution as well as the discretization schemes used to solve the primal and adjoint equations. To avoid such scenarios the density-filtering technique or regularization of the porosity field is employed. Many types of filters have been proposed in the literature, one of them being a Helmholtz-type filter [20] that is based on solving the PDE:

$$-\left(\frac{R}{2\sqrt{3}}\right)^2 \frac{\partial}{\partial x_j}\left(\frac{\partial \tilde{a}}{\partial x_j}\right) + \tilde{a} = a, \qquad R = m_R\left(\bar{V}\right)^{1/2} \tag{2.23}$$

to compute a regularized porosity field $\tilde{a}$ based on the known porosity field a. The regularization radius R is calculated [19] as a multiple of the average cell volume $\bar{V}$. For the numerical solution of equation 2.23, a unitary Dirichlet boundary condition is imposed on $\tilde{a}$ at all wall boundaries belonging in the design space of the computational domain, namely:

$$\tilde{a} = 1 \tag{2.24}$$

Even though the regularization process smoothens the porosity field, it exacerbates the inherent gray area issue in TopO problems, where areas not belonging to neither the fluid nor the solidified part of the design space appear. This effect becomes greater the bigger the regularization radius used in equation 2.23. To remedy this, a projection step of the regularized porosity $\tilde{a}$ field is implemented. Many types of projection methods can be found in the literature, nevertheless the sigmoidal-type [20] projection function shown below is chosen here:

$$\beta = \frac{\tanh\left(0.5\lambda\right) + \tanh\left[\lambda\left(\tilde{a} - 0.5\right)\right]}{2\tanh\left(0.5\lambda\right)} \tag{2.25}$$

The behavior of the projection function for increasing values of the projection parameter λ is depicted in fig. 2.3. Bigger λ values greater highlight the "boundaries" between the solidified and fluid parts of the design space, resulting in a β field that is close to binary.

After the regularization and projection of the porosity field, the computed β field is the one used in equations 2.20, 2.21 and 2.22 to derive the porosity-

dependent terms. From this point forward in the thesis any reference to the primal equations implies that the Brinkman penalization terms, the effective thermal conductivity and of course $h = h\left(k_{eff}\right)$ that appear in them, are calculated based on β and not directly on the porosity field a.

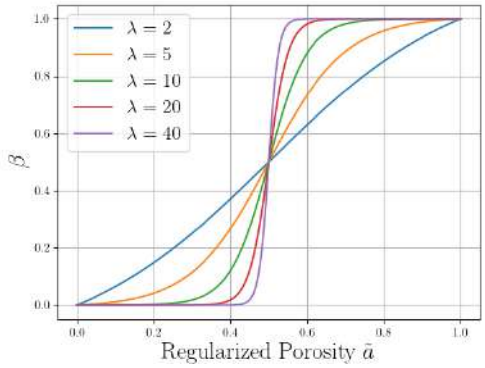

Figure 2.3: *Graphical representation of the projection function with increasing values of the projection parameter λ in equation 2.25.*

2.3 The Adjoint Problem

Deterministic or gradient-based optimization algorithms require the computation of derivatives of the objective function F with respect to (w.r.t.) the design variables in order to proceed to the next optimization cycle. Generally the objective function F depends on the vector of primal or state variables $\boldsymbol{U} = [u_i \; p \; T \; T_b]^T$ and the vector of design variables $\boldsymbol{b}$, whose elements, in TopO problems, are the porosity values a at each grid cell. It is important to note that F may contain the porosity field a in its definition, constituting a direct dependency on the vector of design variables, or/and it can include the primal variables $\boldsymbol{U}$ which in turn depend on the design ones, establishing an indirect dependency on $\boldsymbol{b}$. The latter can be understood, since any change in the design variables vector $\boldsymbol{b}$, i.e. any changes in the porosity field, leads to variations in the primal variables $\boldsymbol{U}$, in order to satisfy the primal equations. From the above it becomes clear that $F = F\left(\boldsymbol{U}\left(\boldsymbol{b}\right), \; \boldsymbol{b}\right)$

One of the greatest factors that influence the computational cost of the optimization algorithm is the method used to compute these gradients or sensitivity derivatives $\delta F/\delta b_n$ with $n \in [1, N]$ and N the number of design variables. One way to derive $\delta F/\delta b_n$ is through the finite differences (FD) method. The basis of the FD method is that an infinitely small variation ϵ is considered in each of the design variables, and the value of the objective function is calculated again for the new set of design variables $\boldsymbol{b}$. For instance, a first

order scheme to compute the derivatives of the objective function F w.r.t the design variables, is expressed below:

$$\frac{\delta F}{\delta b_n} = \frac{F\left(b_1,\ b_2,\ b_3,\ b_n + \epsilon,\ ...,\ b_N\right) - F\left(b_1,\ b_2,\ b_3,\ b_n,\ ...,\ b_N\right)}{\epsilon} \quad n \in [1, N]$$

The primal problem must be solved each time the value of F needs to be re-evaluated, which for this example would be $(N + 1)$ times, and so even though the FD method is mathematically simple, the computational cost is proportional to the number of design variables N and to the order of the scheme used. Another method to compute $\delta F/\delta b_n$ is direct differentiation (DD), where the primal equations are differentiated w.r.t $\boldsymbol{b}$ and N systems of equations, similar to the primal equations, are solved to derive the derivatives of the primal variables $\boldsymbol{U}$ w.r.t the design ones. Through $\delta \boldsymbol{U}/\delta b_n$ the much needed sensitivity derivatives $\delta F/\delta b_n$ are computed. Consequently, the computational cost of the DD method also scales with the number of design variables N.

According to the adjoint method, by solving a dual problem, the primal and its similar in nature adjoint counterpart, the sensitivity derivatives can be derived in such a way, that the computation cost becomes independent of N. For TopO problems where the number of design variables is the same as the number of mesh cells, meaning the optimization has tens of thousands of design variables, the adjoint method is a perfect candidate. Two variations of the adjoint method can be found in the bibliography. **The discrete adjoint method** [21], [22], where the primal equations are first discretized and then used in the definition of the augmented objective function to be differentiated. As a result the system of the adjoint equations is extracted directly in its discrete form. Secondly, **the continuous adjoint method** [23], [24], which will be employed in this thesis, where the primal equations are used in their continuous form in the definition of the augmented objective function to be differentiated. The resulting adjoint equations are PDEs that need to be discretized in order to be numerically solved.

2.3.1 Augmented Objective Function

Following the mathematical formulation found in [15], [16], the augmented objective function is defined by adding the volume integrals of the residuals of the primal equations, multiplied by the adjoint variables, to F:

$$F_{aug} = F + \int_{\Omega} v_i R_i^u \, d\Omega + \int_{\Omega} q R^p \, d\Omega + \int_{\Omega} T_a R^T \, d\Omega + \int_{\Omega} T_{ab} R^{T_b} \, d\Omega \quad (2.26)$$

where v_i, q, T_a, T_{ab} is the adjoint velocity, the adjoint pressure, the adjoint temperatures for the fluid and substrate regions respectively and Ω the 2D computational domain, upon which the 2.5D model solves the primal equations. Taking into consideration that, in TopO problems, all boundaries of Ω are fixed and independent of the design variables, the differentiation of F_{aug} w.r.t. the porosity field yields:

$$\frac{\delta F_{aug}}{\delta a} = \frac{\delta F}{\delta a} + \int_{\Omega} v_i \frac{\partial R_i^u}{\partial a} \, d\Omega + \int_{\Omega} q \frac{\partial R^p}{\partial a} \, d\Omega + \int_{\Omega} T_a \frac{\partial R^T}{\partial a} \, d\Omega \quad (2.27)$$

$$+ \int_{\Omega} T_{ab} \frac{\partial R^{T_b}}{\partial a} \, d\Omega$$

Since the residuals of the primal equations must always be equal to zero it is evident that $F_{aug} = F$ and $\delta F_{aug}/\delta a = \delta F/\delta a$.

2.3.2 TopO Objective Function

The goal of the TopO process is to identify the optimal heat sink geometry, i.e. the optimal fin layout in the fluid region, that has the best thermal performance. Consequently, the (normalized) maximum temperature appearing in the substrate region, which is in direct contact with the electronic components, is chosen as the objective function to be minimized by the TopO. This is given by equation:

$$F = \left[\int_{\Omega} \left(\frac{T_b}{T_{ref}} \right)^p \, d\Omega \right]^{\frac{1}{p}} \quad (2.28)$$

where $p \geq 1$ the norm parameter and T_{ref} a constant normalization reference temperature (usually the fluid inlet temperature T_I is selected). As $p \to \infty$ the aggregation function 2.28 approaches the (normalized) maximum temperature of the substrate [25]. Differentiating F w.r.t the porosity variables, yields:

$$\frac{\delta F}{\delta a} = \underbrace{\frac{1}{pT_{ref}^{p}} \left[\int_{\Omega} \left(\frac{T_b}{T_{ref}} \right)^{p} \, d\Omega \right]^{\frac{1-p}{p}}}_{F_g} \int_{\Omega} pT_b^{p-1} \frac{\partial T_b}{\partial a} \, d\Omega \tag{2.29}$$

By substituting equation 2.29 to 2.27, the final expression of the derivative of F_{aug} w.r.t the design variables is obtained:

$$\frac{\delta F_{aug}}{\delta a} = \int_{\Omega} F_g pT_b^{p-1} \frac{\partial T_b}{\partial a} \, d\Omega + \underbrace{\int_{\Omega} v_i \frac{\partial R_i^u}{\partial a} \, d\Omega}_{T_1} + \underbrace{\int_{\Omega} q \frac{\partial R^p}{\partial a} \, d\Omega}_{T_2} \tag{2.30}$$

$$+ \underbrace{\int_{\Omega} T_a \frac{\partial R^T}{\partial a} \, d\Omega}_{T_3} + \underbrace{\int_{\Omega} T_{ab} \frac{\partial R^{T_b}}{\partial a} \, d\Omega}_{T_4}$$

2.3.3 Adjoint Field Equations

For the computation of the derivatives of the primal equation residuals w.r.t the design variables, appearing in volume integrals T_1, T_2, T_3 and T_4 in equation 2.30, the relation:

$$\frac{\partial}{\partial a} \left(\frac{\partial \Phi}{\partial x_i} \right) = \frac{\partial}{\partial x_i} \left(\frac{\partial \Phi}{\partial a} \right) \tag{2.31}$$

is used. This equation holds true because the partial derivative $\partial/\partial a$ of a quantity Φ shows the change in Φ w.r.t the design variables, by including only the contribution from the variations in the primal variables $\boldsymbol{U}$ and not any changes in the shape of the computational domain's boundaries.

Computation of volume integral T_1

Differentiating the momentum equation 2.9 w.r.t. the porosity variables results in:

$$\frac{\partial R_i^u}{\partial a} = \frac{6}{7}\rho\left[\frac{\partial u_j}{\partial a}\frac{\partial u_i}{\partial x_j} + u_j\frac{\partial}{\partial x_j}\left(\frac{\partial u_i}{\partial a}\right)\right] - \mu\frac{\partial}{\partial x_j}\left[\frac{\partial}{\partial a}\left(\frac{\partial u_i}{\partial x_j} + \frac{\partial u_j}{\partial x_i}\right)\right]$$

$$+\frac{5}{4}\frac{\partial}{\partial x_i}\left(\frac{\partial p}{\partial a}\right) - \frac{\partial}{\partial a}\left(G u_i\right) = 0 \tag{2.32}$$

The viscous terms in the volume integral T_1 are:

$$-\int_\Omega \mu v_i \frac{\partial}{\partial x_j}\left[\frac{\partial}{\partial a}\left(\frac{\partial u_i}{\partial x_j} + \frac{\partial u_j}{\partial x_i}\right)\right]\, d\Omega = -\int_S \mu v_i n_j \frac{\partial}{\partial a}\left(\frac{\partial u_i}{\partial x_j} + \frac{\partial u_j}{\partial x_i}\right)\, dS$$

$$+\int_\Omega \mu \frac{\partial v_i}{\partial x_j}\frac{\partial}{\partial a}\left(\frac{\partial u_i}{\partial x_j} + \frac{\partial u_j}{\partial x_i}\right)\, d\Omega$$

$$= -\int_S \mu v_i n_j \frac{\partial}{\partial a}\left(\frac{\partial u_i}{\partial x_j} + \frac{\partial u_j}{\partial x_i}\right)\, dS + \int_\Omega \mu \frac{\partial v_i}{\partial x_j}\frac{\partial}{\partial x_j}\left(\frac{\partial u_i}{\partial a}\right)\, d\Omega$$

$$+\int_\Omega \mu \frac{\partial v_i}{\partial x_j}\frac{\partial}{\partial x_i}\left(\frac{\partial u_j}{\partial a}\right)\, d\Omega$$

$$= -\int_S \mu v_i n_j \frac{\partial}{\partial a}\left(\frac{\partial u_i}{\partial x_j} + \frac{\partial u_j}{\partial x_i}\right)\, dS + \int_S \mu \frac{\partial v_i}{\partial x_j} n_j \frac{\partial u_i}{\partial a}\, dS \tag{2.33}$$

$$-\int_\Omega \mu \frac{\partial}{\partial x_j}\left(\frac{\partial v_i}{\partial x_j}\right)\frac{\partial u_i}{\partial a}\, d\Omega + \int_S \mu \frac{\partial v_i}{\partial x_j} n_i \frac{\partial u_j}{\partial a}\, dS$$

$$-\int_\Omega \mu \frac{\partial}{\partial x_i}\left(\frac{\partial v_i}{\partial x_j}\right)\frac{\partial u_j}{\partial a}\, d\Omega$$

The convection terms are written as:

$$\int_\Omega \frac{6}{7}\rho v_i \frac{\partial u_i}{\partial x_j}\frac{\partial u_j}{\partial a}\, d\Omega + \int_\Omega \frac{6}{7}\rho v_i u_j \frac{\partial}{\partial x_j}\left(\frac{\partial u_i}{\partial a}\right)\, d\Omega$$

$$= \int_\Omega \frac{6}{7}\rho v_i \frac{\partial u_i}{\partial x_j}\frac{\partial u_j}{\partial a}\, d\Omega + \int_S \frac{6}{7}\rho v_i u_j n_j \frac{\partial u_i}{\partial a}\, dS - \int_\Omega \frac{6}{7}\rho \frac{\partial}{\partial x_j}\left(v_i u_j\right)\frac{\partial u_i}{\partial a}\, d\Omega \quad (2.34)$$

Following with the pressure terms in T_1:

$$\int_\Omega \frac{5}{4} v_i \frac{\partial}{\partial x_i}\left(\frac{\partial p}{\partial a}\right)\, d\Omega = \int_S \frac{5}{4} v_i n_i \frac{\partial p}{\partial a}\, dS - \int_\Omega \frac{5}{4}\frac{\partial v_i}{\partial x_i}\frac{\partial p}{\partial a}\, d\Omega \quad (2.35)$$

Finally, the porosity-dependent terms in T_1 are:

$$-\int_\Omega v_i \frac{\partial}{\partial a}\left(G u_i\right)\, d\Omega = -\int_\Omega v_i u_i \frac{\partial G}{\partial a}\, d\Omega - \int_\Omega v_i G \frac{\partial u_i}{\partial a}\, d\Omega \quad (2.36)$$

Computation of volume integral T_2

Differentiating the continuity equation 2.7 w.r.t the design variables gives:

$$\frac{\partial R^p}{\partial a} = \frac{\partial}{\partial x_j}\left(\frac{\partial u_j}{\partial a}\right) = 0 \quad (2.37)$$

so that:

$$\int_\Omega q \frac{\partial}{\partial x_j}\left(\frac{\partial u_j}{\partial a}\right)\, d\Omega = \int_S q \frac{\partial u_j}{\partial a} n_j\, dS - \int_\Omega \frac{\partial q}{\partial x_j}\frac{\partial u_j}{\partial a}\, d\Omega \quad (2.38)$$

Computation of volume integral T_3

The derivative of the fluid region's energy equation 2.15 w.r.t. the porosity is:

$$\frac{\partial R^T}{\partial a} = \frac{4H_t}{3}\rho C_p\left[\frac{\partial u_j}{\partial a}\frac{\partial T}{\partial x_j} + u_j \frac{\partial}{\partial x_j}\left(\frac{\partial T}{\partial a}\right)\right] - \frac{49 H_t}{26}\frac{\partial}{\partial x_j}\left[\frac{\partial}{\partial a}\left(k_{eff}\frac{\partial T}{\partial x_j}\right)\right]$$

$$-h\left(\frac{\partial T_b}{\partial a} - \frac{\partial T}{\partial a}\right) - \frac{\partial h}{\partial a}\left(T_b - T\right) = 0 \quad (2.39)$$

The diffusion (or conduction) terms in the volume integral T_3 are:

$$
\begin{aligned}
&- \int_\Omega \frac{49H_t}{26} T_a \frac{\partial}{\partial x_j} \left[\frac{\partial}{\partial a} \left(k_{eff} \frac{\partial T}{\partial x_j} \right) \right] \, d\Omega = - \int_S \frac{49H_t}{26} T_a \frac{\partial}{\partial a} \left(k_{eff} \frac{\partial T}{\partial x_j} \right) n_j \, dS \\
&+ \int_\Omega \frac{49H_t}{26} \frac{\partial T_a}{\partial x_j} \frac{\partial}{\partial a} \left(k_{eff} \frac{\partial T}{\partial x_j} \right) \, d\Omega \\
= &+ \frac{49H_t}{26} \left[- \int_S T_a \frac{\partial}{\partial a} \left(k_{eff} \frac{\partial T}{\partial x_j} \right) n_j \, dS + \int_\Omega \frac{\partial T_a}{\partial x_j} \frac{\partial k_{eff}}{\partial a} \frac{\partial T}{\partial x_j} \, d\Omega \right. \\
&\left. + \int_\Omega \frac{\partial T_a}{\partial x_j} k_{eff} \frac{\partial}{\partial x_j} \left(\frac{\partial T}{\partial a} \right) \, d\Omega \right] \\
= &+ \frac{49H_t}{26} \left[- \int_S T_a \frac{\partial}{\partial a} \left(k_{eff} \frac{\partial T}{\partial x_j} \right) n_j \, dS + \int_\Omega \frac{\partial T_a}{\partial x_j} \frac{\partial k_{eff}}{\partial a} \frac{\partial T}{\partial x_j} \, d\Omega \right. \\
&\left. + \int_S \frac{\partial T_a}{\partial x_j} k_{eff} \frac{\partial T}{\partial a} n_j \, dS - \int_\Omega \frac{\partial}{\partial x_j} \left(k_{eff} \frac{\partial T_a}{\partial x_j} \right) \frac{\partial T}{\partial a} \, d\Omega \right] \qquad (2.40)
\end{aligned}
$$

The convection terms are analyzed as follows:

$$
\int_\Omega \frac{4H_t}{3} \rho C_p T_a \frac{\partial u_j}{\partial a} \frac{\partial T}{\partial x_j} \, d\Omega + \int_\Omega \frac{4H_t}{3} \rho C_p T_a u_j \frac{\partial}{\partial x_j} \left(\frac{\partial T}{\partial a} \right) \, d\Omega \qquad (2.41)
$$

$$
= \frac{4H_t}{3} \rho C_p \left[\int_\Omega T_a \frac{\partial u_j}{\partial a} \frac{\partial T}{\partial x_j} \, d\Omega + \int_S T_a u_j n_j \frac{\partial T}{\partial a} \, dS - \int_\Omega \frac{\partial}{\partial x_j} \left(u_j T_a \right) \frac{\partial T}{\partial a} \, d\Omega \right]
$$

The source terms in T_3 are written as:

$$
\begin{aligned}
&- \int_\Omega T_a h \left(\frac{\partial T_b}{\partial a} - \frac{\partial T}{\partial a} \right) \, d\Omega - \int_\Omega \frac{\partial h}{\partial a} T_a \left(T_b - T \right) \, d\Omega = - \int_\Omega T_a h \frac{\partial T_b}{\partial a} \, d\Omega \\
&+ \int_\Omega T_a h \frac{\partial T}{\partial a} \, d\Omega - \int_\Omega \frac{\partial h}{\partial a} T_a \left(T_b - T \right) \, d\Omega \qquad (2.42)
\end{aligned}
$$

Computation of volume integral T_4

Differentiating the energy equation 2.16 for the substrate w.r.t the design variables yields:

$$\frac{\partial R^{T_b}}{\partial a} = 2H_b \frac{\partial}{\partial x_j}\left[k_b \frac{\partial}{\partial a}\left(\frac{\partial T_b}{\partial x_j}\right)\right] - h\left(\frac{\partial T_b}{\partial a} - \frac{\partial T}{\partial a}\right) - \frac{\partial h}{\partial a}\left(T_b - T\right) = 0 \quad (2.43)$$

The conduction terms in the volume integral T_4 are:

$$\begin{aligned}
&\int_\Omega 2H_b T_{ab} \frac{\partial}{\partial x_j}\left[k_b \frac{\partial}{\partial a}\left(\frac{\partial T_b}{\partial x_j}\right)\right]\, d\Omega = \int_S 2H_b T_{ab} k_b \frac{\partial}{\partial a}\left(\frac{\partial T_b}{\partial x_j}\right) n_j\, dS \\
&- \int_\Omega 2H_b \frac{\partial T_{ab}}{\partial x_j} k_b \frac{\partial}{\partial x_j}\left(\frac{\partial T_b}{\partial a}\right)\, d\Omega \\
&= \int_S 2H_b T_{ab} k_b \frac{\partial}{\partial a}\left(\frac{\partial T_b}{\partial x_j}\right) n_j\, dS - \int_S 2H_b \frac{\partial T_{ab}}{\partial x_j} k_b \frac{\partial T_b}{\partial a} n_j\, dS \qquad (2.44) \\
&+ \int_\Omega 2H_b \frac{\partial}{\partial x_j}\left(k_b \frac{\partial T_{ab}}{\partial x_j}\right) \frac{\partial T_b}{\partial a}\, d\Omega
\end{aligned}$$

The source terms in T_4 are:

$$\begin{aligned}
&- \int_\Omega T_{ab} h \left(\frac{\partial T_b}{\partial a} - \frac{\partial T}{\partial a}\right)\, d\Omega - \int_\Omega T_{ab} \frac{\partial h}{\partial a}\left(T_b - T\right)\, d\Omega = - \int_\Omega T_{ab} h \frac{\partial T_b}{\partial a}\, d\Omega \\
&+ \int_\Omega T_{ab} h \frac{\partial T}{\partial a}\, d\Omega - \int_\Omega T_{ab} \frac{\partial h}{\partial a}\left(T_b - T\right)\, d\Omega \qquad (2.45)
\end{aligned}$$

By taking equations 2.33, 2.34, 2.35, 2.36, 2.38, 2.40, 2.41, 2.42, 2.44, 2.45 into consideration and grouping terms together (the indices i,j may need to be exchanged for some terms) the expression 2.30 for $\delta F_{aug}/\delta a$ becomes:

$$\frac{\delta F_{aug}}{\delta a} = \int_S \frac{\partial u_i}{\partial a}\left[\frac{6}{7}\rho v_i u_j n_j + \mu\left(\frac{\partial v_i}{\partial x_j} + \frac{\partial v_j}{\partial x_i}\right) n_j + q n_i\right]\, dS \qquad (2.46)$$

$$+ \int_S \frac{\partial p}{\partial a}\left(\frac{5}{4} v_i n_i\right)\, dS - \int_S \frac{\partial \tau_{ij}}{\partial a} v_i n_j\, dS$$

$$+ \int_S \frac{\partial T}{\partial a}\left(\frac{4H_t}{3}\rho C_p T_a u_j n_j + \frac{49 H_t}{26} k_{eff}\frac{\partial T_a}{\partial x_j} n_j\right)\, dS$$

$$+ \int_S \frac{\partial T_b}{\partial a}\left(-2H_b k_b \frac{\partial T_{ab}}{\partial x_j} n_j\right)\, dS + \int_S 2H_b k_b T_{ab}\frac{\partial}{\partial a}\left(\frac{\partial T_b}{\partial x_j}\right) n_j\, dS$$

$$- \int_S \frac{49 H_t}{26} T_a \frac{\partial}{\partial a}\left(k_{eff}\frac{\partial T}{\partial x_j}\right) n_j\, dS + \int_\Omega \frac{\partial u_i}{\partial a}\left\{\frac{6}{7}\rho\left[v_j \frac{\partial u_j}{\partial x_i}\right.\right.$$

$$\left. - \frac{\partial}{\partial x_j}\left(v_i u_j\right)\right] - \mu \frac{\partial}{\partial x_j}\left(\frac{\partial v_i}{\partial x_j} + \frac{\partial v_j}{\partial x_i}\right) - \frac{\partial q}{\partial x_i} + \frac{4H_t}{3}\rho C_p T_a \frac{\partial T}{\partial x_i}$$

$$\left. - G v_i\right\}\, d\Omega + \int_\Omega \frac{\partial p}{\partial a}\left(-\frac{5}{4}\frac{\partial v_i}{\partial x_i}\right)\, d\Omega + \int_\Omega \frac{\partial T}{\partial a}\left[-\frac{4H_t}{3}\rho C_p\right.$$

$$\left. \frac{\partial}{\partial x_j}\left(u_j T_a\right) - \frac{49 H_t}{26}\frac{\partial}{\partial x_j}\left(k_{eff}\frac{\partial T_a}{\partial x_j}\right) + h\left(T_a + T_{ab}\right)\right] d\Omega$$

$$+ \int_\Omega \frac{\partial T_b}{\partial a}\left[F_g p T_b^{p-1} + 2H_b \frac{\partial}{\partial x_j}\left(k_b \frac{\partial T_{ab}}{\partial x_j}\right) - h\left(T_a + T_{ab}\right)\right]\, d\Omega$$

$$- \int_\Omega v_i u_i \frac{\partial G}{\partial a}\, d\Omega + \int_\Omega \frac{49 H_t}{26}\frac{\partial T_a}{\partial x_j}\frac{\partial T}{\partial x_j}\frac{\partial k_{eff}}{\partial a}\, d\Omega$$

$$- \int_\Omega \frac{\partial h}{\partial a}\left(T_b - T\right)\left(T_a + T_{ab}\right)\, d\Omega$$

By zeroing the multipliers of $\partial u_i/\partial a$, $\partial p/\partial a$, $\partial T/\partial a$ and $\partial T_b/\partial a$ in the volume integrals of expression 2.46, the adjoint field equations are derived:

$$R^q = -\frac{5}{4}\frac{\partial v_i}{\partial x_i} = 0 \tag{2.47}$$

$$R_i^v = \frac{6}{7}\rho\left[v_j\frac{\partial u_j}{\partial x_i} - \frac{\partial}{\partial x_j}\left(v_i u_j\right)\right] - \mu\frac{\partial}{\partial x_j}\left(\frac{\partial v_i}{\partial x_j} + \frac{\partial v_j}{\partial x_i}\right) + \frac{4H_t}{3}\rho C_p T_a\frac{\partial T}{\partial x_i}$$

$$-\frac{\partial q}{\partial x_i} - G v_i = 0 \tag{2.48}$$

$$R^{T_a} = -\frac{4H_t}{3}\rho C_p\frac{\partial}{\partial x_j}\left(u_j T_a\right) - \frac{49H_t}{26}\frac{\partial}{\partial x_j}\left(k_{eff}\frac{\partial T_a}{\partial x_j}\right) + h\left(T_a + T_{ab}\right) = 0 \tag{2.49}$$

$$R^{T_{ab}} = F_g p T_b^{p-1} + 2H_b\frac{\partial}{\partial x_j}\left(k_b\frac{\partial T_{ab}}{\partial x_j}\right) - h\left(T_a + T_{ab}\right) = 0 \tag{2.50}$$

Equations 2.47, 2.48, 2.49 and 2.50 comprise the adjoint continuity, momentum and adjoint energy equations for the fluid and substrate regions respectively. The adjoint equations are similar in nature to the primal ones, with the adjoint momentum equation 2.48 and adjoint energy equations 2.49, 2.50 both containing porosity-dependent terms just like their primal counterparts. Consequently, the way $G\left(\beta\right)$ and $k_{eff}\left(\beta\right)$ are formulated influences the solution of both the primal and adjoint field equations. The appearance of the term $G\left(\beta\right)v_i$ in the adjoint momentum equation signifies that in the solidified areas of the design space where porosity values $a \to 1$ and hence $\beta \to 1$, a zero adjoint velocity field is produced.

In an incompressible fluid flow, the solution of the primal momentum equation is independent of the primal temperature field T. However, T is influenced by the primal velocity field u_i, as evident from equations 2.9 and 2.15. Notably, the exact opposite holds true for the adjoint field equations, meaning the adjoint temperature field T_a does not depend on the adjoint velocity field v_i (T_a is convected by the primal velocity), whereas v_i is affected by T_a.

2.3.4 Adjoint Boundary Conditions

To numerically solve the adjoint equations, boundary conditions for the adjoint variables v_i, q, T_a and T_{ab} are required. For each boundary of the computational domain Ω, and depending on the specific primal boundary conditions set for that boundary, the adjoint boundary conditions are derived such as all surface integrals of equation 2.46 are always equal to zero.

Inlet boundaries $\mathbf{S_I}$

For the inlet boundaries of Ω, Dirichlet boundary conditions are imposed on p, T and zero Neumann conditions are set for the velocity components u_i and temperature T_b. This means that $\partial p/\partial a$ and $\partial T/\partial a$ are equal to zero and thus the second and fourth surface integrals in equation 2.46 are eliminated. Considering equation:

$$\frac{\partial}{\partial a}\left(\frac{\partial \Phi}{\partial x_j}\right) n_j = \frac{\partial}{\partial a}\left(\frac{\partial \Phi}{\partial x_j} n_j\right) \tag{2.51}$$

which holds true because all boundaries of Ω are fixed and independent of the design variables, the sixth boundary integral in equation 2.46, also vanishes. Zeroing the contents of the first and third surface integrals in equation 2.46 leads to the boundary conditions for the adjoint velocity and pressure:

$$\frac{6}{7}\rho v_i u_j n_j + \mu\left(\frac{\partial v_i}{\partial x_j} + \frac{\partial v_j}{\partial x_i}\right) n_j + q n_i = 0 \tag{2.52}$$

$$-v_i n_j = 0 \tag{2.53}$$

The boundary conditions for T_a and T_{ab} that arise in order for the fifth and seventh boundary integrals in equation 2.46 to vanish are pretty straightforward:

$$T_a = 0, \quad \frac{\partial T_{ab}}{\partial x_j} n_j = 0 \tag{2.54}$$

Outlet boundaries $\mathbf{S_O}$

Zero Neumann conditions are imposed on the velocity and temperatures T and T_b and a Dirichlet condition is set for pressure along S_O. As a result $\partial p/\partial a$ and hence the second surface integral in equation 2.46 are equal to zero. The equations that lead to the derivation of the adjoint boundary conditions for v_i and q are equations 2.52 and 2.53, the same as for the inlet

boundaries. Considering the zero Neumann conditions set for T and T_b and equation 2.51 the sixth and seventh surface integrals in expression 2.46 vanish. The fourth and fifth boundary integrals lead to the following equations that define the adjoint boundary conditions for T_a and T_{ab}:

$$\frac{4H_t}{3}\rho C_p T_a u_j n_j + \frac{49H_t}{26}k_{eff}\frac{\partial T_a}{\partial x_j}n_j = 0 \tag{2.55}$$

$$\frac{\partial T_{ab}}{\partial x_j}n_j = 0 \tag{2.56}$$

Wall boundaries S_W

For the wall boundaries of Ω a zero Dirichlet condition is set for the velocity components and zero Neumann conditions are employed for p, T and T_b. Since $\partial u_i/\partial a$ is zero the first surface integral of equation 2.46 vanishes on its own. The second and third boundary integrals in the same equation give rise to equations:

$$\frac{5}{4}v_i n_i = 0 \tag{2.57}$$

$$-v_i n_j = 0 \tag{2.58}$$

that define the adjoint boundary conditions for the adjoint velocity. The adjoint boundary conditions imposed on the adjoint temperatures T_a and T_{ab} are identical with the ones for the outlet boundaries of Ω and are given by equations 2.55 and 2.56. Because no boundary condition was derived for q with no more surface integrals remaining in equation 2.46 a zero Neumann condition is imposed on q:

$$\frac{\partial q}{\partial x_j}n_j = 0 \tag{2.59}$$

2.3.5 Sensitivity Derivatives

With the adjoint equations and their corresponding boundary conditions derived, expression 2.46, that gives the sensitivity derivatives of the augmented objective function F_{aug} w.r.t the design variables, is simplified to:

$$\frac{\delta F_{aug}}{\delta a} = -\int_{\Omega} v_i u_i \frac{\partial G(\beta)}{\partial a}\, d\Omega + \int_{\Omega} \frac{49 H_t}{26} \frac{\partial T_a}{\partial x_j} \frac{\partial T}{\partial x_j} \frac{\partial k_{eff}(\beta)}{\partial a}\, d\Omega \tag{2.60}$$

$$-\int_{\Omega} \frac{\partial h(\beta)}{\partial a} (T_b - T)(T_a + T_{ab})\; d\Omega$$

Using the chain rule, the differentiation of the porosity-dependent terms $G(\beta)$ and $k_{eff}(\beta)$ w.r.t the porosity field is shown below:

$$\frac{\partial G(\beta)}{\partial a} = \frac{\partial G(\beta)}{\partial \beta}\, \frac{\partial \beta}{\partial \tilde{a}}\, \frac{\partial \tilde{a}}{\partial a} \tag{2.61}$$

$$\frac{\partial k_{eff}(\beta)}{\partial a} = \frac{\partial k_{eff}(\beta)}{\partial \beta}\, \frac{\partial \beta}{\partial \tilde{a}}\, \frac{\partial \tilde{a}}{\partial a} \tag{2.62}$$

Taking the formulations 2.20, 2.21 into consideration, equations 2.61 and 2.62 become:

$$\frac{\partial G(\beta)}{\partial a} = \left(\frac{5\mu M^2}{2H_t^2} - \frac{5\mu}{2H_t^2}\right) \frac{\partial I(\beta)}{\partial \beta}\, \frac{\partial \beta}{\partial \tilde{a}}\, \frac{\partial \tilde{a}}{\partial a} \tag{2.63}$$

$$\frac{\partial k_{eff}(\beta)}{\partial a} = (k_b - k_f) \frac{\partial I(\beta)}{\partial \beta}\, \frac{\partial \beta}{\partial \tilde{a}}\, \frac{\partial \tilde{a}}{\partial a} \tag{2.64}$$

Since h is a function of the porosity-dependent effective thermal conductivity $k_{eff}(\beta)$, its derivative w.r.t. the porosity field is easily obtained:

$$\frac{\partial h(\beta)}{\partial a} = \frac{35 k_b \frac{\partial k_{eff}}{\partial a} \left[26 H_t k_b + 35 H_b k_{eff}\right] - 1225 H_b k_b k_{eff} \frac{\partial k_{eff}}{\partial a}}{\left[26 H_t k_b + 35 H_b k_{eff}\right]^2} \tag{2.65}$$

The computation of the $\partial \tilde{a}/\partial a$ field can be achieved by differentiating the regularization PDE 2.23 w.r.t a and with the help of expression 2.31. To numerically solve the resulting equation:

$$-\left(\frac{R}{2\sqrt{3}}\right)^2 \frac{\partial}{\partial x_j}\left[\frac{\partial}{\partial x_j}\left(\frac{\partial \tilde{a}}{\partial a}\right)\right] + \frac{\partial \tilde{a}}{\partial a} = 1 \tag{2.66}$$

$$\frac{\partial \tilde{a}}{\partial a} = 0 \tag{2.67}$$

a zero Dirichlet condition is imposed on $\partial\tilde{a}/\partial a$, at all wall boundaries of the design space. It is noted that the computational cost for solving the regularization PDE 2.23 as well as equation 2.66 is negligible compared to the solution of the primal and adjoint problems.

Finally, it is interesting to mention that the first volume integral in equation 2.60 includes the dot product of the primal and adjoint velocity vector fields. Considering that all multipliers of $u_i v_i$ are positive (because of the nature of equation 2.66, the value of $\partial\tilde{a}/\partial a$ will be positive across the entirety of the computational domain), when the two vectors form an acute angle the local areas of the design space tend to solidify and on the contrary when they form an obtuse angle the local porosity values tend to decrease. The same holds true for the dot product of the gradients of the primal and adjoint temperatures T and T_a appearing in the second volume integral of equation 2.60. This time, when the two gradients form an acute angle the local porosity values decrease and when they form an obtuse angle the local areas of the design space begin to solidify.

2.4 The SQP Update Method

The sequential quadratic programming (SQP) [3] is the employed gradient-based method used to update the design variables during the TopO process and is a technique particularly suited for solving large-scale nonlinear constrained optimization problems. In the TopO problems studied in this thesis, no constraint functions will be used, and thus a simplified version of SQP will be presented here with only bound constraints for the design variables. In the discrete space, the continuous real-valued porosity field $a \in [0, 1]$ is represented by the vector $\boldsymbol{b}$ formed by the porosity values at each mesh cell. The Quadratic Problem (QP) can be written as:

$$\min_{p_i} \quad \left(\frac{1}{2} p_i H_{i,j} p_j + G_i p_i\right) \tag{2.68a}$$

$$\text{s.t.} \quad l_i - b_i - p_i < 0 \tag{2.68b}$$

$$b_i + p_i - u_i < 0 \tag{2.68c}$$

where p_i is the update of the design variables b_i with $i \in [1, N]$, $G_i = \delta F/\delta b_i$

is the derivative of the objective function F w.r.t the design variables and $H_{i,j}$ an approximation to its Hessian matrix. In addition $l_i = 0, u_i = 1$ are the bound constrains of the design variables written as $l_i \leq b_i \leq u_i$. The Lagrangian of the above QP is:

$$L = \frac{1}{2} p_i H_{i,j} p_j + G_i p_i - \widetilde{l_i}(b_i + p_i - l_i) - \widetilde{u_i}(u_i - b_i - p_i) \tag{2.69}$$

where $\widetilde{l_i}$ and $\widetilde{u_i}$ are positive Lagrange multipliers. Taking complementary slackness into consideration, the KKT conditions are expressed as follows:

$$\frac{\partial L}{\partial p_i} = H_{i,j} p_j + G_i - \widetilde{l_i} + \widetilde{u_i} = 0 \tag{2.70a}$$

$$-b_i - p_i + l_i \leq 0 \tag{2.70b}$$

$$b_i + p_i - u_i \leq 0 \tag{2.70c}$$

$$\widetilde{l_i} l s_i = 0 \quad \forall i \tag{2.70d}$$

$$\widetilde{u_i} u s_i = 0 \quad \forall i \tag{2.70e}$$

where $ls_i > 0, us_i > 0$ the slack variables. The above non-linear system of equations is solved iteratively using a Newton method to compute the correction p_i^κ, where κ is the optimization cycle counter, to update the design variables as:

$$b_i^{\kappa+1} = b_i^\kappa + p_i^\kappa \tag{2.71}$$

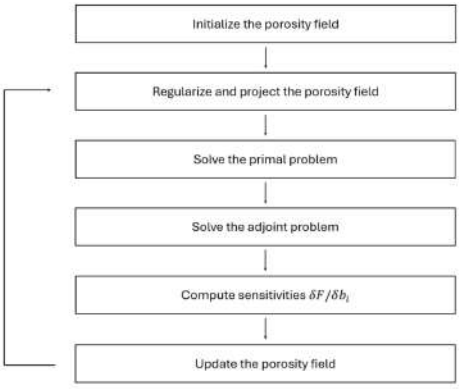

Figure 2.4: *Workflow of the TopO algorithm.*

Chapter 3

Case Studies

3.1 2.5D vs 3D: Adequacy of the 2.5D Model

A simple and approximate way to test the adequacy of the 2.5D model in resolving the heat transfer process, is to create random geometries with different substrate-fin configurations and compare the results against full 3D CHT simulations across different pressure gradients. This step is crucial, since the 2.5D model is the primal solver of the TopO process, and thus it is important to ensure it is capable of evaluating the thermal efficiency of the heat sink with an acceptable degree of accuracy.

For the full 3D simulations, separate 3D body-fitted meshes are generated, through the snappyHexMesh utility in OpenFOAM, for the fluid domain and solid domain which includes both the substrate and fins. The girds are unstructured and made up of hexahedral and split-hexahedral elements. On the contrary, for the 2.5D simulations, a single, structured, uniform Cartesian 2D mesh consisting of hexahedral elements is generated, through the blockMesh utility in OpenFOAM. Using this mesh, both the fluid and substrate solid regions are solved, but this time the 2.5D model considers the fins part of the fluid region. Since the geometry and location of the fins is known a priori, the cells that correspond to fins are given a fixed unitary porosity value, while the rest of the grid cells are given a fixed porosity value of zero. It is important to ensure that, for the 2.5D cases, the overall mesh refinement is enough to appropriately approximate the geometry of the fins and that no regularization and projection of the porosity field will be performed, so that the comparison between the 3D and 2.5D results will be valid.

A one inlet-two outlet (1I2O) microchannel heat sink was selected, with

water as the cooling fluid and aluminum nitride as the solid material of the substrate and fins. Water has a high thermal capacity under constant pressure and is one the most basic cooling fluids, while aluminum nitride is an electrically insulating ceramic material with high thermal conductivity, making it well suited for microchannel heat sink substrates in electronics cooling applications. The two different fin layouts that were tested, were built at random and are depicted in fig. 3.1, while visual representation of how the fin geometry is captured in the Cartesian mesh for the 2.5D cases is provided in fig. 3.2. The CHT problem was solved for (inlet-to-outlet) pressure drops of $\Delta p = 50Pa$ and $\Delta p = 400Pa$ and the water inlet temperature was set at $300K$. The uniform heat flux $\dot{q_o}$ was applied to the entire bottom surface of the substrate. Table 3.1 contains more case-specific information, like fluid and solid properties as well as key geometric characteristics.

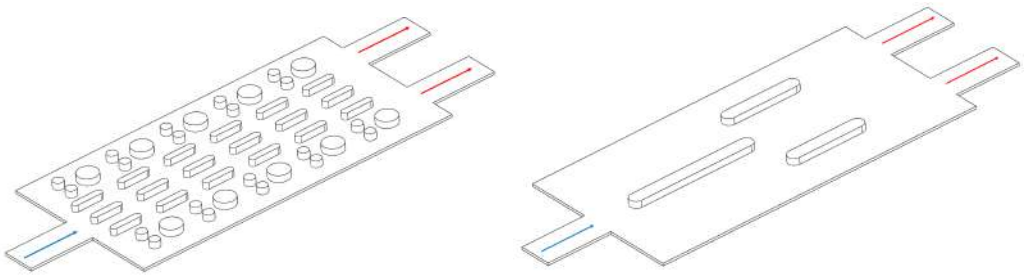

(a) *Fl1* **(b)** *Fl2*

Figure 3.1: *1I2O: Graphical representation of the microchannel heat sink's substrate with fin layouts Fl1 and Fl2.*

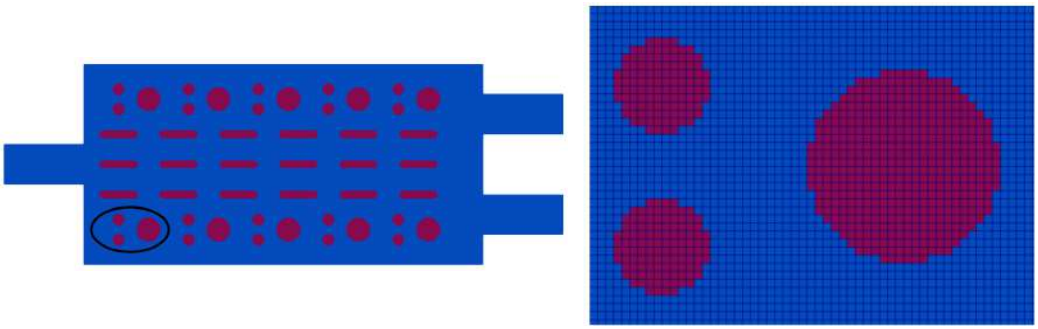

Figure 3.2: *1I2O-Fl1 (2.5D): Fin geometry approximation in the 2D structured Cartesian mesh. This is how the 2.5D model sees the fins - not strictly as solid bodies, but as areas in the mesh with unitary local porosity values.*

Figs. 3.3, 3.4, 3.5, 3.6, 3.7 and 3.8 depict the resulting velocity and temperature fields on the mid-plane of the fluid and substrate regions, from the 3D and 2.5D simulations. Since the 2.5D model solves for the temperature field on the middle of the substrate region and the velocity field on the mid-plane of the fluid region, it is convenient for the comparison against the 3D results

to be performed on the mid-plane of the substrate and fluid regions. The temperature field on the mid-plane of the fluid region can be derived from the computed primal field T with the help of equation 2.10. Tables 3.2, 3.3 and 3.4 respectively show the computed maximum temperature $T_{b,max}$ and average temperature $T_{b,avg}$ appearing on the middle of the substrate as well as the inlet mass flow rate $\dot{m}_I$ for all cases.

Variable	Value
M	100
H_t	0.20 mm
H_b	0.075 mm
$\dot{q_o}$	75000 W/m^2
ρ	998.2 kg/m^3
μ	0.001002 $P_a \cdot s$
C_p	4182 $J/kg \cdot K$
k_f	0.598 $W/m \cdot K$
k_b	150 $W/m \cdot K$

Mesh	Cell Count
Fl1 - Fluid Domain (3D)	2586967
Fl1 - Solid Domain (3D)	1285371
Fl2 - Fluid Domain (3D)	2639033
Fl2 - Solid Domain (3D)	1190718
Fl1/Fl2 Cartesian Mesh (2.5D)	89600

Table 3.1: *1I2O-FL1/FL2: Case-specific details for 3D and 2.5D simulations. Solid and fluid properties as well as heat flux $\dot{q_o}$ are common between 2.5D and 3D simulations. Variables M, H_t and H_b are only used for the 2.5D simulations.*

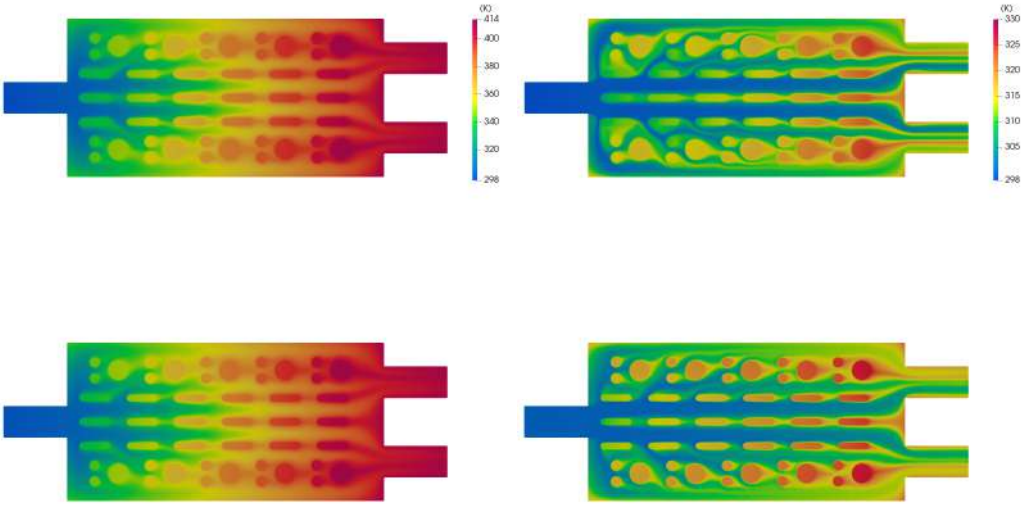

(a) $50Pa$ **(b)** $400Pa$

Figure 3.3: *1I2O-Fl1: Temperature field on the mid-plane of the fluid region from the 2.5D simulation (upper figs.) and the full 3D simulation (lower figs.).*

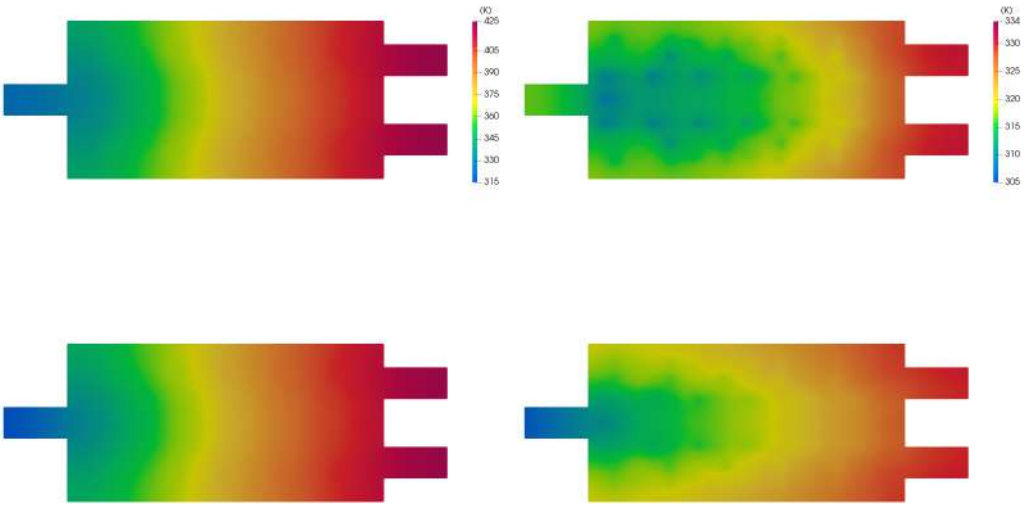

(a) $50Pa$ **(b)** $400Pa$

Figure 3.4: *1I2O-Fl1: Temperature field on the mid-plane of the substrate region from the 2.5D simulation (upper figs.) and the full 3D simulation (lower figs.).*

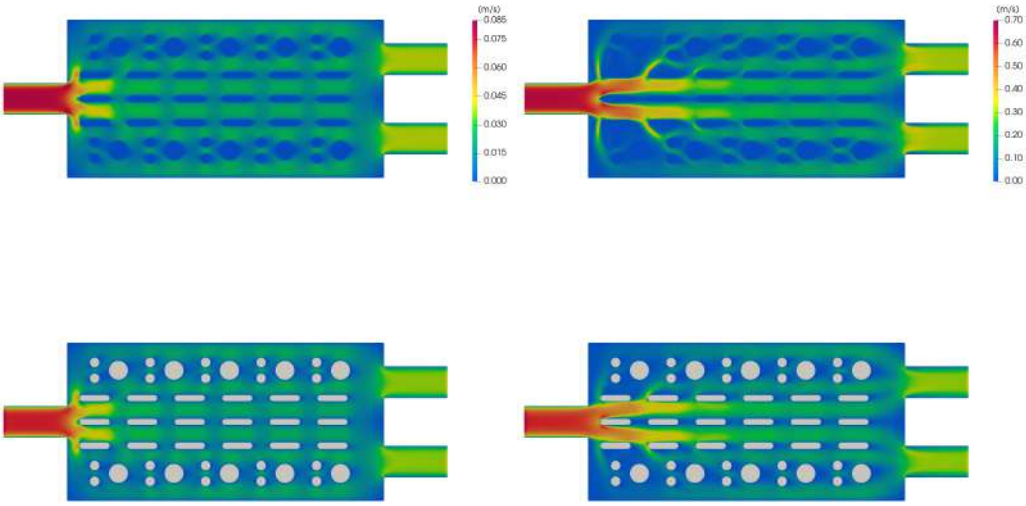

(a) $50Pa$ **(b)** $400Pa$

Figure 3.5: *1I2O-Fl1: Velocity field on the mid-plane of the fluid region from the 2.5D simulation (upper figs.) and the full 3D simulation (lower figs.).*

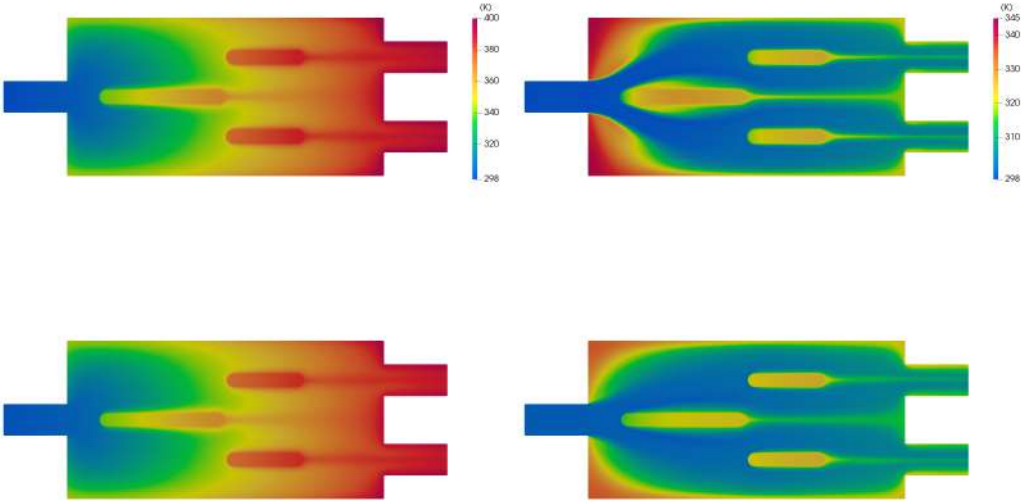

(a) $50Pa$ **(b)** $400Pa$

Figure 3.6: *1I2O-Fl2: Temperature field on the mid-plane of the fluid region from the 2.5D simulation (upper figs.) and the full 3D simulation (lower figs.).*

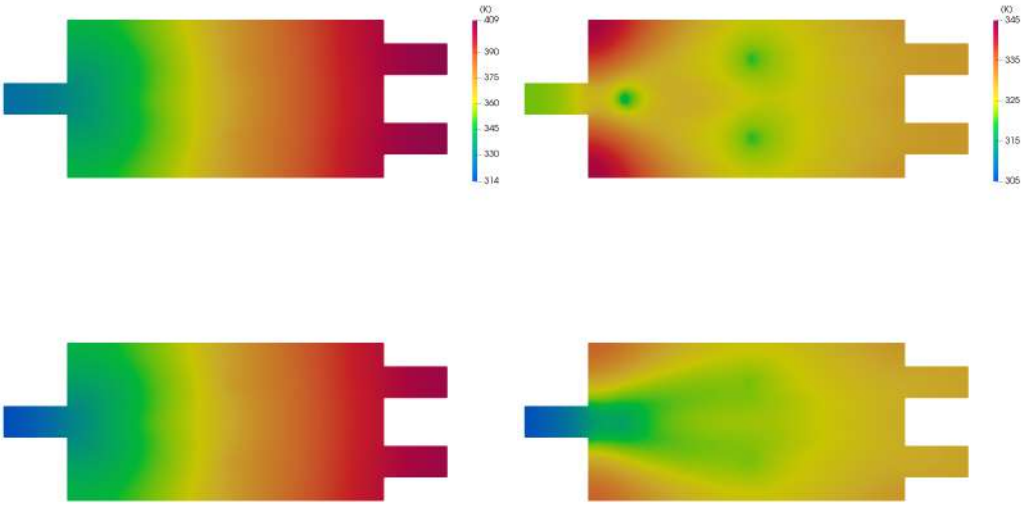

(a) $50Pa$ **(b)** $400Pa$

Figure 3.7: *1I2O-Fl2: Temperature field on the mid-plane of the substrate region from the 2.5D simulation (upper figs.) and the full 3D simulation (lower figs.).*

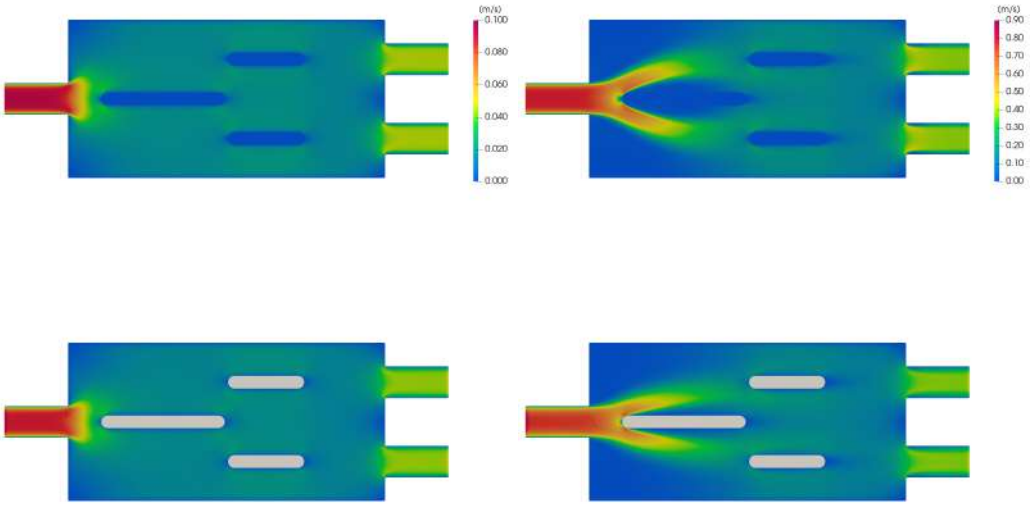

(a) $50Pa$ **(b)** $400Pa$

Figure 3.8: *1I2O-Fl2: Velocity field on the mid-plane of the fluid region from the 2.5D simulation (upper figs.) and the full 3D simulation (lower figs.).*

Considering figs. 3.3, 3.4, 3.5, 3.6, 3.7 and 3.8 and tables 3.2, 3.3, 3.4, the following conclusions can be reached:

1. Irrespective of the geometry, the 2.5D model predicts more accurately the temperature fields for low pressure drops and the error becomes greater as the pressure gradient increases. This is because the assumption of the fully developed flow, fails increasingly as pressure drops get bigger. Especially, the non-dimensional temperature profile given by expression 2.10. used to derive the temperature on the mid-plane of the fluid region from the computed T field, is not valid for a flow that is still developing. As mentioned in [13], this is the reason that, sometimes, when trying to derive temperature fields on a constant x_3 plane, areas with local temperatures lower that the fluid's inlet temperature are observed in the fluid region, which is non physical.

2. The 2.5D model agrees with the 3D results as to which fin layout is more thermally efficient at a certain operating point of the heat sink. For the low pressure gradient of $50Pa$ the fin layout Fl1 performs worse than Fl2, despite the higher number of fins. At such a low pressure drop, the resulting inlet mass flow rate is so small that convection cannot benefit from the extra surface area provided by the higher number of fins. In such conditions even the slightly higher achieved mass flow rate for the fin layout Fl2 makes a difference. At the relatively larger

pressure gradient of $400Pa$, convection is better utilized and now the Fl1 fin configuration is the more thermally efficient one.

Case	1I2O-Fl1			1I2O-Fl2		
$\Delta p\,(Pa)$	2.5D $T_{b,max}\,(K)$	3D $T_{b,max}\,(K)$	Relative Error	2.5D $T_{b,max}\,(K)$	3D $T_{b,max}\,(K)$	Relative Error
50	421.99	421.32	0.55%	407.46	404.75	2.59%
400	330.70	330.12	1.93%	342.86	334.83	23.05%

Table 3.2: *1I2O-Fl1/Fl2: Computed maximum temperature $T_{b,max}$ appearing on the middle of the substrate.*

Case	1I2O-Fl1			1I2O-Fl2		
$\Delta p\,(Pa)$	2.5D $T_{b,avg}\,(K)$	3D $T_{b,avg}\,(K)$	Relative Error	2.5D $T_{b,avg}\,(K)$	3D $T_{b,avg}\,(K)$	Relative Error
50	377.89	378.43	0.69%	370.78	369.18	2.31%
400	318.57	320.59	9.81%	327.77	324.73	12.29%

Table 3.3: *1I2O-Fl1/Fl2: Computed average temperature $T_{b,avg}$ appearing on the middle of the substrate.*

Case	1I2O-Fl1			1I2O-Fl2		
$\Delta p\,(Pa)$	2.5D $\dot{m}_I\,(g/s)$	3D $\dot{m}_I\,(g/s)$	Relative Error	2.5D $\dot{m}_I\,(g/s)$	3D $\dot{m}_I\,(g/s)$	Relative Error
50	0.0369	0.0371	0.54%	0.0432	0.0444	2.7%
400	0.299	0.297	0.67%	0.364	0.371	1.89%

Table 3.4: *1I2O-Fl1/Fl2: Computed inlet mass flow rate $\dot{m}_I$ of the heat sink.*

In the above tables the relative error for the maximum temperature $T_{b,max}$ appearing on the mid-plane of the substrate was computed as:

$$\frac{\left|T_{b,max}^{3D} - T_{b,max}^{2.5D}\right|}{T_{b,max}^{3D} - T_I} \tag{3.1}$$

with the same equation used for calculating the relative error for the averaged temperature, by replacing $T_{b,max}$ with $T_{b,avg}$. The relative error for the calculated inlet mass flow rate between the 3D and 2.5D solutions was found using the formula:

$$\frac{\left|{\dot{m}_I}^{3D} - {\dot{m}_I}^{2.5D}\right|}{{\dot{m}_I}^{3D}} \tag{3.2}$$

Even if the geometry of the fins was exactly captured in the Cartesian mesh for the 2.5D cases, differences from the 3D results are inevitable since the 2.5D model is made as a primal solver for a TopO algorithm and thus the fins in the fluid region are not considered as strict solid boundaries. The no-slip boundary condition for the velocity is set indirectly through the Brinkman penalization terms and not explicitly imposed during the solution of the flow problem. Finally even though the 2.5D model retains part of the information from the neglected height dimension, it of course doesn't give the same level of accuracy as fully resolving the flow problem across all three dimensions. Nevertheless, from the above, it becomes clear that the 2.5D primal solver is capable of evaluating thermal performance and can thus be used in a TopO process to gradually lead the algorithm to a heat sink geometry that has optimal thermal performance at a given operating point.

3.2 Application to TopO Problems

In this section, TopO of microchannel heat sinks will be performed using the 2.5D model. The (normalized) maximum temperature appearing in the substrate region is the objective function of the TopO process which is computed using the p-norm aggregation function 2.28 and is rewritten here in its discrete form:

$$F = \left[\sum_{i=1}^{N} \left(\frac{T_{b_i}}{T_{ref}} \right)^p \right]^{\frac{1}{p}} \tag{3.3}$$

where N is the total number of mesh cells in Ω. The optimization runs for a maximum of 300 cycles or until the relative change in the value of the objective function between successive optimization cycles becomes less than a very small number, namely:

$$\frac{F^{\kappa+1} - F^{\kappa}}{F^{\kappa}} < 10^{-6} \tag{3.4}$$

In TopO problems, volume constraints, which limit how much from the overall domain volume can be occupied by fluid or solid material, are frequently employed. From a design point of view, such constraints are often implemented to ensure practical, manufacturable and cost efficient designs where a balance is struck between performance and solid material used. The volume constraints also help guide the TopO algorithm and prevent trivial solutions from arising with only fluid or only solid materials filling the entirety of the design space. In the theoretical study of the TopO applications considered in

this thesis, however, it is desired to give the algorithm the freedom to decide how many fins, i.e. how much solid material, to place inside the fluid region depending on the heat sink's operating conditions. As a result no volume constraints will be imposed to any of the TopO problems in the following subsections.

3.2.1 The 1I1O and 1I2O CHT TopO Problems

Microchannel heat sinks with a one inlet-one outlet (1I1O) and 1I2O configurations are designed with water as the cooling fluid and aluminum nitride as the solid material for the substrate and fins. The 1I1O heat sinks are designed for pressure drops of $400Pa$ and $800Pa$, while the 1I2O ones for pressure drops of $200Pa$ and $400Pa$. Depending on the pressure gradient that the heat sink is designed to work at, different optimal geometries are expected to arise. The computational domains for both problems are depicted in fig. 3.9, while the initialization of the porosity field is shown in fig. 3.10.

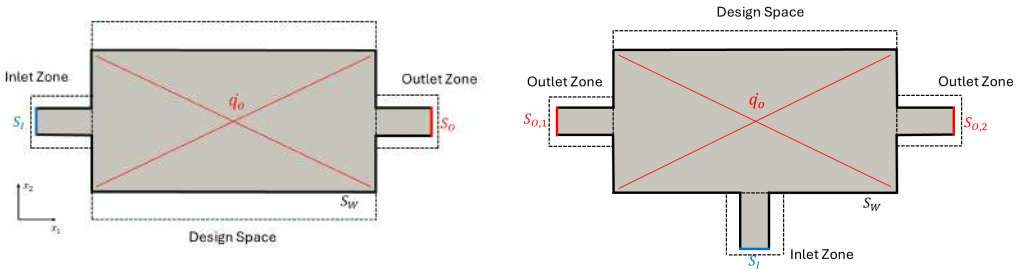

(a) *1I1O-TopO* **(b)** *1I2O-TopO*

Figure 3.9: *1I1O/1I2O-TopO: Computational domain with the inlet boundary S_I, outlet boundary S_O, wall boundary S_W and design space. For the 1I2O-TopO case, $S_O = S_{O,1} \cup S_{O,2}$*

The inlet and outlet zones are fixed porous zones that are always occupied by fluid and do not belong to the design space of the optimization. Consequently the cells that correspond to these zones have a fixed porosity value of zero during the TopO process. The constant uniform heat flux $\dot{q}_o$ is applied to the part of the substrate that corresponds to the design space of the optimization. The inlet water temperature was set at $300K$, while more case-specific information, including parameter values for the regularization and projection of the porosity field are presented in table 3.5.

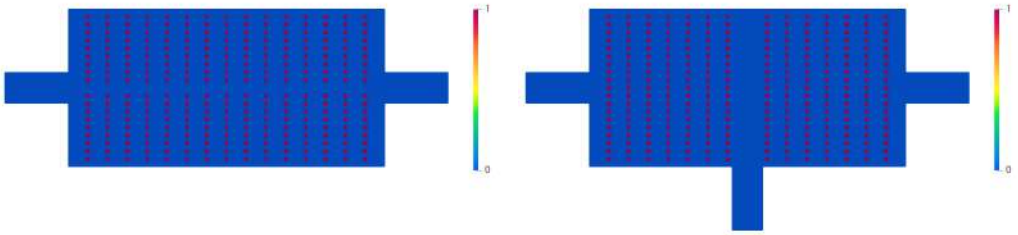

(a) *1I1O-TopO* **(b)** *1I2O-TopO*

Figure 3.10: *1I1O/1I2O-TopO: Initialization of the porosity field a. Zero porosity values indicate fluid while unitary porosity values correspond to solid material.*

Variable	Value
b	10
m_R	5
λ	10
M	100
p	10
T_{ref}	$300K$
$\dot{q_o}$	75000 W/m^2
H_t	0.20 mm
H_b	0.075 mm
ρ	998.2 kg/m^3
μ	0.001002 $P_a \cdot s$
C_p	4182 $J/kg \cdot K$
k_f	0.598 $W/m \cdot K$
k_b	150 $W/m \cdot K$
Mesh Cell Count (1I1O-TopO/1I2O-TopO)	21600/22000

Table 3.5: *1I1O/1I2O-TopO: Case-specific details.*

Convergence of the TopO algorithm can be seen in fig. 3.11. The value of the objective function decreases rapidly in the first cycles and then steadily declines, indicating consistent progress toward an optimal design. The convergence behavior is similar for both pressure load cases, across both CHT problems.

Figs. 3.12 and 3.13 show the optimal 1I1O and 1I2O heat sink geometries that resulted from the TopO process, respectively. These geometries were constructed by extracting the interfaces between the fluid and fins, i.e. extracting the isolines of the β field, to produce 3D extruded surfaces. It can be seen that for lower pressure drops the number of fins that are formed inside

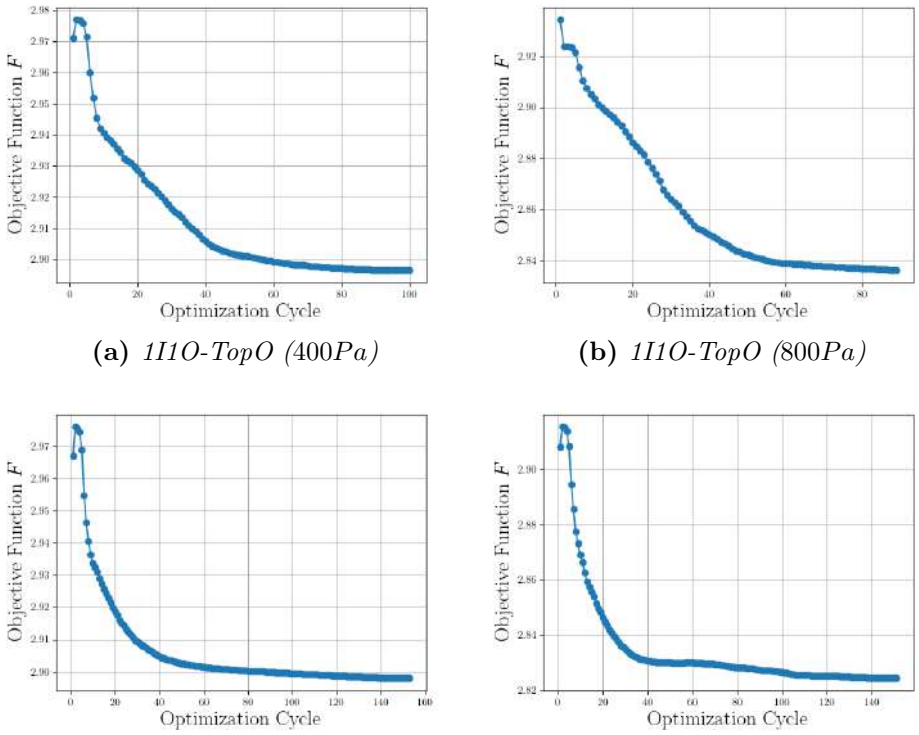

(a) *1I1O-TopO (400Pa)* **(b)** *1I1O-TopO (800Pa)*

(c) *1I2O-TopO (200Pa)* **(d)** *1I2O-TopO (400Pa)*

Figure 3.11: *1I1O/1I2O-TopO: Progress of the TopO algorithm.*

the fluid region is much smaller, because of the weaker force that drives the flow. The algorithm tries to utilize conduction and convection, by placing as many fins as possible in strategic locations to maximize the surface area without increasing the hydraulic resistance too much and choking the flow. It is also observed that the algorithm creates solid material around the wall boundaries belonging in the design space of Ω and smoothens the corners of the computational domain to further aid the flow.

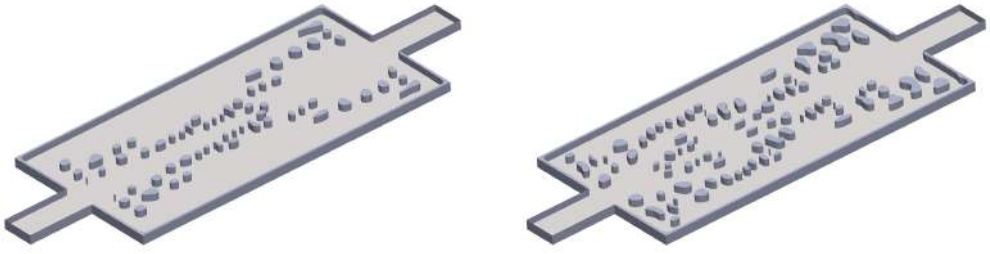

(a) $400Pa$ **(b)** $800Pa$

Figure 3.12: *1I1O-TopO: Optimized heat sink geometries. The substrate and fins are made of the same solid material, however they are presented with different colors for visualization purposes.*

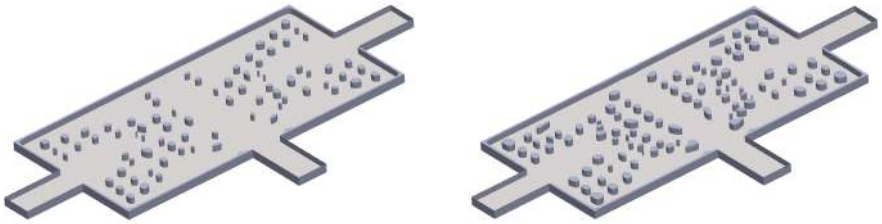

(a) $200Pa$ **(b)** $400Pa$

Figure 3.13: *1I2O-TopO: Optimized heat sink geometries. The substrate and fins are made of the same solid material, however they are presented with different colors for visualization purposes.*

Figs. 3.14, 3.15, 3.16 and 3.17 depict the resulting primal velocity and temperature fields of the fluid and substrate regions for the optimized 1I1O and 1I2O heat sinks, where intriguing flow patterns can be observed. In addition, figs. 3.18 and 3.19 show the corresponding optimal β fields. An indicator of the heat sink's ability to reject heat is its thermal resistance R_{th} which expresses the temperature rise (K) in the substrate relatively to the fluid inlet temperature per unit of heat input (W) and is given by equation:

$$R_{th} = \frac{T_{b,max} - T_I}{\dot{Q}} = \frac{T_{b,max} - T_I}{\dot{q_o} A} \tag{3.5}$$

where $\dot{Q}$ is the total heat fed into the heat sink and A the area of the substrate, where the heat flux $\dot{q_o}$ is applied. Table 3.6 includes the aforementioned performance metric and the calculated inlet mass flow rate $\dot{m}_I$, while table 3.7 contains the computed Reynolds and Peclet numbers, for the designed microchannel heat sinks. Based on the Reynolds and Peclet values, the flow is indeed laminar and the designed heat sinks work within the forced convection regime.

Pressure Drop (Pa)	Thermal Resistance $R_{th}\,(K/W)$	$\dot{m}_I\ (g/s)$
1I1O-TopO		
400	2.02	0.194
800	1.45	0.292
1I2O-TopO		
200	2.05	0.193
400	1.21	0.355

Table 3.6: *1I1O/1I2O-TopO: Thermal resistance and inlet mass flow rate for the designed heat sinks. The lower the value of R_{th}, the better the thermal performance of the heat sink. It is observed that for the same operating conditions (e.g., pressure drop of $400Pa$) the 1I2O configuration is more thermally efficient.*

Pressure Drop (Pa)	Reynolds Number Re	Peclet Number Pe
1I1O-TopO		
400	161.42	1129.97
800	242.97	1700.78
1I2O-TopO		
200	160.59	1124.15
400	295.39	2067.73

Table 3.7: *1I1O/1I2O-TopO: Computed Reynolds and Peclet numbers for the designed heat sinks. The average inlet velocity and inlet hydraulic diameter (which also takes into account the height of the fluid region H_t) were used as characteristic quantities for the computation of the dimensionless numbers. Generally, for internal flows a $R_e < 2300$ typically indicates laminar flow, while for $P_e > 100$ heat transfer is dominated by convection. Forced convection heat sinks often have a Peclet number greater than 1000, depending on cooling fluid, flow velocity and geometry.*

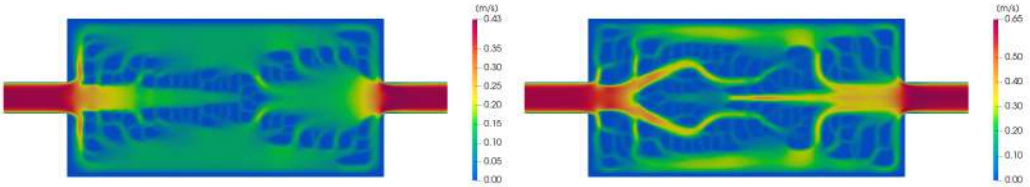

(a) $400Pa$ **(b)** $800Pa$

Figure 3.14: *1I1O-TopO: Primal velocity field of the fluid region for the designed heat sinks.*

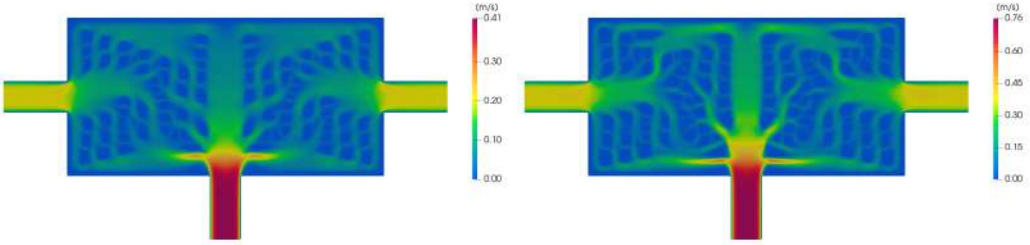

(a) $200Pa$ **(b)** $400Pa$

Figure 3.15: *1I2O-TopO: Primal velocity field of the fluid region for the designed heat sinks.*

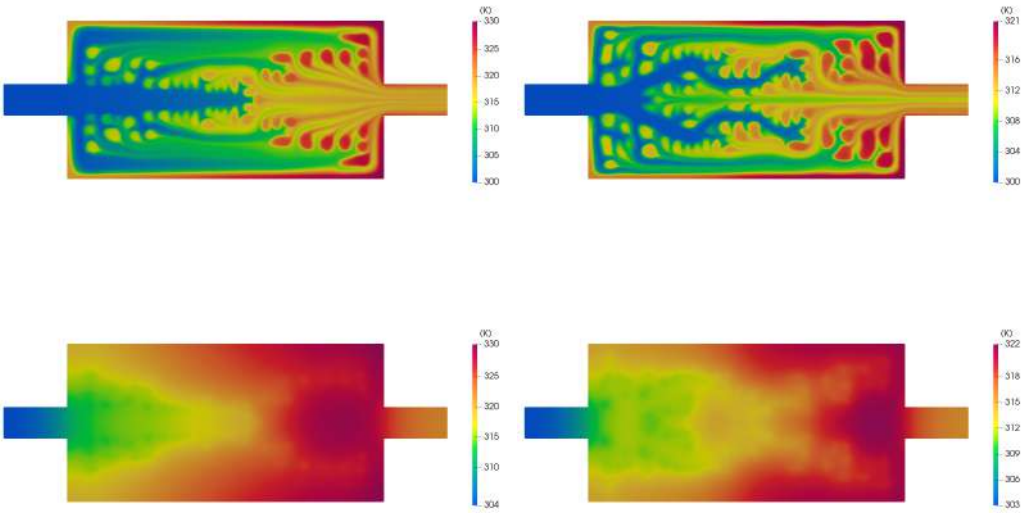

(a) $400Pa$ **(b)** $800Pa$

Figure 3.16: *1I1O-TopO: Primal temperature field of the fluid region (upper figs.) and substrate region (lower figs.) for the designed heat sinks.*

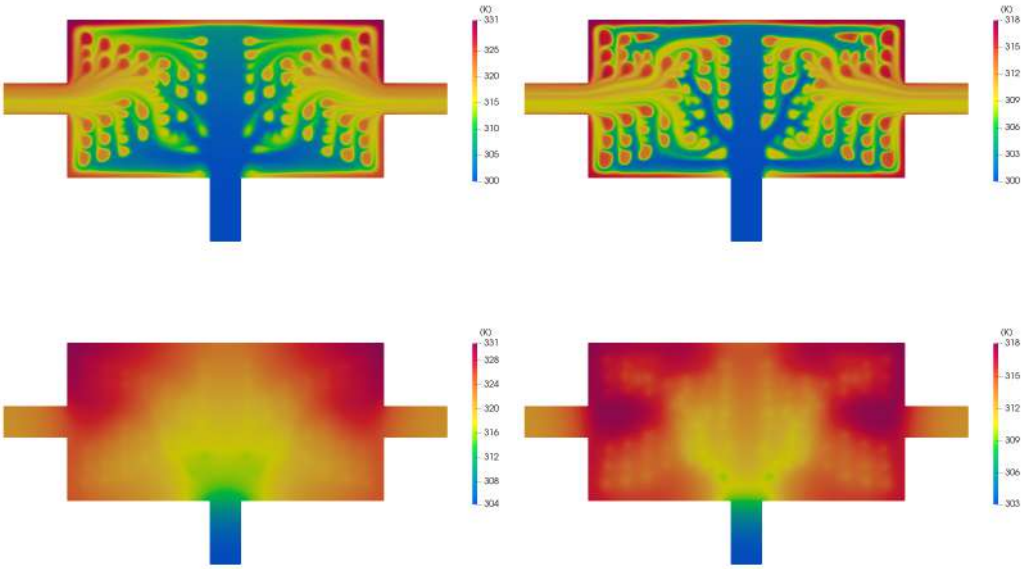

(a) $200Pa$ **(b)** $400Pa$

Figure 3.17: *1I2O-TopO: Primal temperature field of the fluid region (upper figs.) and substrate region (lower figs.) for the designed heat sinks.*

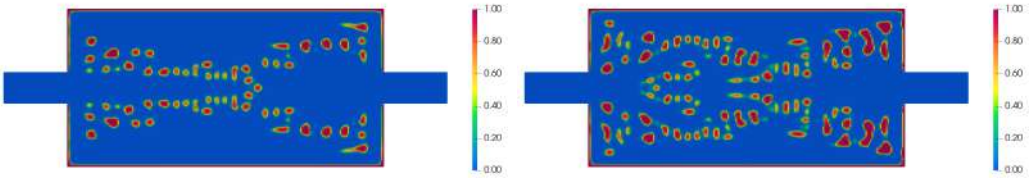

(a) $400Pa$ **(b)** $800Pa$

Figure 3.18: *1I1O-TopO: Optimal β fields for the designed heat sinks.*

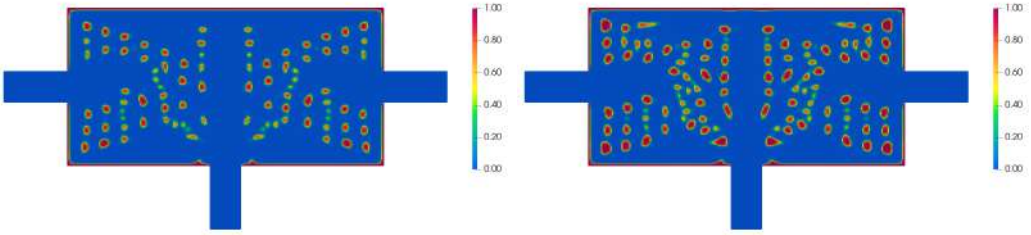

(a) $200Pa$ **(b)** $400Pa$

Figure 3.19: *1I2O-TopO: Optimal β fields for the designed heat sinks.*

The results from both the 1I1O and 1I2O CHT TopO problems, clearly demonstrate the fundamental advantage of microchannel heat sinks: high thermal performance (low R_{th} values) can be achieved even with low inlet mass flow rates. This highlights the efficiency of microscale convective cooling, where the high surface area-to-volume ratio enables effective heat transfer. Such characteristics make microchannel heat sinks highly attractive for compact, low-power cooling solutions in modern electronics, where energy efficiency and spatial constraints are critical.

3.2.2 The Varying Heat Flux (VHF) Application

In real world practical applications, the bottom surface of the heat sink's substrate is not uniformly heated, but rather, hot spots are observed in certain areas corresponding to the location of chips on the electronic board. Therefore it would be interesting to study the case where the heat flux $\dot{q}_o$ is applied locally and not to the entire part of the substrate that corresponds to the design space. The microchannel heat sink with the 1I1O configuration as presented in subsection 3.2.1 is studied, and designed once again for pressure drops of $400Pa$ and $800Pa$. The case setup and initialization of the porosity

field are also identical to the ones presented in the previous subsection, with the exception that $\dot{q_o}$ is non-uniform this time.

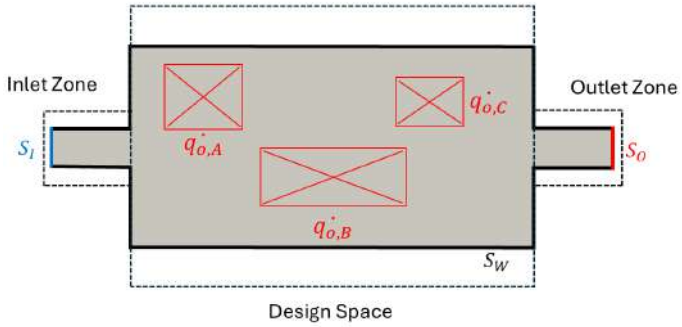

Figure 3.20: *1I1O(VHF)-TopO: Computational domain with the inlet boundary S_I, outlet boundary S_O, wall boundary S_W and design space with locally heated areas.*

Variable	Value
$q_{o,A}^{\cdot}$	180000 W/m^2
$q_{o,B}^{\cdot}$	200000 W/m^2
$q_{o,C}^{\cdot}$	150000 W/m^2

Table 3.8: *1I1O(VHF)-TopO: Local heat fluxes generated from chipsets A,B and C on the electronic board.*

As evident from the resulting optimal geometries in fig. 3.22, this time the fins are less spread out in the entirety of the design space and are instead concentrated around the areas where heat fluxes are applied. The algorithm tries to maximize convective surface area at critical hot spots, so as heat is transferred from these hot spots to the solid fins through conduction and then carried away by the flow through convection. Similar to the cases with the uniform heat flux $\dot{q_o}$, a higher number of fins is observed for the heat sink designed to work at the greater pressure gradient.

The thermal resistance of the heat sinks is again computed using equation 3.5, where the total heat input $\dot{Q}\,(W)$ is now calculated as:

$$\dot{Q} = q_{o,A}^{\cdot} A_A + q_{o,B}^{\cdot} A_B + q_{o,C}^{\cdot} A_C \tag{3.6}$$

with A_A, A_B, A_C being the surface areas in the substrate where the corresponding heat fluxes are applied.

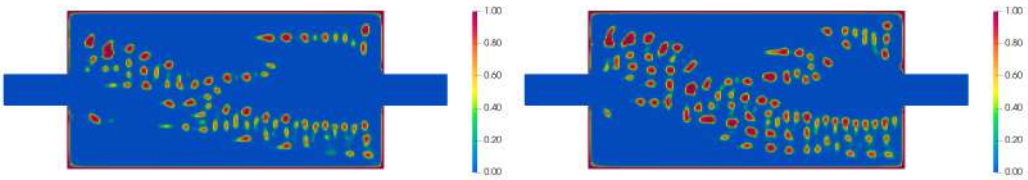

(a) $400Pa$ **(b)** $800Pa$

Figure 3.21: *1I1O(VHF)-TopO: Optimal β fields for the designed heat sinks.*

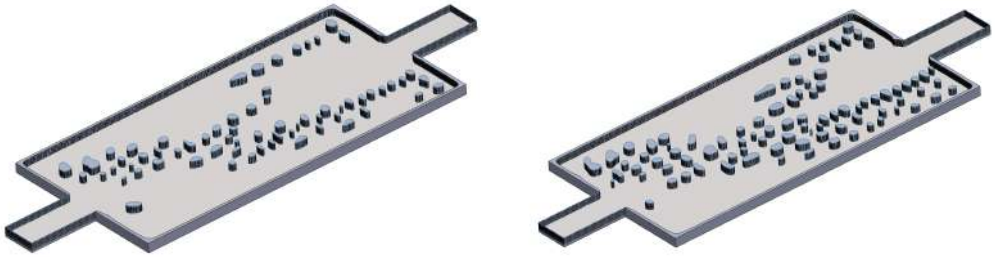

(a) $400Pa$ **(b)** $800Pa$

Figure 3.22: *1I1O(VHF)-TopO: Optimized heat sink geometries. The fins form less symmetric layouts and are instead gathered around the hot spots where heat flux is locally applied.*

Pressure Drop (Pa)	Thermal Resistance $R_{th}\,(K/W)$	$\dot{m}_I\ (g/s)$
400	2.89	0.182
800	2.04	0.285

Table 3.9: *1I1O(VHF)-TopO: Thermal resistance and inlet mass flow rate for the designed heat sinks.*

Pressure Drop (Pa)	Reynolds Number Re	Peclet Number Pe
400	151.44	1060.08
800	237.14	1660.01

Table 3.10: *1I1O(VHF)-TopO: Reynolds and Peclet numbers for the designed heat sinks.*

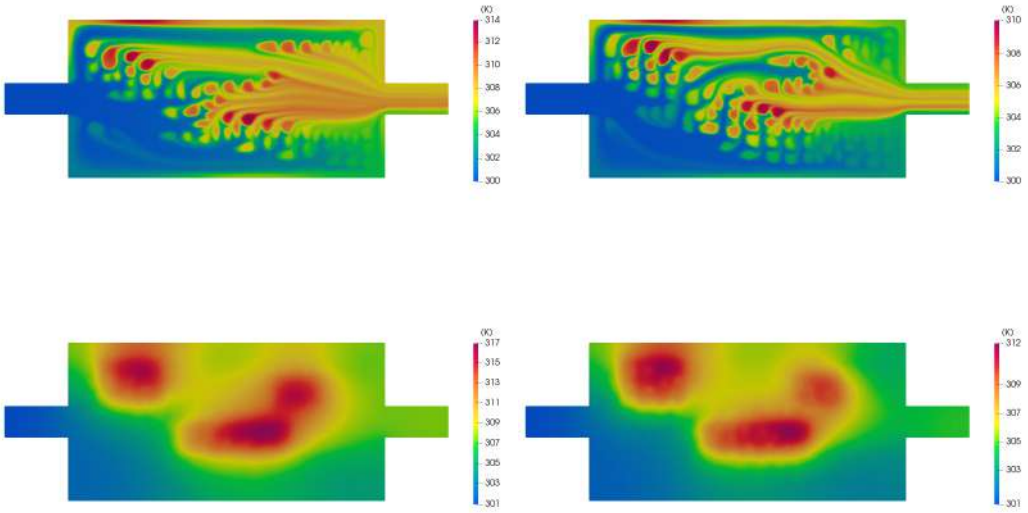

(a) $400P_a$ **(b)** $800P_a$

Figure 3.23: *1I1O(VHF)-TopO: Primal temperature field of the fluid region (upper figs.) and substrate region (lower figs.) for the designed heat sinks.*

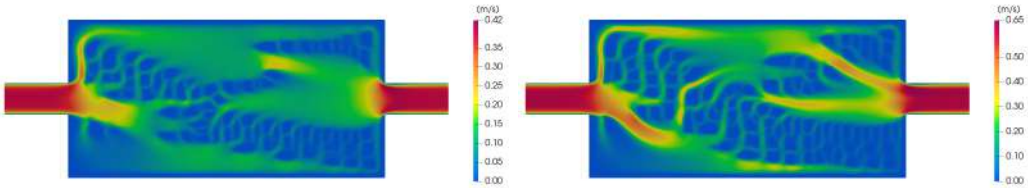

(a) $400P_a$ **(b)** $800P_a$

Figure 3.24: *1I1O(VHF)-TopO: Primal velocity field of the fluid region for the designed heat sinks.*

3.2.3 Porosity Field Initialization: Sensitivity Analysis

Gradient-based optimization methods heavily depend on the initial guess of the design variables and thus, in this subsection, a sensitivity analysis of the resulting optimal solution on the initialization of the porosity field will be performed. The 1I1O and 1I2O heat sinks presented in subsection 3.2.1 are once again selected and designed for pressure drops of $800Pa$ and $400Pa$ respectively. All case-specific details are the same as in subsection 3.2.1. In

figs. 3.26 and 3.27 the different initializations of the porosity field as well as the corresponding optimal solutions are depicted.

This time, instead of initializing the design space (fluid region) with a high number of small (in volume) solid areas like in subsections 3.2.1 and 3.2.2, few solid fins, with different layouts, that occupy a considerable part of the design space are selected. Even in this scenario, the algorithm still favors the formation of many small (in volume) fins to create as many microchannels as possible and increase the convective surface area.

Case	$T_{b,max}$ (K)	R_{th} (K/W)
1I1O(I1)-TopO	323.25	1.55
1I1O(I2)-TopO	320.57	1.371
1I2O(I1)-TopO	319.18	1.279
1I2O(I2)-TopO	318.42	1.228

Table 3.11: *1I1O(SA)/1I2O(SA)-TopO: Maximum temperature appearing in the substrate and calculated thermal resistance for the different optimized solutions.*

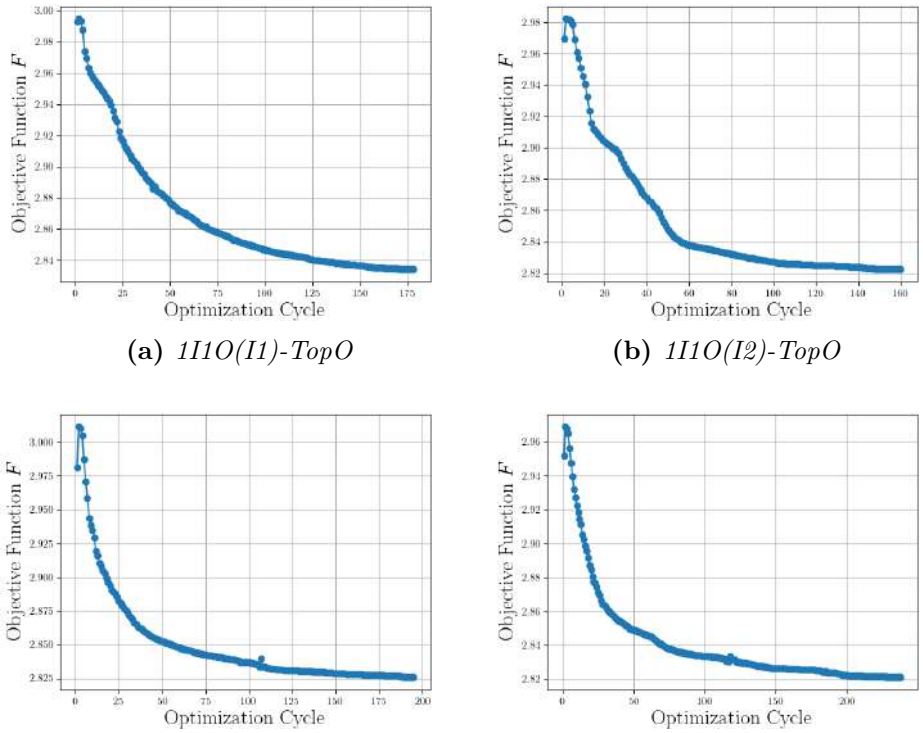

(a) *1I1O(I1)-TopO* **(b)** *1I1O(I2)-TopO*

(c) *1I2O(I1)-TopO* **(d)** *1I2O(I2)-TopO*

Figure 3.25: *1I1O(SA)/1I2O(SA)-TopO: Progress of the TopO algorithm.*

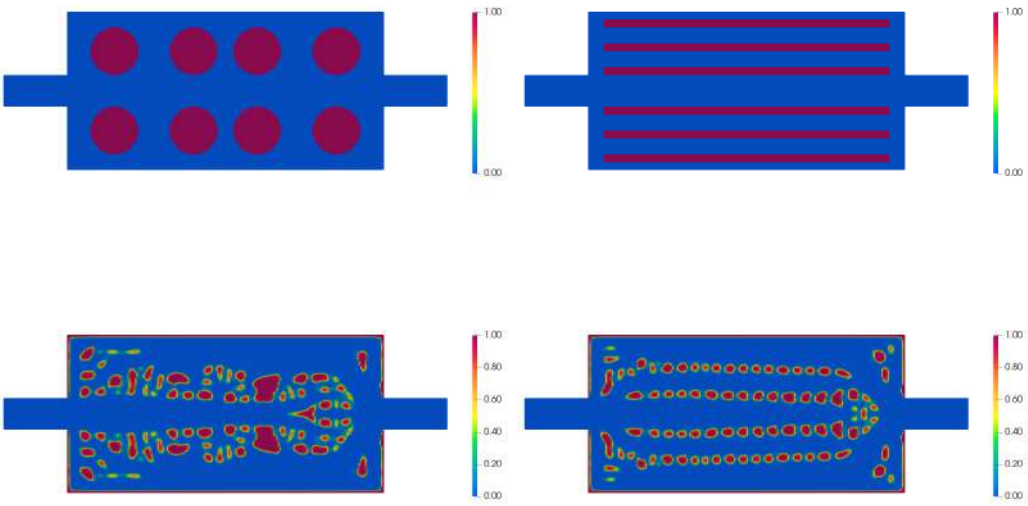

(a) *1I1O(I1)-TopO* **(b)** *1I1O(I2)-TopO*

Figure 3.26: *1I1O(SA)-TopO: Different initializations of the porosity field (upper figs.) and the corresponding optimal β fields (lower figs.) which resulted from the TopO process.*

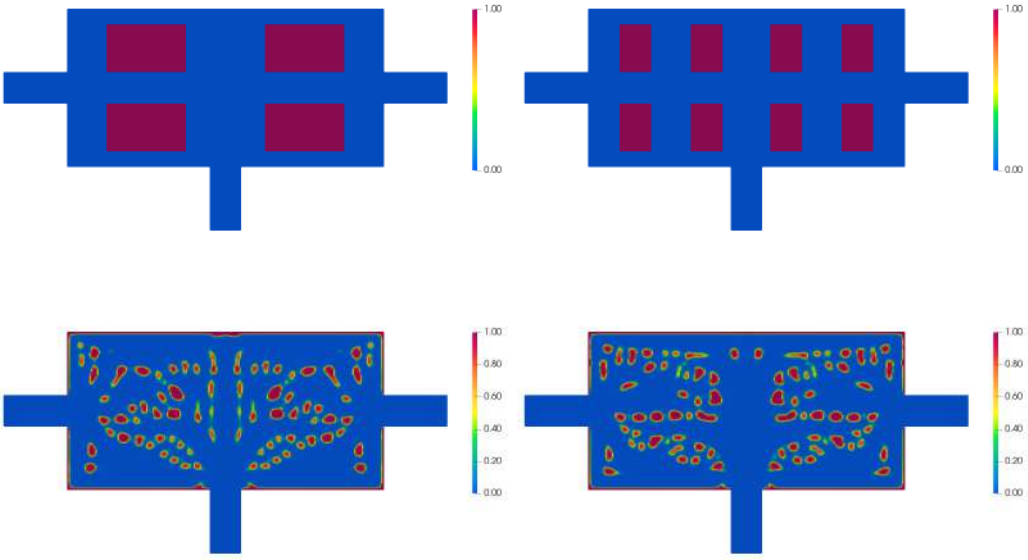

(a) *1I2O(I1)-TopO* **(b)** *1I2O(I2)-TopO*

Figure 3.27: *1I2O(SA)-TopO: Different initializations of the porosity field (upper figs.) and the corresponding optimal β fields (lower figs.) which resulted from the TopO process.*

Although the resulting optimal solution is affected by the initialization of the porosity field (the optimal fin layouts are not identical), the algorithm's trends remain the same. Moreover, based on the initial a field, the algorithm may require more cycles to reach an optimal design, as seen from fig. 3.25. Consequently, the computational cost of the TopO is also slightly affected. Finally, because no volume constraints were employed in the TopO cases studied in this thesis, the solution is even more sensitive to the initialization of the porosity field. Since there are no constraint functions to restrict the feasible design space, the algorithm is more prone to getting stuck on the closest local minimum.

Chapter 4

Closure-Conclusions

This thesis has explored the application of porosity-based TopO to the design of forced convection microchannel heat sinks. By integrating the governing equations across the geometry height while preserving lateral and streamwise resolution, the employed 2.5D CHT model [13] achieves a meaningful balance between computational efficiency and physical fidelity. Although the 2.5D model does not match the full accuracy of 3D simulations, it enables rapid iteration, parametric studies, and preliminary design evaluation without the prohibitive cost of full 3D computations. This makes it particularly useful for optimization processes, where hundreds of design evaluations may be required. In combination with using the continuous adjoint method to compute the sensitivity derivatives of the objective function at a cost independent of the number of design variables, the cost of the overall TopO process is drastically decreased.

However, it must be acknowledged that the accuracy of the 2.5D CHT model inherently depends on the validity of the assumptions made during the reduction process. Specifically, the results are more accurate for low pressure drops across the heat sinks, with the error getting increasingly higher for greater pressure gradients. This is due to the fully developed flow assumption, which does not hold true for high pressure drops. Furthermore, although an application was studied where the heat sink's substrate was locally heated, during the derivation of the temperature profiles the heat flux applied to the bottom surface of the substrate was assumed uniform. Therefore, the optimized geometries should always be re-evaluated with full 3D CHT simulations to get accurate temperature and velocity fields and cross-check the results against the ones produced from the 2.5D model.

Porosity-based TopO was employed to discover optimal microchannel heat sink geometries. Depending on the pressure gradient the heat sink was de-

signed to work at and whether the substrate was uniformly or locally heated, different optimal geometries were produced. The algorithm tends to place as many small fins as possible inside the fluid region to maximize convective surface area while keeping the hydraulic resistance at low levels to allow relatively considerable mass flow rates through the heat sink. Although different initializations of the porosity field lead to different optimized solutions, the aforementioned behavior of the algorithm was always observed (the trends remain the same). Evaluating the thermal performance of the optimized geometries, shows that efficient thermal dissipation is achieved even at low mass flow rates which is one of the major characteristics of microchannel heat sinks. The results also highlight the power of TopO in uncovering non-intuitive fin layouts that would be difficult or impossible to derive manually. Such outcomes reinforce the value of computational optimization in guiding modern engineering design. Nevertheless, porosity-based TopO is not without limitations and has its drawbacks, like the emergence of gray areas—regions of partial material presence that lack a clear physical interpretation. This can complicate both the manufacturing and interpretation of the optimized designs. Alternative TopO methods have been introduced in the literature, such as the level set method, which naturally tends to produce sharp interfaces and avoids gray regions.

In summary, this thesis demonstrates that the low computational cost 2.5D model proposed in [13] coupled with the continuous adjoint method, are highly complementary tools in TopO of microchannel heat sinks. When used together, they enable the efficient exploration of large design spaces and the discovery of novel engineering solutions.

Appendix A

2.5D Problem Formulation

This appendix contains the analytical derivation of the governing equations of the 2.5D CHT model used in this thesis. Because the geometry's height or thickness is much smaller compared to its other dimensions, the idea is to eliminate the dependency of the full 3D governing equations on said height dimension. For this purpose, known profiles for the velocity and temperature across the height direction are required. Keeping in mind the heat transfer problem under consideration, these profiles can be extracted by taking a cross section of a heat sink with no fins [13] and studying the resulting simplified 2D CHT problem as depicted in fig. A.1.

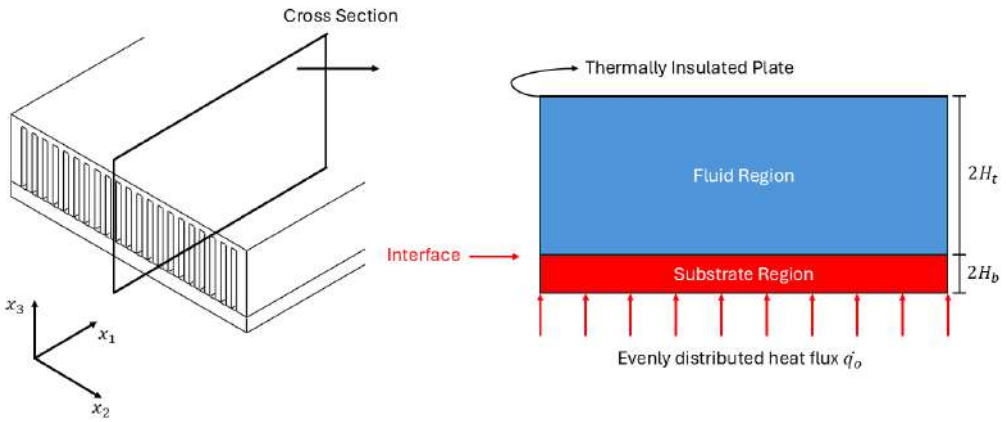

Figure A.1: *Cross Section of heat sink and simplified 2D CHT problem*

A.1 Velocity and Temperature Profiles

Fluid Region - Velocity Profile

The simplified 2D CHT problem depicted in fig. A.1 is examined, with x_1 denoted as the flow direction and x_3 as the extremely small height dimension. Assuming fully developed flow, the objective is to determine a non-dimensional velocity profile $f_u(x_3)$, as defined in equation:

$$f_u(x_3) = \frac{u_1'(x_3)}{u_1} \qquad x_3 \in [-H_t, +H_t] \tag{A.1}$$

that remains invariant in the flow direction, where u_1' is the x_1-component of the (dimensional) velocity, which for this simplified fully developed flow is only a function of x_3, and u_1 is the velocity at the middle ($x_3 = 0$) of the fluid region.

For a fully developed incompressible flow, the momentum equation in the flow direction can be simplified to:

$$-\frac{\partial p}{\partial x_1} + \mu \frac{\partial^2 u_1'}{\partial x_3^2} = 0 \tag{A.2}$$

By considering that the fluid's dynamic viscosity μ as well as the pressure gradient across the flow direction remain constant, equation A.2 gives:

$$\frac{\partial^2 u_1'(x_3)}{\partial x_3^2} = \frac{1}{\mu}\frac{\partial p}{\partial x_1} = t_1 \tag{A.3}$$

Integrating twice w.r.t. x_3 yields:

$$u_1'(x_3) = t_1 x_3^2 + C_1 x_3 + C_2 \tag{A.4}$$

Constants C_1 and C_2 are calculated by applying the following boundary conditions for the velocity u_1':

$$u_1'(x_3 = -H_t) = 0 \;\Rightarrow\; C_1 = 0$$

$$u_1'(x_3 = +H_t) = 0 \;\Rightarrow\; C_2 = -t_1 H_t^2$$

With C_1 and C_2 known, expression A.4 becomes:

$$u_1^{'}(x_3) = \frac{t_1}{H_t^2}\left(\frac{x_3^2}{H_t^2} - 1\right) \tag{A.5}$$

From the above expression, it becomes clear that the velocity u_1 at the middle of the fluid region is equal to $(-t_1/H_t^2)$ and, thus, the non-dimensional velocity profile $f_u(x_3)$ defined in equation A.1 is:

$$\boxed{f_u(x_3) = 1 - \frac{x_3^2}{H_t^2}} \qquad x_3 \in [-H_t, +H_t] \tag{A.6}$$

Fluid Region - Temperature Profile

Similar procedure is followed to derive a non-dimensional temperature profile $f_T(x_3)$, defined in equation:

$$f_T(x_3) = \frac{T_i(x_1) - T^{'}(x_1, x_3)}{T_i(x_1) - T(x_1)} \qquad x_3 \in [-H_t, +H_t] \tag{A.7}$$

that remains constant along the flow direction, where $T^{'}$ is the temperature field, T_i is the temperature at the fluid-solid interface ($x_3 = -H_t$) and T the fluid's bulk mean temperature across the height direction x_3.

Supposing that heat conduction in the flow direction can be neglected, the steady state energy equation for an incompressible fluid with constant properties can be written as:

$$\rho C_p\left(u_1^{'}\frac{\partial T^{'}}{\partial x_1}\right) - k_f\frac{\partial^2 T^{'}}{\partial x_3^2} = 0 \tag{A.8}$$

where ρ is the fluid's density, C_p the fluid's thermal capacity under constant pressure and k_f its thermal conductivity.

The heat flux $\dot{q}_i$ at the interface between solid and fluid is expressed using Fourier's law:

$$\dot{q}_i = -k_f\left.\frac{\partial T^{'}}{\partial x_3}\right|_{x_3=-H_t} \tag{A.9}$$

Computing the partial derivative of $T^{'}$ w.r.t. x_3 using equation A.7 which defines the non-dimensional profile $f_T(x_3)$ and substituting into the above

equation gives:

$$\frac{\partial T^{'}}{\partial x_3} = \frac{\partial}{\partial x_3}\left[T_i - f_T\left(T_i - T\right)\right] = -\left(T_i - T\right)\frac{\partial f_T}{\partial x_3} \tag{A.10}$$

$$\dot{q}_i = k_f\left(T_i - T\right)\frac{\partial f_T}{\partial x_3}\bigg|_{x_3=-H_t} \tag{A.11}$$

Assuming that heat flux $\dot{q}_i$ remains constant along the interface and considering that k_f and $\partial f_T/\partial x_3$ at $x_3 = -H_t$ are constant, equation A.11 suggests that $(T_i - T)$ must also be constant and thus:

$$\frac{\partial}{\partial x_1}\left(T_i - T\right) = 0 \;\Rightarrow\; \frac{\partial T_i}{\partial x_1} = \frac{\partial T}{\partial x_1} \tag{A.12}$$

Using relations A.10 and A.12, equation A.8 is rewritten as follows:

$$\rho C_p\left\{f_u u_1 \frac{\partial}{\partial x_1}\left[T_i - f_T\left(T_i - T\right)\right]\right\} + k_f\left(T_i - T\right)\frac{\partial^2 f_T}{\partial x_3^2} = 0$$

$$\Rightarrow\; \frac{\partial^2 f_T}{\partial x_3^2} = \frac{\rho C_p\, u_1\, \partial T/\partial x_1}{k_f\left(T - T_i\right)} f_u \tag{A.13}$$

For a laminar flow that is hydrodynamically and thermally fully developed, u_1 which is the velocity at the middle of the fluid region ($x_3 = 0$) and $\partial T/\partial x_1$ can both be considered constant. As a result, the multiplier of f_u in the above expression is also constant, hence:

$$\frac{\partial^2 f_T}{\partial x_3^2} = t_2\left(1 - \frac{x_3^2}{H_t^2}\right) \tag{A.14}$$

Integrating twice w.r.t x_3 gives the fourth order polynomial profile:

$$f_T = -\frac{t_2 x_3^4}{12 H_t^2} + \frac{t_2 x_3^2}{2} + C_3 x_3 + C_4 \tag{A.15}$$

Unknown constants C_3 and C_4 can be computed using the boundary conditions:

$$\left.\frac{\partial T^{'}}{\partial x_3}\right|_{x_3=+H_t} = 0 \;\Rightarrow\; \left.\frac{\partial f_T}{\partial x_3}\right|_{x_3=+H_t} = 0 \;\Rightarrow\; C_3 = -\frac{2}{3}t_2 H_t$$

$$T^{'}\left(x_3 = -H_t\right) = T_i \;\Rightarrow\; f_T\left(x_3 = -H_t\right) = 0 \;\Rightarrow\; C_4 = -\frac{13}{12}t_2 H_t^2$$

With C_3 and C_4 known, the non-dimensional profile f_T becomes:

$$f_T = -\frac{t_2 x_3^4}{12H_t^2} + \frac{t_2 x_3^2}{2} - \frac{2}{3}t_2 H_t x_3 - \frac{13}{12}t_2 H_t^2 \tag{A.16}$$

The value of t_2 is calculated by using the definition of the bulk mean temperature T of the fluid across x_3 given by equation:

$$T = \frac{\int_{-H_t}^{+H_t} u_1^{'} T^{'}\, dx_3}{\int_{-H_t}^{+H_t} u_1^{'}\, dx_3} = \frac{T_1}{T_2} \tag{A.17}$$

$$T_1 = \int_{-H_t}^{+H_t} u_1^{'} T^{'}\, dx_3 = \int_{-H_t}^{+H_t} f_u(x_3)\, u_1 \left[T_i - \left(T_i - T\right) f_T(x_3)\right]\, dx_3$$

$$= u_1 T_i \int_{-H_t}^{+H_t} f_u(x_3)\, dx_3 + u_1\left(T - T_i\right) \int_{-H_t}^{+H_t} f_u(x_3) f_T(x_3)\, dx_3$$

$$= u_1 T_i \frac{4}{3}H_t - u_1\left(T - T_i\right)\frac{t_2 H_t^3}{12}\frac{1664}{105} \tag{A.18}$$

$$T_2 = \int_{-H_t}^{+H_t} u_1^{'}\, dx_3 = u_1 \int_{-H_t}^{+H_t} f_u(x_3)\, dx_3 = u_1 \frac{4}{3}H_t \tag{A.19}$$

Going back to equation A.17, one may write that:

$$u_1 \frac{4}{3}H_t T = u_1 T_i \frac{4}{3}H_t - u_1\left(T - T_i\right)\frac{t_2 H_t^3}{12}\frac{1664}{105}$$

$$\Rightarrow \frac{4}{3} H_t \left(T - T_i\right) = -\left(T - T_i\right) \frac{t_2 H_t^3}{12} \frac{1664}{105} \Rightarrow t_2 = -\frac{105}{104 H_t^2}$$

Thus, the non-dimensional temperature profile f_T for the fluid region is extracted:

$$\boxed{f_T = \frac{35}{416}\left[\left(\frac{x_3}{H_t}\right)^4 - 6\left(\frac{x_3}{H_t}\right)^2 + 8\left(\frac{x_3}{H_t}\right) + 13\right]} \quad x_3 \in [-H_t, +H_t] \quad \text{(A.20)}$$

Substrate Region - Temperature Profile

Likewise for the substrate, a non-dimensional temperature profile $f_{T_b}(x_3)$, defined in equation:

$$f_{T_b}(x_3) = \frac{T_i(x_1) - T_b'(x_1, x_3)}{T_i(x_1) - T_b(x_1)} \qquad x_3 \in [-H_b, +H_b] \qquad \text{(A.21)}$$

that's invariant in x_1 direction is required, where T_b' is the substrate's temperature field, T_i is the temperature at the interface ($x_3 = +H_b$) and T_b the mean temperature of the substrate across x_3.

Assuming that heat conduction dominates in the x_3 direction, the steady state energy equation for a solid body with constant properties can be written as:

$$k_b \frac{\partial^2 T_b'}{\partial x_3^2} = 0 \qquad \text{(A.22)}$$

The heat flux $\dot{q}_o$ at the bottom surface of the substrate is assumed uniform and is expressed using Fourier's law:

$$\dot{q}_o = -k_b \left.\frac{\partial T_b'}{\partial x_3}\right|_{x_3 = -H_b} \qquad \text{(A.23)}$$

Computing the derivative of T_b' w.r.t. x_3 using equation A.21 which defines the non-dimensional profile $f_{T_b}(x_3)$ and substituting into the above equation gives:

$$\frac{\partial T_b^{'}}{\partial x_3} = \frac{\partial}{\partial x_3}\left[T_i - f_{T_b}\left(T_i - T_b\right)\right] = -\left(T_i - T_b\right)\frac{\partial f_{T_b}}{\partial x_3} \tag{A.24}$$

$$\dot{q_o} = k_b\left(T_i - T_b\right)\frac{\partial f_{T_b}}{\partial x_3}\bigg|_{x_3=-H_b} \tag{A.25}$$

Observing equation A.25, a similar conclusion to the one derived when studying the fluid region can be reached, that $(T_i - T_b)$ is constant and so:

$$\frac{\partial}{\partial x_1}\left(T_i - T_b\right) = 0 \;\Rightarrow\; \frac{\partial T_i}{\partial x_1} = \frac{\partial T_b}{\partial x_1} \tag{A.26}$$

Using relation A.24, equation A.22 is rewritten as follows:

$$\frac{\partial}{\partial x_3}\left[-k_b\left(T_i - T_b\right)\frac{\partial f_{T_b}}{\partial x_3}\right] = -k_b\left(T_i - T_b\right)\frac{\partial^2 f_{T_b}}{\partial x_3^2} = 0 \;\Rightarrow\; \frac{\partial^2 f_{T_b}}{\partial x_3^2} = 0 \tag{A.27}$$

Integrating twice w.r.t. x_3 results in the linear profile $f_{T_b} = C_5 x_3 + C_6$ where constants C_5, C_6 can be determined using the known boundary conditions as shown below:

$$\dot{q_o} = -k_b\frac{\partial T_b^{'}}{\partial x_3}\bigg|_{x_3=-H_b} = k_b\left(T_i - T_b\right)\frac{\partial f_{T_b}}{\partial x_3}\bigg|_{x_3=-H_b} \;\Rightarrow\; C_5 = \frac{\dot{q_o}}{k_b\left(T_i - T_b\right)}$$

$$T_b^{'}\left(x_3 = +H_b\right) = T_i \;\Rightarrow\; f_{T_b}\left(x_3 = +H_b\right) = 0 \;\Rightarrow\; C_6 = -\frac{\dot{q_o}H_b}{k_b\left(T_i - T_b\right)}$$

With C_5 and C_6 known, profile f_{T_b} becomes:

$$f_{T_b} = \frac{\dot{q_o}H_b}{k_b\left(T_i - T_b\right)}\left(\frac{x_3}{H_b} - 1\right) \;\Rightarrow\; f_{T_b} = t_3\left(\frac{x_3}{H_b} - 1\right) \tag{A.28}$$

To compute the value of t_3 the definition of T_b which is the mean temperature of the substrate across x_3 is employed as shown below:

$$T_b = \int_{-H_b}^{+H_b} \frac{T_b'}{2H_b}\, dx_3 = \frac{1}{2H_b} \int_{-H_b}^{+H_b} \left[T_i - f_{T_b}(x_3)\,(T_i - T_b)\right]\, dx_3$$

$$\Rightarrow T_b = \frac{1}{2H_b}\left[T_i \int_{-H_b}^{+H_b} dx_3 - (T_i - T_b) \int_{-H_b}^{+H_b} f_{T_b}(x_3)\, dx_3\right]$$

$$\Rightarrow T_b = \frac{1}{2H_b}\left[T_i\, 2H_b + (T_i - T_b)\, t_3\, 2H_b\right] \;\Rightarrow\; t_3 = -1$$

Thus the non-dimensional temperature profile f_{T_b} for the substrate is extracted:

$$\boxed{f_{T_b} = 1 - \frac{x_3}{H_b}} \qquad x_3 \in [-H_b, +H_b] \tag{A.29}$$

A.2 2.5D Equations

Fluid Region

For a steady laminar flow of an incompressible fluid the full 3D continuity and momentum equations are given by equations 2.1 and 2.2. The 3D velocity field can be expressed with the help of the non-dimensional velocity profile $f_u(x_3)$, as shown in equation 2.6, which remains invariant in directions x_1, x_2. Because the height of the fluid region is much smaller compared to its other dimensions, the momentum across the height direction, i.e. the momentum across the x_3 direction, can be ignored. After implementing the velocity profile $f_u(x_3)$, equations 2.1 and 2.2 can be written as follows:

$$f_u \frac{\partial u_j}{\partial x_j} = 0 \;\Rightarrow\; \frac{\partial u_j}{\partial x_j} = 0 \tag{A.30}$$

$$\rho f_u^2 u_j \frac{\partial u_i}{\partial x_j} = -\frac{\partial p}{\partial x_i} + \mu f_u \frac{\partial}{\partial x_j}\left(\frac{\partial u_i}{\partial x_j} + \frac{\partial u_j}{\partial x_i}\right) + \mu u_i \frac{\partial^2 f_u}{\partial x_3^2} \quad i = 1, 2 \tag{A.31}$$

The momentum in the x_3 direction was considered negligible and hence $\partial p/\partial x_3 = 0$. As a result, after the implementation of the velocity profile,

the pressure field p is now only a function of x_1, x_2. By integrating equations A.30 and A.31 w.r.t. x_3, using the velocity profile $f_u(x_3)$ as a weight function, the 2.5D continuity and momentum equations can be derived:

$$\int_{-H_t}^{+H_t} f_u(x_3)\frac{\partial u_j}{\partial x_j}\,dx_3 = 0 \;\Rightarrow\; \frac{\partial u_j}{\partial x_j}\int_{-H_t}^{+H_t} f_u(x_3)\,dx_3 = 0 \;\Rightarrow\; \frac{4}{3}H_t\frac{\partial u_j}{\partial x_j} = 0$$

$$\Rightarrow\; \frac{\partial u_j}{\partial x_j} = 0 \tag{A.32}$$

$$\int_{-H_t}^{+H_t} \rho f_u^3(x_3)u_j\frac{\partial u_i}{\partial x_j}\,dx_3 = -\int_{-H_t}^{+H_t} f_u(x_3)\frac{\partial p}{\partial x_i}\,dx_3$$

$$+\int_{-H_t}^{+H_t} \mu f_u^2(x_3)\frac{\partial}{\partial x_j}\left(\frac{\partial u_i}{\partial x_j}+\frac{\partial u_j}{\partial x_i}\right)\,dx_3 + \int_{-H_t}^{+H_t}\frac{2\mu}{H_t^2}f_u(x_3)u_i\,dx_3$$

$$\Rightarrow \rho u_j\frac{\partial u_i}{\partial x_j}\int_{-H_t}^{+H_t} f_u^3(x_3)\,dx_3 = -\frac{\partial p}{\partial x_i}\int_{-H_t}^{+H_t} f_u(x_3)\,dx_3$$

$$+\mu\frac{\partial}{\partial x_j}\left(\frac{\partial u_i}{\partial x_j}+\frac{\partial u_j}{\partial x_i}\right)\int_{-H_t}^{+H_t} f_u^2(x_3)\,dx_3 + \frac{2\mu}{H_t^2}u_i\int_{-H_t}^{+H_t} f_u(x_3)\,dx_3$$

$$\Rightarrow \frac{32}{35}H_t\rho u_j\frac{\partial u_i}{\partial x_j} = -\frac{4}{3}H_t\frac{\partial p}{\partial x_i} + \frac{16}{15}H_t\mu\frac{\partial}{\partial x_j}\left(\frac{\partial u_i}{\partial x_j}+\frac{\partial u_j}{\partial x_i}\right) + \frac{8}{3}\frac{\mu}{H_t}u_i$$

$$\Rightarrow\; \frac{6}{7}\rho u_j\frac{\partial u_i}{\partial x_j} + \frac{5}{4}\frac{\partial p}{\partial x_i} - \mu\frac{\partial}{\partial x_j}\left(\frac{\partial u_i}{\partial x_j}+\frac{\partial u_j}{\partial x_i}\right) - \frac{5}{2}\frac{\mu}{H_t^2}u_i = 0 \quad i = 1,2 \tag{A.33}$$

Equations A.32 and A.33 are the resulting 2.5D continuity and momentum equations, respectively. The source term $(-5\mu/2H_t^2)\,u_i$ that appears in the 2.5D momentum equation originates from the terms $\mu\left(\partial^2 u_i^{'}/\partial x_3^2\right)$ and contains a part of the information as to how the third dimension influences the flow. This term is absent in the 2D formulation of the problem, making the 2.5D model theoretically more accurate while maintaining 2D computational

cost. Similar procedure is followed to derive the 2.5D energy equation of the fluid region from the full 3D one which is given by equation 2.3. Keeping in mind that $(T_i - T)$ is a constant quantity and by ignoring once more the velocity component in the x_3 direction, equation 2.3, after implementing profiles $f_u(x_3)$ and $f_T(x_3)$, becomes:

$$\rho C_p f_u u_j \frac{\partial T}{\partial x_j} = \frac{\partial}{\partial x_j}\left(k_f \frac{\partial T}{\partial x_j}\right) - k_f (T_i - T) \frac{\partial^2 f_T}{\partial x_3^2} \tag{A.34}$$

Integrating equation A.34 w.r.t x_3 using the non-dimensional temperature profile $f_T(x_3)$ as a weight function results in:

$$\int_{-H_t}^{+H_t} \rho C_p f_u(x_3) f_T(x_3) u_j \frac{\partial T}{\partial x_j}\, dx_3 - \int_{-H_t}^{+H_t} f_T(x_3) \frac{\partial}{\partial x_j}\left(k_f \frac{\partial T}{\partial x_j}\right)\, dx_3$$

$$+ \int_{-H_t}^{+H_t} k_f (T_i - T) f_T(x_3) \frac{\partial^2 f_T(x_3)}{\partial x_3^2}\, dx_3 = 0$$

$$\Rightarrow \rho C_p u_j \frac{\partial T}{\partial x_j} \int_{-H_t}^{+H_t} f_u(x_3) f_T(x_3)\, dx_3 - \frac{\partial}{\partial x_j}\left(k_f \frac{\partial T}{\partial x_j}\right) \int_{-H_t}^{+H_t} f_T(x_3)\, dx_3$$

$$+ k_f (T_i - T) \int_{-H_t}^{+H_t} f_T(x_3) \frac{\partial^2 f_T(x_3)}{\partial x_3^2}\, dx_3 = 0$$

$$\Rightarrow \frac{4H_t}{3} \rho C_p u_j \frac{\partial T}{\partial x_j} - \frac{49 H_t}{26} \frac{\partial}{\partial x_j}\left(k_f \frac{\partial T}{\partial x_j}\right) - \frac{35}{26 H_t} k_f (T_i - T) = 0 \tag{A.35}$$

Equation A.35 is the resulting 2.5D energy equation for the fluid region.

Substrate Region

Likewise, considering that $(T_i - T_b)$ is a constant quantity, implementing the temperature profile $f_{T_b}(x_3)$ into the full 3D conduction equation 2.4 of the substrate region, yields:

$$\frac{\partial}{\partial x_j}\left(k_b \frac{\partial T_b}{\partial x_j}\right) - k_b\left(T_i - T_b\right)\frac{\partial^2 f_{T_b}}{\partial x_3^2} = 0 \tag{A.36}$$

Since the profile $f_{T_b}(x_3)$ of the substrate is linear, simply integrating equation A.36 w.r.t x_3 gives:

$$\int_{-H_b}^{+H_b} \frac{\partial}{\partial x_j}\left(k_b \frac{\partial T_b}{\partial x_j}\right)\, dx_3 - \int_{-H_b}^{+H_b} k_b\left(T_i - T_b\right)\frac{\partial^2 f_{T_b}}{\partial x_3^2}\, dx_3 = 0$$

$$\Rightarrow \frac{\partial}{\partial x_j}\left(k_b \frac{\partial T_b}{\partial x_j}\right)\int_{-H_b}^{+H_b} dx_3 - k_b\left(T_i - T_b\right)\int_{-H_b}^{+H_b} \frac{\partial^2 f_{T_b}}{\partial x_3^2}\, dx_3 = 0$$

$$\Rightarrow\ 2H_b \frac{\partial}{\partial x_j}\left(k_b \frac{\partial T_b}{\partial x_j}\right) - k_b\left(T_i - T_b\right)\frac{\partial f_{T_b}}{\partial x_3}\bigg|_{-H_b}^{+H_b} = 0$$

$$\Rightarrow\ 2H_b \frac{\partial}{\partial x_j}\left(k_b \frac{\partial T_b}{\partial x_j}\right) - \frac{k_b}{H_b}\left(T_b - T_i\right) + \dot{q}_o = 0 \tag{A.37}$$

Equation A.37 is the 2.5D energy equation for the substrate region. Finally, it is interesting to mention that the heat fluxes entering and exiting from each region appear as source terms in the energy equations A.35 and A.37.

Bibliography

[1] K.C. Giannakoglou. *Optimization Methods in Aerodynamics*. PcOpt/NTUA, 2006.

[2] M.P. Bendsoe and O. Sigmund. *Topology Optimization: Theory, Methods and Applications*. Springer, 2003.

[3] Jorge Nocedal and Stephen J. Wright. *Numerical Optimization*. Springer, 2006.

[4] S. Kirkpatrick, C.D. Gelatt, and M.P. Vecchi. Optimization by Simulated Annealing. Science, 220(4598), 671–680 (1983).

[5] D.E. Goldberg. *Genetic Algorithms in Search, Optimization, and Machine Learning*. Addison-Wesley, 1989.

[6] M. Bendsoe and N. Kikuchi. Generating optimal topologies in structural design using a homogenization method. Journal of Computer Methods in Applied Mechanics and Engineering, 71:197–224, 1988.

[7] B. Chen and N. Kikuchi. Topology optimization with design-dependent loads. Computer Methods in Applied Mechanics and Engineering, 37:57–70 (2001).

[8] S. Amstutz and H. Andra. A new algorithm for topology optimization using a level-set method. Journal of Computational Physics, 216:573–588, (2006).

[9] J.A. Sethian and A. Wiegmann. Structural boundary design via level set and immersed interface methods. Journal of Computational Physics, 163:489–528 (2000).

[10] A. Gersborg-Hansen, M. P. Bendsoe, and O. Sigmund. Topology optimization of heat conduction problems using the finite volume method. Structural and Multidisciplinary Optimization, Springer 31, 251–259 (2006).

[11] C. Zhuang, Z. Xiong, and H. Ding. A level set method for topology optimization of heat conduction problem under multiple load cases. Com-

puter Methods in Applied Mechanics and Engineering, 196:1074–1084 (2007).

[12] T. Borrvall and J. Petersson. Topology Optimization of Fluids in Stokes Flow. International Journal for Numerical Methods in Fluids, 41, 77–107 (2003).

[13] S. Yan, F. Wang, J. Hong, and O. Sigmund. Topology optimization of microchannel heat sinks using a two-layer model. International Journal of Heat and Mass Transfer, 143 (2019) 118462.

[14] G.H. Yoon. Topological design of heat dissipating structure with forced convective heat transfer. Journal of Mechanical Science and Technology, Springer 24, 1225–1233 (2010).

[15] E.M. Papoutsis-Kiachagias and K.C. Giannakoglou. Continuous adjoint methods for turbulent flows, applied to shape and topology optimization: Industrial applications. Archives of Computational Methods in Engineering, 23(2):255–299 (2016).

[16] Evangelos M. Papoutsis–Kiachagias. *Adjoint Methods for Turbulent Flows, Applied to Shape or Topology Optimization and Robust Design.* PhD thesis, National Technical University of Athens, 2013.

[17] J. Deaton and R. Grandhi. A survey of structural and multidisciplinary continuum topology optimization: post 2000. Structural and Multidisciplinary Optimization, Springer 49, 1–38 (2013).

[18] O. Sigmund and K. Maute. Topology optimization approaches. Structural and Multidisciplinary Optimization, Springer 48, 1031–1055 (2013).

[19] K.C. Giannakoglou, E.M. Papoutsis-Kiachagias, and N. Galanos. *adjointOptimisationFoam, an OpenFOAM-based optimisation tool.* OpenFOAM User Manual, November 2024.

[20] B.S. Lazarov and O. Sigmund. Filters in topology optimization based on Helmholtz-type differential equations. International Journal for Numerical Methods in Engineering, 86:765–781.

[21] W.K. Anderson and D.L. Bonhaus. Aerodynamic design on unstructured grids for turbulent flows. NASA Technical Memorandum, 112867 (1997).

[22] W.K. Anderson and D.L. Bonhaus. Airfoil Design on Unstructured Grids for Turbulent Flows. AIAA Journal, 37(2):185-191 (1999).

[23] A. Jameson. Optimum Aerodynamic Design Using CFD And Control Theory. AIAA Paper, 1729 (1995).

[24] W.K. Anderson and V. Venkatakrishnan. Aerodynamic design optimization on unstructured grids with a continuous adjoint formulation. AIAA Paper, 0643 (1997).

[25] Graeme J. Kennedy and Jason E. Hicken. Improved constraint-aggregation methods. Computer Methods in Applied Mechanics and Engineering, 289:332–354 (2015).

Εθνικό Μετσόβιο Πολυτεχνείο
Σχολή Μηχανολόγων Μηχανικών
Τομέας Ρευστών
Μονάδα Παράλληλης Υπολογιστικής Ρευστοδυναμικής
& Βελτιστοποίησης

Εφαρμογές Βελτιστοποίησης Τοπολογίας στο Σχεδιασμό Ψυκτρών με Μικροκανάλια

Διπλωματική Εργασία - Εκτενής Περίληψη στα Ελληνικά

Δημήτριος Νικολαΐδης

Επιβλέπων: Κυριάκος Χ. Γιαννάκογλου, Καθηγητής ΕΜΠ

Αθήνα, 2025

Εισαγωγή

Η έννοια της βελτιστοποίησης τοπολογίας (TopO) εμφανίστηκε για πρώτη φορά στο χώρο της δομικής μηχανικής [6], όπου ένα συνεχές πραγματικό πεδίο πυκνότητας χρησιμοποιήθηκε με σκοπό να βρεθεί η βέλτιστη κατανομή στερέου υλικού σε κατασκευές. Η ιδέα ήταν να αναγνωριστεί η βέλτιστη τοπολογία του χώρου σχεδιασμού, δηλαδή η πιο κατάλληλη κατανομή του πεδίου πυκνότητας, με στόχο η μορφή της κατασκευής που θα προκύψει να της προσδίδει την καλύτερη συμπεριφορά όταν της ασκούνται προδιαγεγραμμένα μηχανικά φορτία. Περιοχές του χώρου σχεδιασμού με μοναδιαία τιμή πυκνότητας αντιστοιχούσαν σε περιοχές στερεού υλικού, ενώ μηδενικές τιμές πυκνότητας υποδείκνυαν τις κενές περιοχές (απουσία στερεού υλικού). Η ιδέα της TopO προεκτάθηκε και στο χώρο της υπολογιστικής ρευστοδυναμικής (CFD), αρχικά για ροές Stokes [12], όπου οι εξισώσεις διατήρησης ορμής επαυξήθηκαν με τους λεγόμενους όρους Brinkman ή όρους ποινής ταχύτητας οι οποίοι αποτελούσαν συνάρτηση ενός συνεχούς πραγματικού πεδίου πορώδους (μη-διαπερατότητας).

Αντικείμενο της παρούσας διπλωματικής εργασίας είναι η εφαρμογή TopO στο σχεδιασμό ψυκτρών (εξαναγκασμένης συναγωγής) με μικροκανάλια, για ψύξη ηλεκτρικών κυκλωμάτων. Εκτός απο τους όρους ποινής ταχύτητας που περιέχονται στις εξισώσεις διατήρησης ορμής, η θερμική αγωγιμότητα μοντελοποιείται και αυτή ως συνάρτηση της μη-διαπερατότητας [13], [14] ώστε να ληφθεί υπόψη η διαφορά στις θερμικές ιδιότητες μεταξύ ρευστού και στερεού υλικού. Το πρωτεύον πρόβλημα αποτελεί ένα πρόβλημα συζυγούς μεταφοράς θερμότητας (CHT) μεταξύ στερεού χωρίου (υπόστρωμα ψύκτρας) και ρευστού χωρίου το οποίο είναι και ο χώρος σχεδιασμού της βελτιστοποίησης. Στόχος είναι η εύρεση της βέλτιστης κατανομής στερεού υλικού στο χωρίο του ρευστού (και άρα η εύρεση της βέλτιστης διαδρομής που πρέπει να ακολουθήσει το ψυκτικό μέσο) ώστε να επιτευχθεί μέγιστη απαγωγή θερμότητας μέσω αγωγής και συναγωγής.

Εξαιτίας της φύσης των γεωμετριών που συναντώνται κατά τη μελέτη ροών σε μικροκανάλια, γίνεται χρήση του 2.5Δ CHT μοντέλου που προτάθηκε στο [13], το οποίο εκφυλίζει τις 3Δ εξισώσεις σε 2.5Δ. Δεδομένου ότι σε μια διαδικασία βελτιστοποίησης το πρωτεύον πρόβλημα επιλύεται επαναληπτικά, η δυνατότητα αποφυγής επίλυσης του πλήρους 3Δ προβλήματος μειώνει σημαντικά το υπολογιστικό κόστος κάθε κύκλου βελτιστοποίησης. Οι παράγωγοι ευαισθησίας της συνάρτησης στόχου που απαιτούνται από την SQP (Sequential Quadratic Programming), η οποία είναι η αιτιοκρατική μέθοδος ανανέωσης των μεταβλητών σχεδιασμού, υπολογίζονται μέσω της συνεχούς συζυγούς μεθόδου.

Το Πρωτεύον Πρόβλημα

Σε πολλές εφαρμογές CFD, συναντώνται γεωμετρίες των οποίων το πάχος ή το ύψος είναι πολύ μικρότερο σε σχέση με τις υπόλοιπες διαστάσεις τους. Σε τέτοιες περιπτώσεις, δεδομένου ότι η ορμή του ρευστού κατά τη διάσταση του

ύψους είναι σχεδόν αμελητέα, μια λογική πρακτική θα ήταν να αγνοηθεί εντελώς η διάσταση αυτή και να λυθεί ένα κλασσικό 2Δ πρόβλημα. Παρόλα αυτά, μια άλλη εναλλακτική ώστε να απλοποιηθεί το πλήρες 3Δ πρόβλημα είναι να θεωρηθεί ότι η συμπεριφορά της ροής κατά τη διάσταση του ύψους είναι προβλέψιμη. Με άλλα λόγια, θεωρώντας πλήρως ανεπτυγμένη ροή και κάνοντας κάποιες επιπλέον παραδοχές είναι δυνατόν να εξαχθούν σταθερά προφίλ ταχύτητας και θερμοκρασίας κατά τη διάσταση του ύψους.

Η εισαγωγή των προφίλ αυτών στις 3Δ εξισώσεις που διέπουν το CHT πρόβλημα και στη συνέχεια ολοκλήρωση τους κατά τη διάσταση του ύψους οδηγούν στη δημιουργία μέσων ή 2.5Δ εξισώσεων [12], [13]. Μέσω αυτής της διαδικασίας εμφανίζονται όροι πηγής και δεδομένες σταθερές μπροστά από τους υπάρχοντες όρους των τελικών εξισώσεων. Αυτοί οι όροι πηγής και οι σταθερές εκφράζουν ένα κομμάτι της πληροφορίας ως προς το πως η διάσταση του ύψους που έχει αγνοηθεί, επηρεάζει τη ροή και τα φαινόμενα μεταφοράς θερμότητας. Ο όρος 2.5Δ προκύπτει από το γεγονός ότι, παρόλο που αυτές οι εξισώσεις δεν παρέχουν την ίδια ακρίβεια με μια πλήρης 3Δ επίλυση, αντικατοπτρίζουν καλύτερα τη φυσική του προβλήματος σε σχέση με ένα 2Δ μοντέλο, όπου όλη η πληροφορία σχετικά με την επίδραση της τρίτης διάστασης αγνοείται. Για τη μελέτη ροών σε μικροκανάλια, όπου συναντώνται γεωμετρίες με μικρές υδραυλικές διαμέτρους και υψηλούς λόγους επιφάνειας προς όγκο, η χρήση ενός 2.5Δ μοντέλου είναι μια δικαιολογημένη επιλογή.

Τα προβλήματα που αναλύονται σε αυτή τη διπλωματική εργασία αφορούν ασυμπίεστες και στρωτές ροές, όπου τόσο τα ροϊκά φαινόμενα όσο και τα φαινόμενα μεταφοράς θερμότητας θεωρούνται χρονικά μόνιμα. Επιπλέον, οι ιδιότητες του ρευστού και του στερεού υλικού θεωρούνται σταθερές. Το 2.5Δ CHT μοντέλο που παρουσιάζεται στο [13] αφορά ψύκτρες με μικροκανάλια που έχουν τη γεωμετρική μορφή του σχήματος Α΄.2, όπου το ύψος του ρευστού χωρίου και του υποστρώματος (στερέου χωρίου) είναι σχετικά μικρά σε σχέση με τις υπόλοιπες διαστάσεις και έτσι 2.5Δ εξισώσεις μπορούν να εξαχθούν για το κάθε χωρίο. Η κάτω επιφάνεια του υποστρώματος θεωρείται ομοιόμορφα θερμαινόμενη.

Οι 3Δ εξισώσεις συνέχειας, διατήρησης ορμής και διατήρησης ενέργειας για το χωρίο του ρευστού είναι:

$$R^p = \frac{\partial u_j^{'}}{\partial x_j} = 0 \tag{Α΄.38}$$

$$R_i^{u'} = \rho u_j^{'} \frac{\partial u_i^{'}}{\partial x_j} + \frac{\partial p}{\partial x_i} - \mu \frac{\partial}{\partial x_j}\left(\frac{\partial u_i^{'}}{\partial x_j} + \frac{\partial u_j^{'}}{\partial x_i}\right) = 0 \quad i = 1,2,3 \tag{Α΄.39}$$

$$R^{T'} = \rho C_p u_j^{'} \frac{\partial T'}{\partial x_j} - \frac{\partial}{\partial x_j}\left(k_f \frac{\partial T'}{\partial x_j}\right) = 0 \tag{Α΄.40}$$

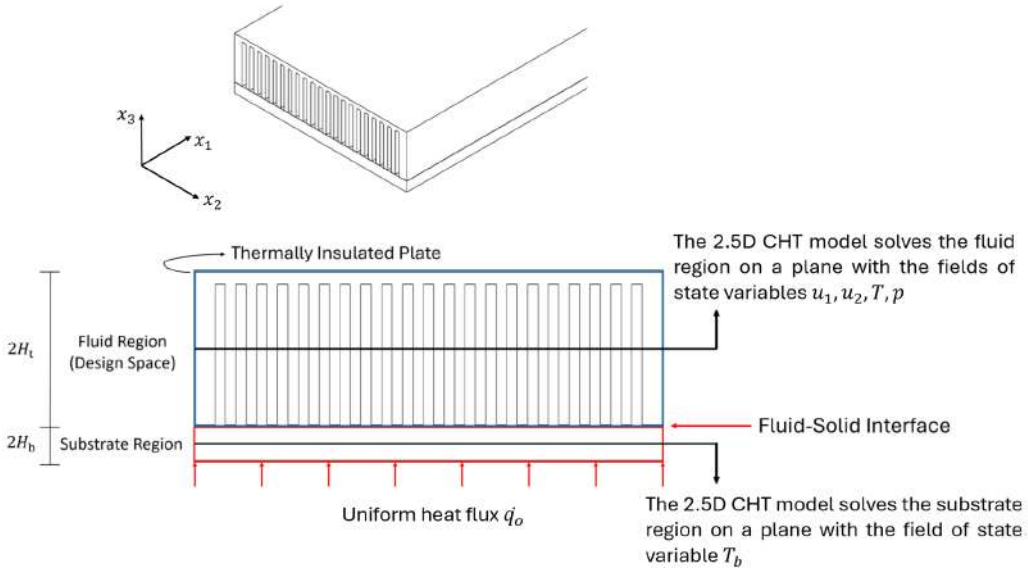

Σχήμα Α′.2: *Γεωμετρική μορφή των υπό μελέτη ψυκτρών με μικροκανάλια, αποτελούμενες από ένα επίπεδο κάτω υπόστρωμα και μια αδιαβατική επίπεδη πάνω πλάκα. Κατά την εξέλιξη του αλγορίθμου βελτιστοποίησης, περιοχές του ρευστού χωρίου αρχίζουν να στερεοποιούνται, δηλαδή πτερύγια διαμορφώνονται στο χωρίο του ρευστού που είναι και ο χώρος σχεδιασμού της βελτιστοποίησης.*

όπου ρ, μ, C_p και k_f είναι η πυκνότητα, δυναμική συνεκτικότητα, θερμοχωρητικότητα υπό σταθερή πίεση και θερμική αγωγιμότητα του ρευστού. Το 3Δ πεδίο πίεσης συμβολίζεται με $p\left(x_1, x_2, x_3\right)$, ενώ $u_i^{'}\left(x_1, x_2, x_3\right)$ με $i = 1, 2, 3$ είναι οι συνιστώσες του 3Δ πεδίου ταχύτητας και $T^{'}\left(x_1, x_2, x_3\right)$ το πλήρες 3Δ πεδίο θερμοκρασίας του ρευστού. Η 3Δ εξίσωση μεταφοράς θερμότητας για το υπόστρωμα (στερεό χωρίο) μπορεί να γραφεί ως:

$$R^{T_b^{'}} = \frac{\partial}{\partial x_j}\left(k_b \frac{\partial T_b^{'}}{\partial x_j}\right) = 0 \tag{Α′.41}$$

όπου k_b είναι η θερμική αγωγιμότητα του υποστρώματος και $T_b^{'}\left(x_1, x_2, x_3\right)$ το πλήρες 3Δ θερμοκρασιακό πεδίο του. Ακολουθώντας την αναλυτική διαδικασία που περιγράφεται στο Παράρτημα Α, τα αδιάστατα και αμετάβλητα κατα τις κατευθύνσεις x_1, x_2 προφίλ ταχύτητας και θερμοκρασίας που εξάγονται για το χωρίο του ρευστού και του στερεού υποστρώματος είναι τα ακόλουθα:

$$f_u\left(x_3\right) = 1 - \frac{x_3^2}{H_t^2} \tag{Α′.42}$$

$$f_T(x_3) = \frac{T_i - T'}{T_i - T} = \frac{35}{416}\left[\left(\frac{x_3}{H_t}\right)^4 - 6\left(\frac{x_3}{H_t}\right)^2 + 8\left(\frac{x_3}{H_t}\right) + 13\right] \quad \text{(A′.43)}$$

$$f_{T_b}(x_3) = \frac{T_i - T_b'}{T_i - T_b} = 1 - \frac{x_3}{H_b} \quad \text{(A′.44)}$$

όπου $\boldsymbol{u} = [u_1\ u_2]^T$ είναι η ταχύτητα στο μέσο επίπεδο του ρευστού χωρίου, $T_i(x_1, x_2)$ είναι η θερμοκρασία στη διεπιφάνεια μεταξύ ρευστού χωρίου και υποστρώματος, ενώ με $T(x_1, x_2) = \int_{-H_t}^{+H_t} |\boldsymbol{u}'|T'\ dx_3 / \int_{-H_t}^{+H_t} |\boldsymbol{u}'|\ dx_3$ συμβολίζεται η σταθμισμένη με βάση τη ταχύτητα μέση θερμοκρασία του ρευστού κατά x_3 και $T_b(x_1, x_2) = \int_{-H_b}^{+H_b} T_b'\ dx_3/2H_b$ η μέση θερμοκρασία του στερεού υποστρώματος κατά x_3. Επιπλέον, H_t και H_b είναι τα μισά ύψη του ρευστού και στερεού χωρίου αντίστοιχα. Με βάση τα προφίλ αυτά, οι 2.5Δ εξισώσεις που προκύπτουν (αναλυτική διατύπωση στο Παράρτημα Α) τροποποιούνται κατάλληλα ώστε να επιτρέψουν την πραγματοποίηση μιας διαδικασίας TopO, οδηγώντας τελικά στις πρωτεύουσες εξισώσεις του προβλήματος βελτιστοποίησης:

$$R^p = \frac{\partial u_j}{\partial x_j} = 0 \quad \text{(A′.45)}$$

$$R_i^u = \frac{6}{7}\rho u_j \frac{\partial u_i}{\partial x_j} + \frac{5}{4}\frac{\partial p}{\partial x_i} - \mu\frac{\partial}{\partial x_j}\left(\frac{\partial u_i}{\partial x_j} + \frac{\partial u_j}{\partial x_i}\right) - G(a)\, u_i = 0 \quad i = 1, 2 \quad \text{(A′.46)}$$

$$R^T = \frac{4H_t}{3}\rho C_p u_j \frac{\partial T}{\partial x_j} - \frac{49H_t}{26}\frac{\partial}{\partial x_j}\left[k_{eff}(a)\frac{\partial T}{\partial x_j}\right] - h(a)(T_b - T) = 0 \quad \text{(A′.47)}$$

$$R^{T_b} = 2H_b\frac{\partial}{\partial x_j}\left(k_b\frac{\partial T_b}{\partial x_j}\right) - h(a)(T_b - T) + \dot{q}_o = 0 \quad \text{(A′.48)}$$

με $h(a) = 35k_b k_{eff}(a) / [26H_t k_b + 35H_b k_{eff}(a)]$ και $a \in [0, 1]$ το πεδίο του πορώδους. Μηδενικές (ή σχεδόν μηδενικές) τιμές πορώδους αντιστοιχούν σε περιοχές του χώρου σχεδιασμού που καταλαμβάνονται από ρευστό και μοναδιαίες (ή σχεδόν μοναδιαίες) τιμές πορώδους δηλώνουν παρουσία στερεού υλικού. Στόχος του αλγορίθμου είναι η εύρεση του βέλτιστου πεδίου a, με σκοπό η γεωμετρία της ψύκτρας (η διαμόρφωση των πτερυγίων) που θα προκύψει να έχει βέλτιστη θερμική απόδοση. Πρέπει να σημειωθεί ότι το πεδίο πίεσης p για το οποίο λύνει το 2.5Δ μοντέλο είναι πλέον συνάρτηση μόνο του x_1 και x_2. Οι όροι ποινής ταχύτητας $G(a)\, u_i$ μοντελοποιούνται κατάλληλα, λαμβάνοντας

υπόψη τον ήδη υπάρχοντα όρο πηγής $\left(-5\mu/2H_t^2\right)u_i$ που υπάρχει στη 2.5Δ εξίσωση ορμής και εκφράζει τις μέσες τάσεις $\mu\left(\partial^2 u_i^{'}/\partial x_3^2\right)$ κατά x_3. Ταυτόχρονα γίνεται χρήση της φαινόμενης θερμικής αγωγιμότητας $k_{eff}\left(a\right)$, αντί για απλά της θερμικής αγωγιμότητας k_f του ρευστού ώστε να ληφθούν υπόψη τα στερεά πτερύγια στο χωρίου του ρευστού. Συγκεκριμένα [19]:

$$G\left(a\right)u_i = \left[\frac{5\mu}{2H_t^2} + I\left(a\right)\left(\frac{5\mu M^2}{2H_t^2} - \frac{5\mu}{2H_t^2}\right)\right]u_i \tag{A′.49}$$

$$k_{eff}\left(a\right) = k_f + I\left(a\right)\left(k_b - k_f\right) \tag{A′.50}$$

Όπου M είναι μια σταθερή αδιάστατη βαθμωτή ποσότητα που χρησιμοποιείται ώστε οι όροι Brinkman να κυριαρχούν έναντι των υπολοίπων όρων στην πρωτεύουσα εξίσωση διατήρησης της ορμής στις στερεοποιημένες περιοχές του χώρου σχεδιασμού. Έτσι στις περιοχές αυτές παράγεται ένα τοπικά μηδενικό πεδίο ταχύτητας. Ως συνάρτηση παρεμβολής $I\left(a\right)$ που χρησιμοποιείται ώστε να υπολογίζονται οι οροι $G\left(a\right)u_i$ και $k_{eff}\left(a\right)$ για ενδιάμεσες τιμές του πεδίου του πορώδους, επιλέγεται η συνάρτηση Borrvall-Petersson [12]:

$$I\left(a\right) = \frac{a}{1 + b(1-a)} \tag{A′.51}$$

με υψηλότερες τιμές της παραμέτρου b να οδηγούν στη μείωση των γκρι ζωνών. Η δημιουργία γκρι ζωνών είναι από τα γνωστά αρνητικά ζητήματα που εμφανίζονται σε προβλήματα TopO βασισμένα στην έννοια του πορώδους και αποτελούν περιοχές μερικής παρουσίας υλικού, με ενδιάμεσες ιδιότητες μεταξύ ρευστού και στερεού υλικού. Σε προβλήματα TopO, η απευθείας χρήση του πεδίου του πορώδους a για τον υπολογισμό των όρων που εξαρτώνται από αυτό, οδηγεί σε γεωμετρίες μορφής σκακιέρας με την τελική βέλτιστη λύση να εξαρτάται από τη πυκνότητα του πλέγματος και από τα σχήματα διακριτοποίησης που χρησιμοποιήθηκαν για την επίλυση των πρωτευουσών και συζυγών εξισώσεων. Για την αποφυγή αυτών των προβλημάτων πραγματοποιείται φιλτράρισμα [20] του πεδίου του πορώδους, επιλύοντας την εξίσωση:

$$-\left(\frac{R}{2\sqrt{3}}\right)^2 \frac{\partial}{\partial x_j}\left(\frac{\partial \tilde{a}}{\partial x_j}\right) + \tilde{a} = a, \qquad R = m_R\left(\bar{V}\right)^{1/2} \tag{A′.52}$$

$$\tilde{a} = 1 \tag{A′.53}$$

με σκοπό τον υπολογισμό ενός φιλτραρισμένου πεδίου πορώδους $\tilde{a}$. Η ακτίνα φιλτραρίσματος R υπολογίζεται [19] ως ένα πολλαπλάσιο του μέσου όγκου κελιού $\bar{V}$. Παρόλο που η τεχνική φιλτραρίσματος ομαλοποιεί το πεδίο του πο-

ρώδους, ενισχύει το πρόβλημα των γκρι ζωνών καθιστώντας δύσκολο να προσδιορίσει κανείς αν υπάρχει ρευστό ή στερεό στις περιοχές αυτές του χώρου σχεδιασμού. Για το λόγο αυτό, πραγματοποιείται προβολή [20] του φιλτραρισμένου πεδίου $\tilde{a}$ με βάση τη συνάρτηση:

$$\beta = \frac{\tanh(0.5\lambda) + \tanh[\lambda(\tilde{a} - 0.5)]}{2\tanh(0.5\lambda)} \tag{A′.54}$$

με αυξημένες τιμές της παραμέτρου λ να ενισχύουν τη δυαδικότητα του πεδίου β. Έπειτα από το φιλτράρισμα και τη προβολή του πεδίου του πορώδους, το πεδίο β είναι αυτό που χρησιμοποιείται τελικά στις εξισώσεις A′.49, A′.50 και A′.51 για τον υπολογισμό των όρων Brinkman, της φαινόμενης θερμικής αγωγιμότητας και φυσικά του $h = h(k_{eff})$ και όχι απευθείας το πεδίο του πορώδους.

Λαμβάνοντας υπόψη ότι όλες οι ροές που μελετώνται στη παρούσα διπλωματική είναι ροές που οδηγούνται από προδιαγεγραμμένη κλίση πίεσης, οι οριακές συνθήκες για τις πρωτεύουσες μεταβλητές δίνονται παρακάτω:

Όρια Εισόδου S_I

$$\frac{\partial u_i}{\partial x_j} n_j = 0, \quad p = p_I = const, \quad T = T_I = const, \quad \frac{\partial T_b}{\partial x_j} n_j = 0 \tag{A′.55}$$

Όρια Εξόδου S_O

$$\frac{\partial u_i}{\partial x_j} n_j = 0, \quad p = 0 = const, \quad \frac{\partial T}{\partial x_j} n_j = 0, \quad \frac{\partial T_b}{\partial x_j} n_j = 0 \tag{A′.56}$$

Στερεά Όρια S_W

$$u_i = 0, \quad \frac{\partial p}{\partial x_j} n_j = 0, \quad \frac{\partial T}{\partial x_j} n_j = 0, \quad \frac{\partial T_b}{\partial x_j} n_j = 0 \tag{A′.57}$$

Το 2.5Δ μοντέλο λύνει το χωρίο του ρευστού και το χωρίο του στερεού υποστρώματος πάνω στο ίδιο ομοιόμορφο καρτεσιανό 2Δ πλέγμα και αντιλαμβάνεται τα στερεά πτερύγια ως περιοχές στο πλέγμα με μοναδιαία τιμή πορώδους. Με άλλα λόγια, το 2.5Δ μοντέλο δεν θεωρεί τις περιμετρικές επιφάνειες των πτερυγίων σαν αυστηρά στερεά όρια. Τα στερεά όρια S_W που αναφέρονται εδώ αφορούν όλα τα υπόλοιπα όρια πέρα της εισόδου και εξόδου που οριοθετούν το 2Δ υπολογιστικό χωρίο Ω πάνω στο οποίο το 2.5Δ μοντέλο επιλύει τις πρωτεύουσες εξισώσεις.

Καθώς ο σκοπός του αλγορίθμου βελτιστοποίησης είναι να προκύψει μια γεωμετρία ψύκτρας με βέλτιστη θερμική συμπεριφορά, η (κανονικοποιημένη) μέγιστη

θερμοκρασία που εμφανίζεται στο υπόστρωμα (στερεό χωρίο) της ψύκτρας, που έρχεται σε άμεση επαφή με τα ηλεκτρονικά στοιχεία, επιλέγεται ως η συνάρτηση στόχος προς ελαχιστοποίηση και δίνεται από την εξίσωση:

$$F = \left[\int_{\Omega} \left(\frac{T_b}{T_{ref}} \right)^p \, d\Omega \right]^{\frac{1}{p}} \tag{Α΄.58}$$

όπου $p \geq 1$ και T_{ref} μια σταθερή θερμοκρασία αναφοράς που χρησιμοποιείται για τη κανονικοποίηση (συνήθως επιλέγεται η θερμοκρασία εισόδου του ρευστού T_I).

Σύγκριση 2.5Δ και 3Δ - Αξιολόγηση 2.5Δ Μοντέλου

Ένας απλός και προσεγγιστικός τρόπος αξιολόγησης της ακρίβειας του 2.5Δ μοντέλου, είναι να επιλυθεί το CHT πρόβλημα, σε διαφορετικές κλίσεις πίεσης, για ψύκτρα με τυχαίες διαμορφώσεις πτερυγίων και τα αποτελέσματα να συγκριθούν με αυτά που προκύπτουν από πλήρεις 3Δ προσομοιώσεις. Για τις 3Δ προσομοιώσεις, γεννώνται διαφορετικά 3Δ σωματόδετα και μη-δομημένα πλέγματα για το χωρίο του ρευστού και το χωρίο του στερεού, με το τελευταίο να περιλαμβάνει και το υπόστρωμα και τα στερεά πτερύγια. Σε αντίθεση, για τις 2.5Δ επιλύσεις, γεννάται ένα μοναδικό, ομοιόμορφο, δομημένο και καρτεσιανό 2Δ πλέγμα πάνω στο οποίο το 2.5Δ μοντέλο επιλύει και το χωρίο του ρευστού και του στερεού, με τη διαφορά όμως ότι τα στερεά πτερύγια θεωρούνται τώρα μέρος του ρευστού χωρίου. Καθώς η θέση στο χώρο και η γεωμετρική μορφή των πτερυγίων είναι γνωστές εξ' αρχής, στα κελιά που αντιστοιχούν στα πτερύγια δίνεται σταθερή μοναδιαία τιμή μη-διαπερατότητας και σε όλα τα υπόλοιπα κελιά η τιμή του πορώδους είναι μηδενική. Είναι σημαντικό η συνολική πύκνωση του πλέγματος να είναι επαρκής ώστε να προσεγγιστεί με ακρίβεια η γεωμετρία των στερεών πτερυγίων και επίσης να μην πραγματοποιηθεί φιλτράρισμα και προβολή του πεδίου του πορώδους. Τέλος αναφέρεται ότι ολόκληρη η κάτω επιφάνεια του υποστρώματος θερμαίνεται ομοιόμορφα.

Στα σχήματα Α΄.5, Α΄.6, Α΄.7 φαίνεται οπτική ομοιότητα στα πεδία ταχύτητας και θερμοκρασίας στο μέσο επίπεδο του ρευστού και στερεού χωρίου, που προέκυψαν από τις 2.5Δ και 3Δ προσομοιώσεις για τη περίπτωση της διάταξης που φαίνεται στο σχήμα Α΄.3α΄. Παρατηρώντας και τους πίνακες Α΄.1, Α΄.2 και Α΄.3, μπορούν να παρατηρηθούν τα εξής:

1. Ανεξαρτήτως γεωμετρίας, το 2.5Δ μοντέλο υπολογίζει με μεγαλύτερη ακρίβεια τα θερμοκρασιακά πεδία για μικρές κλίσεις πίεσης κατά μήκος της ψύκτρας, κυρίως διότι η υπόθεση της πλήρως ανεπτυγμένης ροής δεν ισχύει όσο η πτώση πίεσης αυξάνεται. Ειδικά το θερμοκρασιακό προφίλ f_T δεν ισχύει για μια ροή που δεν είναι αναπτυγμένη και συμφώνα με το [13] αυτός είναι και ο λόγος που, μερικές φόρες, κατά την ανάκτηση του πεδίου θερμοκρασίας του ρευστού σε ένα $x_3 = const$ επίπεδο από

το πρωτεύον T πεδίο, παρατηρούνται σε τοπικές περιοχές, θερμοκρασίες μικρότερες από τη θερμοκρασία εισόδου του ρευστού που είναι αφύσικο.

2. Το 2.5Δ μοντέλο συμφωνεί με τα 3Δ αποτελέσματα ως προς τα ποια διάταξη πτερυγίων είναι η πιο αποτελεσματική θερμικά σε δεδομένο σημείο λειτουργίας (δεδομένη κλίση πίεσης) της ψύκτρας. Αυτό το γεγονός το καθιστά ικανό να χρησιμοποιηθεί σαν επιλύτης του πρωτεύοντος προβλήματος μιας διαδικασίας TopO και να οδηγήσει τον αλγόριθμο σε μια γεωμετρία με την καλύτερη θερμική συμπεριφορά.

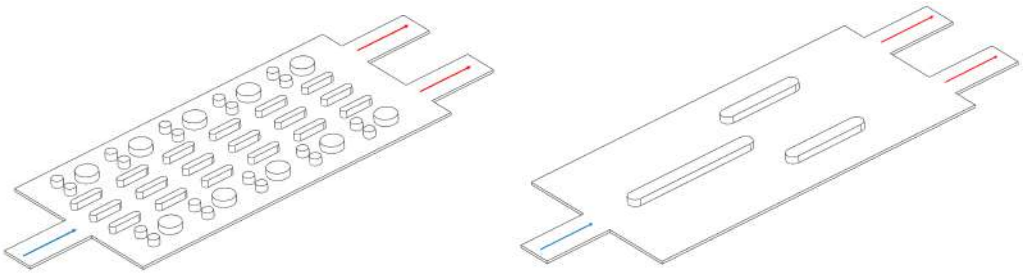

(α′) *Fl1* (β′) *Fl2*

Σχήμα Α′.3: *1I2O: Υπόστρωμα ψύκτρας με διαμορφώσεις πτερυγίων Fl1 και Fl2.*

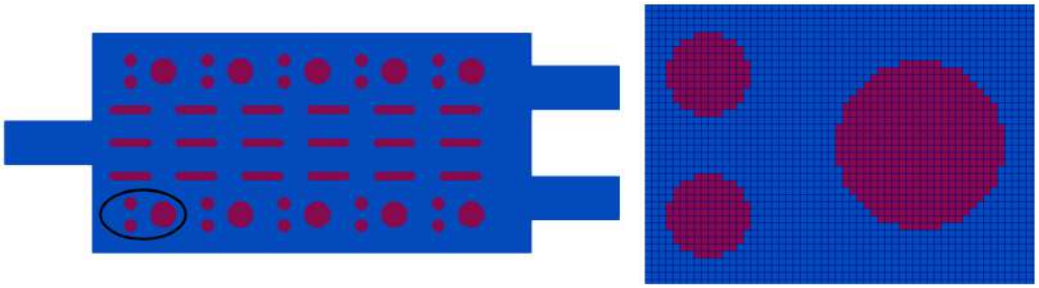

Σχήμα Α′.4: *1I2O-Fl1 (2.5D): Προσεγγιστική αναπαράσταση της γεωμετρίας των πτερυγίων στο 2Δ καρτεσιανό πλέγμα. Το 2.5Δ μοντέλο αντιλαμβάνεται τα στερεά πτερύγια, όχι σαν αυστηρά στερεά σώματα, αλλά ως περιοχές στο πλέγμα με τοπικά μοναδιαίες τιμές πορώδους.*

Case	1I2O-Fl1			1I2O-Fl2		
$\Delta p\,(Pa)$	2.5Δ $T_{b,max}\,(K)$	3Δ $T_{b,max}\,(K)$	Relative Error	2.5Δ $T_{b,max}\,(K)$	3Δ $T_{b,max}\,(K)$	Relative Error
50	421.99	421.32	0.55%	407.46	404.75	2.59%
400	330.70	330.12	1.93%	342.86	334.83	23.05%

Πίνακας Α′.1: *1I2O-Fl1/Fl2: Μέγιστη θερμοκρασία $T_{b,max}$ που εμφανίζεται στο μέσο επίπεδο του υποστρώματος.*

Case	1I2O-Fl1			1I2O-Fl2		
$\Delta p\,(Pa)$	2.5Δ $T_{b,avg}\,(K)$	3Δ $T_{b,avg}\,(K)$	Relative Error	2.5Δ $T_{b,avg}\,(K)$	3Δ $T_{b,avg}\,(K)$	Relative Error
50	377.89	378.43	0.69%	370.78	369.18	2.31%
400	318.57	320.59	9.81%	327.77	324.73	12.29%

Πίνακας Α′.2: *1I2O-Fl1/Fl2: Μέση θερμοκρασία $T_{b,avg}$ που εμφανίζεται στο μέσο επίπεδο του υποστρώματος.*

Case	1I2O-Fl1			1I2O-Fl2		
$\Delta p\,(Pa)$	2.5Δ $\dot{m}_I\,(g/s)$	3Δ $\dot{m}_I\,(g/s)$	Relative Error	2.5Δ $\dot{m}_I\,(g/s)$	3Δ $\dot{m}_I\,(g/s)$	Relative Error
50	0.0369	0.0371	0.54%	0.0432	0.0444	2.7%
400	0.299	0.297	0.67%	0.364	0.371	1.89%

Πίνακας Α′.3: *1I2O-Fl1/Fl2: Παροχή μάζας εισόδου $\dot{m}_I$ της ψύκτρας.*

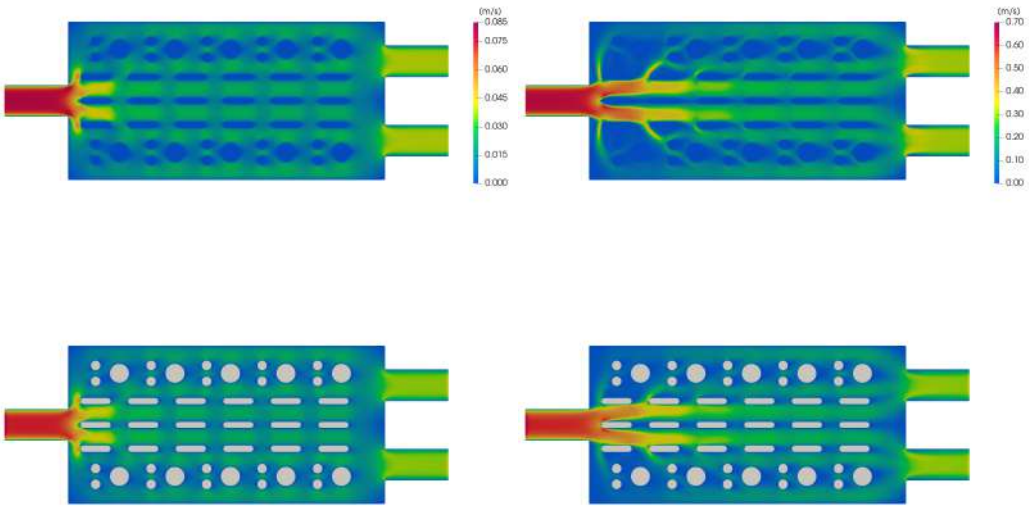

(α′) $50Pa$ (β′) $400Pa$

Σχήμα Α′.5: *1I2O-Fl1: Πεδίο ταχύτητας στο μέσο του χωρίου του ρευστού από τις 2.5Δ επιλύσεις (πάνω σχήματα) και τις 3Δ προσομοιώσεις (κάτω σχήματα).*

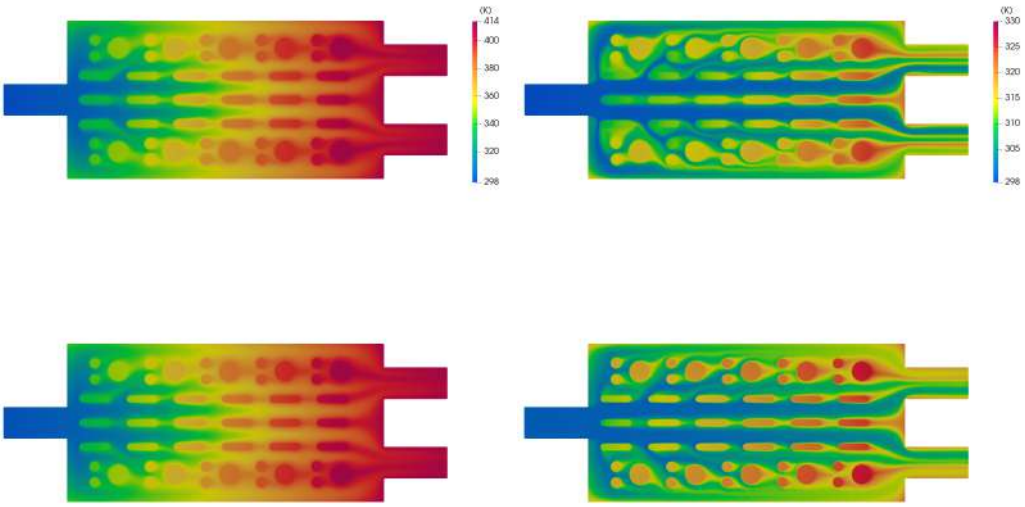

(α′) $50Pa$ (β′) $400Pa$

Σχήμα Α′.6: *1I2O-Fl1: Θερμοκρασιακό πεδίο στο μέσο του χωρίου του ρευστού από τις 2.5Δ επιλύσεις (πάνω σχήματα) και τις 3Δ προσομοιώσεις (κάτω σχήματα).*

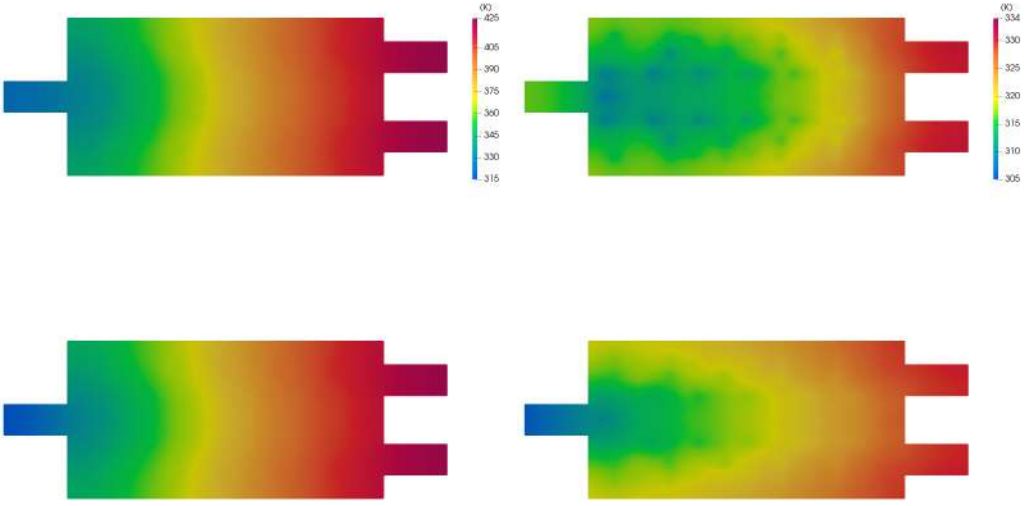

(α′) $50Pa$ (β′) $400Pa$

Σχήμα Α′.7: *1I2O-Fl1: Θερμοκρασιακό πεδίο στο μέσο του υποστρώματος από τις 2.5Δ επιλύσεις (πάνω σχήματα) και τις 3Δ προσομοιώσεις (κάτω σχήματα).*

Ακόμα και αν ήταν δυνατή η πιστή αναπαράσταση της γεωμετρίας των στερεών πτερυγίων στο καρτεσιανό πλέγμα για τις 2.5Δ προσομοιώσεις, διαφορές με τα 3Δ αποτελέσματα είναι αναπόφευκτες, καθώς το 2.5Δ μοντέλο είναι ένας επιλύτης του πρωτεύοντος προβλήματος μιας TopO και έτσι τα πτερύγια στο χωρίο του ρευστού δεν θεωρούνται αυστηρά στερεά σώματα, με τη συνθήκη μη-ολίσθησης να τίθεται έμμεσα μέσω των όρων Brinkman. Τέλος παρόλο που το 2.5Δ μοντέλο διατηρεί μέρος της πληροφορίας από την διάσταση του ύψους, προφανώς δεν είναι δυνατόν να δίνει τα ίδια αποτελέσματα με μια πλήρη 3Δ επίλυση.

Εφαρμογές TopO

Σε όλα τα προβλήματα TopO που ακολουθούν δεν θα χρησιμοποιηθούν κριτήρια περιορισμού όγκου, διότι είναι επιθυμητό να δοθεί η ελευθερία στον αλγόριθμο να αποφασίζει πόσο στερεό υλικό (πτερύγια) θα τοποθετήσει μέσα στο χωρίο του ρευστού με βάση το σημείο λειτουργίας (δεδομένη κλίση πίεσης) της ψύκτρας. Η βελτιστοποίηση τρέχει ως και 300 κύκλους ή μέχρι:

$$\frac{F^{\kappa+1} - F^{\kappa}}{F^{\kappa}} < 10^{-6}, \quad \text{where } \kappa \text{ is the cycle counter} \tag{A′.59}$$

Ψύκτρες με διατάξεις μιας εισόδου-μιας εξόδου (1I1O) και μιας εισόδου-δύο εξόδων (1I2O) σχεδιάζονται για πτώσεις πίεσης $400Pa$, $800Pa$ και $200Pa$, $400Pa$ αντίστοιχα. Οι ζώνες εισόδου και εξόδου των υπολογιστικών χωρίων αποτελούν ζώνες που καταλαμβάνονται μόνιμα από ρευστό και έτσι δεν ανήκουν στο χώρο σχεδιασμού της βελτιστοποίησης. Το μέρος του υποστρώματος που αντιστοιχεί στο χώρο σχεδιασμού θεωρείται ομοιόμορφα θερμαινόμενο.

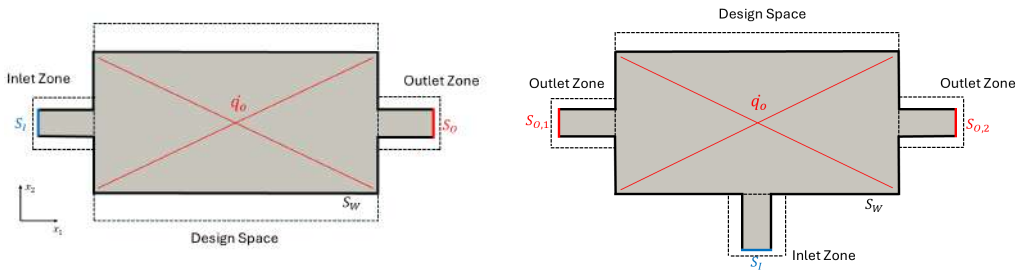

(α′) *1I1O-TopO* (β′) *1I2O-TopO*

Σχήμα Α′.8: *1I1O/1I2O-TopO: Υπολογιστικό χωρίο με τα όρια εισόδου S_I, όρια εξόδου S_O, στερεά όρια S_W και χώρος σχεδιασμού. Για την 1I2O-TopO περίπτωση, $S_O = S_{O,1} \cup S_{O,2}$*

Τα σχήματα Α′.10 και Α′.11 δείχνουν τις τελικές βέλτιστες γεωμετρίες των ψυκτρών με μικροκανάλια που προέκυψαν στο τέλος της διαδικασίας βελτιστοποίησης. Αυτές οι γεωμετρίες προέκυψαν εξάγοντας τις ισογραμμές του πεδίου β και στη συνέχεια παράγοντας 3Δ επιφάνειες καθ' ύψος. Φαίνεται ότι για τις μι-

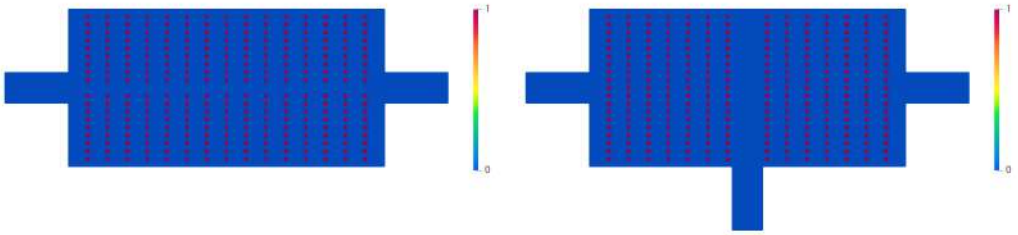

(α′) *1I1O-TopO* (β′) *1I2O-TopO*

Σχήμα Α′.9: *1I1O/1I2O-TopO: Αρχικοποίηση του πεδίου του πορώδους a. Μηδενικές τιμές πορώδους υποδεικνύουν ρευστό ενώ μοναδιαίες τιμές μηδιαπερατότητας αντιστοιχούν σε στερεό υλικό.*

κρότερες κλίσεις πίεσης, ο αριθμός των στερεών πτερυγίων που δημιουργούνται στο χωρίο του ρευστού είναι πολύ μικρότερος, εξαιτίας της μικρότερης πτώσης πίεσης που οδηγεί τη ροή. Ο αλγόριθμος προσπαθεί να αξιοποιήσει τους μηχανισμούς αγωγής και συναγωγής, τοποθετώντας όσο το δυνατόν περισσότερα πτερύγια σε στρατηγικές θέσεις ώστε να μεγιστοποιήσει την επιφάνεια συναγωγής, χωρίς όμως να αυξήσει την υδραυλική αντίσταση τόσο ώστε να δυσκολέψει τη διέλευση της ροής. Παρατηρείται επίσης ότι ο αλγόριθμος τοποθετεί στερεό υλικό γύρω από τα στερεά όρια που ανήκουν στο χώρο σχεδιασμού του Ω και ομαλοποιεί τις απότομες ορθές γωνίες του υπολογιστικού χωρίου ώστε να ευνοήσει τη ροή. Η θερμική απόδοση μιας ψύκτρας κρίνεται με βάση τη θερμική της αντίσταση, που όπως φαίνεται στο πίνακα Α′.4 ικανοποιητική θερμική απόδοση επιτυγχάνεται με μικρές παροχές μάζας, που είναι εξάλλου και από τα κύρια χαρακτηριστικά και πλεονεκτήματα των ψυκτρών με μικροκανάλια.

$$R_{th} = \frac{T_{b,max} - T_I}{\dot{Q}} = \frac{T_{b,max} - T_I}{\dot{q}_o A} \tag{Α′.60}$$

με A την επιφάνεια του υποστρώματος στην οποία εφαρμόζεται η θερμοροή $\dot{q}_o$.

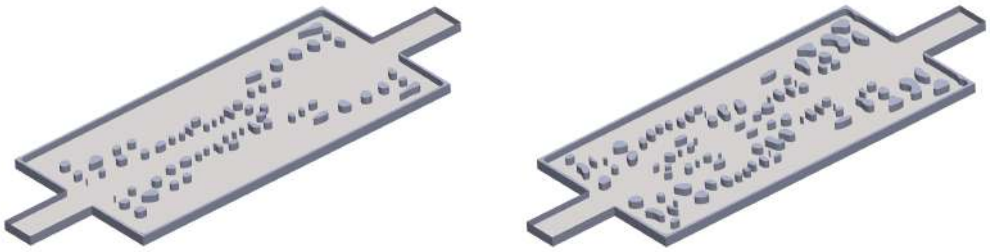

(α′) $400Pa$ (β′) $800Pa$

Σχήμα Α′.10: *1I1O-TopO: Βέλτιστες γεωμετρίες ψυκτρών.*

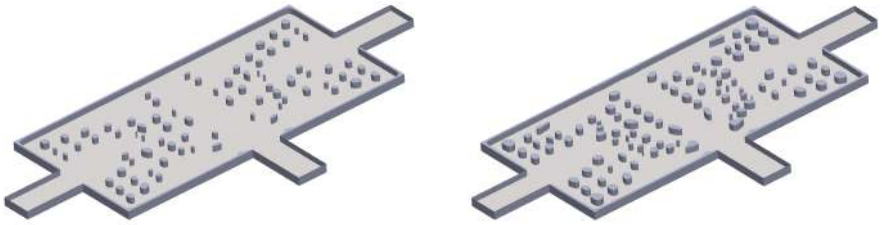

(α′) $200Pa$ (β′) $400Pa$

Σχήμα Α′.11: *1I2O-TopO: Βέλτιστες γεωμετρίες ψυκτρών.*

Πτώση Πίεσης (Pa)	Θερμική Αντίσταση $R_{th}\,(K/W)$	$\dot{m}_I\ (g/s)$
1I1O-TopO		
400	2.02	0.194
800	1.45	0.292
1I2O-TopO		
200	2.05	0.193
400	1.21	0.355

Πίνακας Α′.4: *1I1O/1I2O-TopO: Θερμική αντίσταση και παροχή μάζας εισόδου για τις βελτιστοποιημένες ψύκτρες. Όσο μικρότερη είναι η τιμή του R_{th}, τόσο καλύτερη είναι η θερμική απόδοση της ψύκτρας.*

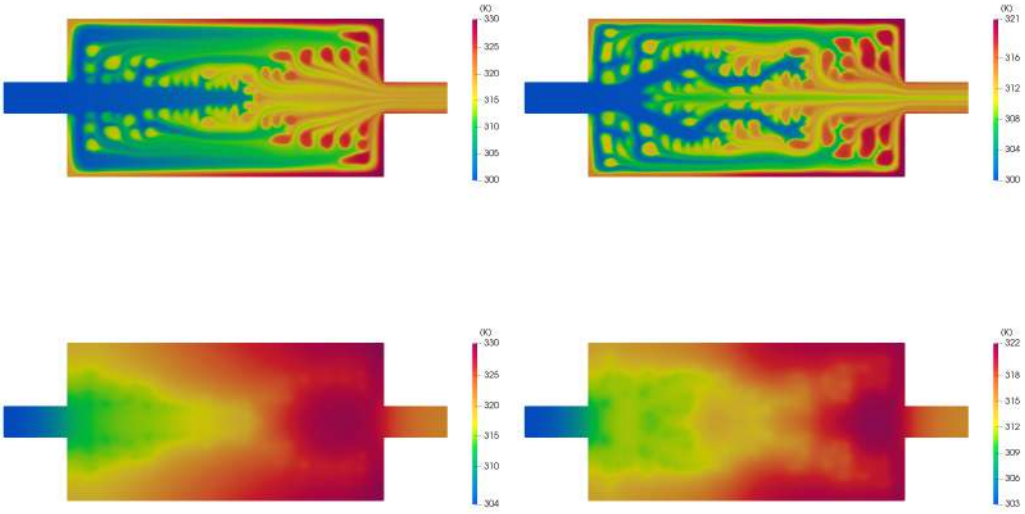

(α′) $400Pa$ (β′) $800Pa$

Σχήμα Α′.12: *1I1O-TopO: Πρωτεύον θερμοκρασιακό πεδίο του ρευστού χωρίου (πάνω σχήματα) και του στερεού χωρίου (κάτω σχήματα) για τις βελτιστοποιημένες ψύκτρες.*

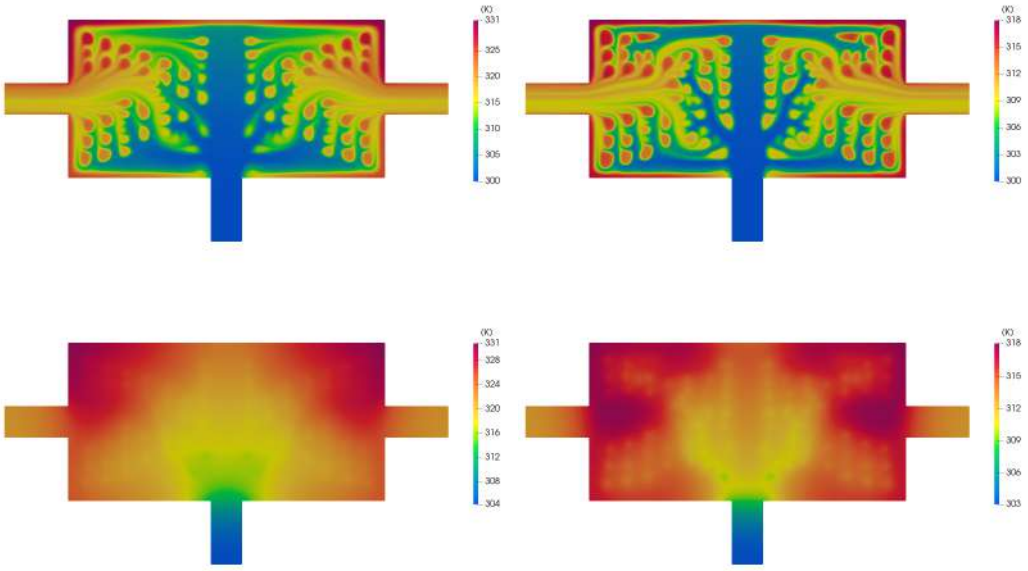

(α′) $200Pa$ (β′) $400Pa$

Σχήμα Α′.13: *1I2O-TopO: Πρωτεύον θερμοκρασιακό πεδίο του ρευστού χωρίου (πάνω σχήματα) και του στερεού χωρίου (κάτω σχήματα) για τις βελτιστοποιημένες ψύκτρες.*

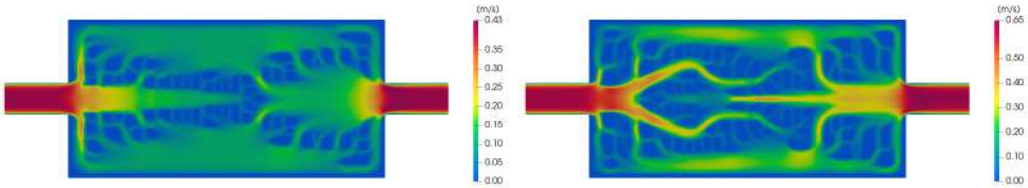

(α′) *1I1O-TopO* ($400Pa$) (β′) *1I1O-TopO* ($800Pa$)

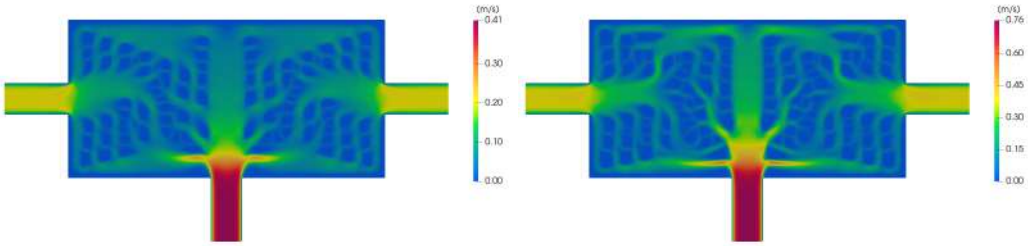

(γ′) *1I2O-TopO* ($200Pa$) (δ′) *1I2O-TopO* ($400Pa$)

Σχήμα Α′.14: *1I1O/1I2O-TopO: Πρωτεύον πεδίο ταχύτητας του ρευστού χωρίου για τις βελτιστοποιημένες ψύκτρες.*

Σε ρεαλιστικές εφαρμογές ψύξης ηλεκτρονικών συστημάτων, η κάτω επιφάνεια του υποστρώματος δεν είναι ομοιόμορφα θερμαινόμενη, αλλά αντίθετα ζεστά σημεία παρατηρούνται τα οποία αντιστοιχούν στις θέσεις των τσιπ στην ηλεκτρονική πλακέτα. Για το λόγο αυτό, σχεδιάζεται ξανά η 1I1O ψύκτρα για τις ίδιες πτώσεις πίεσης με τη διαφορά ότι τώρα η θερμοροή $\dot{q}_o$ εφαρμόζεται τοπικά σε περιοχές του υποστρώματος. Η αρχικοποίηση του πεδίου του πορώδους είναι ίδια με αυτή που φαίνεται στο σχήμα Α΄.9α΄.

Με αναφορά το σχήμα Α΄.16, εύκολα μπορεί κανείς να παρατηρήσει ότι στη περίπτωση αυτή τα πτερύγια είναι λιγότερο διασκορπισμένα στο χώρο σχεδιασμού και συγκεντρώνονται γύρω από τα ζεστά σημεία με σκοπό την αποτελεσματική απαγωγή θερμότητας από τις κρίσιμες αυτές περιοχές.

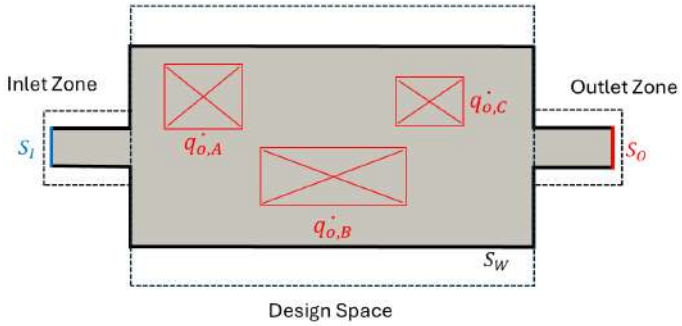

Σχήμα Α΄.15: *1I1O(VHF)-TopO: Υπολογιστικό χωρίο με τα όρια εισόδου S_I, όρια εξόδου S_O, στερεά όρια S_W και χώρος σχεδιασμού με τοπικά θερμαινόμενες περιοχές.*

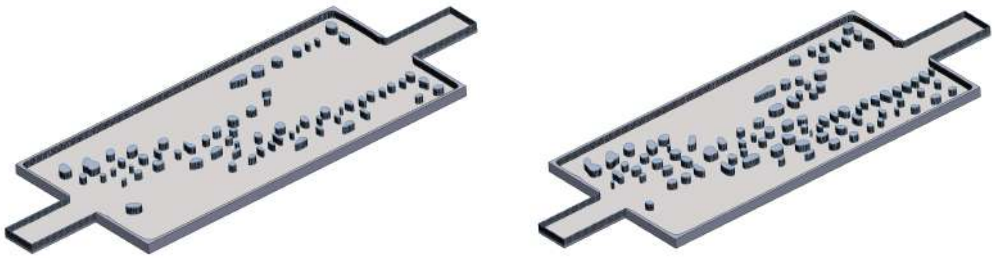

(α΄) $400Pa$ (β΄) $800Pa$

Σχήμα Α΄.16: *1I1O(VHF)-TopO: Βέλτιστες γεωμετρίες ψυκτρών, με τα πτερύγια να σχηματίζουν λιγότερο συμμετρικές διαμορφώσεις και να συγκεντρώνονται γύρω από τα ζεστά σημεία.*

Τέλος με αφορμή το γεγονός ότι οι αιτιοκρατικές μέθοδοι βελτιστοποίησης εξαρτώνται από την αρχικοποίηση των μεταβλητών σχεδιασμού, γίνεται μια μικρή μελέτη στην ευαισθησία της βέλτιστης λύσης που προκύπτει, από την αρχικοποίηση στο πεδίο του πορώδους. Αυτή τη φορά γίνεται αρχικοποίηση του χωρίου

του ρευστού (χώρος σχεδιασμού) με λίγα στερεά πτερύγια που καταλαμβάνουν μεγάλο μέρος του χώρου σχεδιασμού, σε αντίθεση με μικρού όγκου στερεές περιοχές όπως στις προηγούμενες περιπτώσεις. Παρόλα αυτά, αν και οι τελικές βέλτιστες λύσεις διαφέρουν (δεδομένου ότι δεν χρησιμοποιήθηκαν περιορισμοί όγκου στη TopO, ο αλγόριθμος είναι ακόμη πιο επιρρεπής στο να προσκολλάται στο πιο κοντινό τοπικό ελάχιστο), ο αλγόριθμος και σε αυτό το σενάριο προτιμά τη δημιουργία πολλών μικρών στερεών πτερύγιων (και άρα πολλών μικροκαναλιών) για να μεγιστοποιήσει την επιφάνεια συναγωγής.

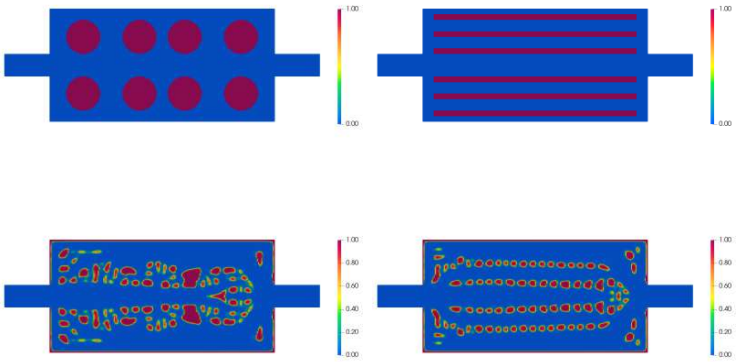

(α′) *1I1O(I1)-TopO* (β′) *1I1O(I2)-TopO*

Σχήμα Α′.17: *1I1O(SA)-TopO: Διαφορετικές αρχικοποιήσεις στο πεδίο του πορώδους (πάνω σχήματα) και τα αντίστοιχα β πεδία (κάτω σχήματα) τα οποία προέκυψαν απο τη διαδικασία TopO.*

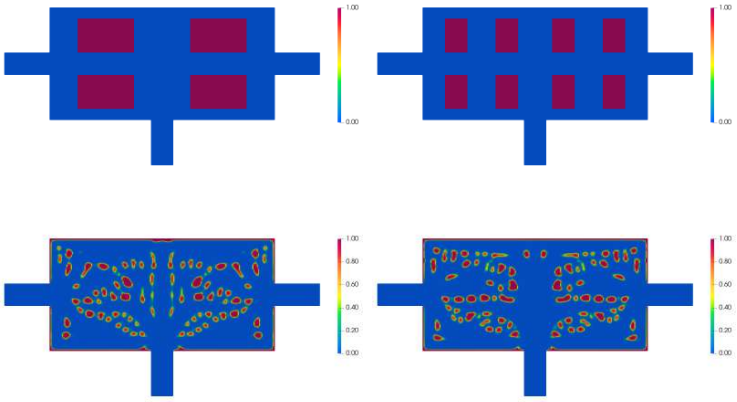

(α′) *1I2O(I1)-TopO* (β′) *1I2O(I2)-TopO*

Σχήμα Α′.18: *1I2O(SA)-TopO: Διαφορετικές αρχικοποιήσεις στο πεδίο του πορώδους (πάνω σχήματα) και τα αντίστοιχα β πεδία (κάτω σχήματα) τα οποία προέκυψαν απο τη διαδικασία TopO.*